SAPIENZA
UNIVERSITÀ DI ROMA

Evolution of the accretion geometry of the black hole X-ray binary GX 339-4 observed by NuSTAR and NICER

Facoltà di Scienze Matematiche, Fisiche e Naturali
Laurea Magistrale in Astronomia e Astrofisica

Valerio Pandolfi
ID number 1885039

Advisor
Prof.ssa Irene Di Palma

External Advisor
Prof. Andrea Santangelo

Academic Year 2023-2024

Evolution of the accretion geometry of the black hole X-ray binary GX 339-4 observed by NuSTAR and NICER

Sapienza University of Rome

This thesis has been typeset by LaTeX and the Sapthesis class.

Author's email: valerio.pandolfi.vp@gmail.com

Abstract

GX 339-4 is one of the most thoroughly-studied black hole X-ray binaries, known for its regular outbursts (approximately every two years), with flux variations spanning over three orders of magnitude. In this work, I conducted a broadband analysis of X-ray spectra of the source captured during the outburst it underwent in 2021, combining *NuSTAR* and *NICER* data. Aiming to utilise simultaneous or quasi-simultaneous observations, corresponding to a temporal separation of at most one day between end and start time of different instances, I carefully selected 13 observations from *NuSTAR*, and 24 observations from *NICER*, resulting in a total exposure of more than 330 ks, grouped in 11 multi-mission spectral epochs. With the opportunity to track the source throughout the entirety of its outburst, I constrained the evolution of the accretion geometry by incorporating: a multi-temperature blackbody accretion disk model, a Comptonized corona power-law, and a relativistic reflection component to reproduce the reprocessing in the disk of high-energy photons from the corona. Moreover, I implemented a self-consistent treatment of the Comptonization of both disk and reflection photons, and measured the black hole spin. Results of my investigation point to a scenario in which the inner region of the accretion disk is modestly truncated in the bright hard state and during the entire state transition ($R_{\rm in} \lesssim 2R_{\rm ISCO}$), progressively moving closer to the black hole and extending up to the innermost stable circular orbit (ISCO) radius in the soft state. The data also suggests an intense variability of the coronal size and physical properties, showing an initially extended corona comprised by a thermal electron distribution reducing in size and presenting a non-thermal component after the state transition; and is consistent with a near-maximal value of the black hole spin ($a_* = 0.9974^{+0.0002}_{-0.0004}$), in good agreement with estimates from previous studies.

Contents

Acronyms

ADAF advection-dominated accretion flow. 21, 23

AGN active galactic nucleus. 4, 5, 15, 20

BH black hole. 1–3, 5–10, 13–16, 20–26, 35, 46, 48, 59, 60, 63, 64, 66–68

BHXRB black hole X-ray binary. 6, 7, 11, 15–17, 20, 24–26, 28, 44, 60, 67

BLR broad line region. 4, 5

CALDB Calibration Database. 29, 30, 32

d.o.f. degree of freedom. 37, 46, 47

FPM Focal Plane Module. 29–31, 36, 37, 39–44, 46, 50–55

FWHM full-width half-maximum. 30

GR general relativity. 1, 2, 7

GW gravitational wave. 2

HEASARC High Energy Astrophysics Science Archive Research Center. 29

HEASoft High Energy Astrophysics Software. 29, 30, 32

HID hardness-intensity diagram. 16–19, 28, 67

HMXB high mass X-ray binary. 6, 7

HXMT Hard X-ray Modulation Telescope. 25, 59

IR infrared. 17, 24

ISCO innermost stable circular orbit. 9, 14, 20, 21, 25, 58–60, 67

ISM interstellar medium. 33, 36, 37, 45, 47

ISS International Space Station. 26, 31, 32

IXPE Imaging X-ray Polarimetry Explorer. 22, 23

JAXA Japanese Aerospace Exploration Agency. 26

LMXB low mass X-ray binary. 6, 7, 24, 65

LoS line of sight. 4, 14, 36, 37, 45

MAXI Monitor All-sky X-ray Image. 15, 26–28

MJD modified Julian date. 15

NASA National Aeronautics and Space Administration. 26, 29, 31, 32

NICER Neutron star Interior Composition ExploreR. 11, 18–20, 24–29, 31–33, 37, 39–55, 67

NICERDAS NICER Data Analysis Software. 32

NLR narrow line region. 4, 5

NS neutron star. 6

NuSTAR Nuclear Spectroscopic Telescope Array. 11, 18–20, 24–33, 36, 39–44, 46, 48, 50–55, 67

NuSTARDAS NuSTAR Data Analysis Software. 30

SED spectral energy distribution. 8

SMBH supermassive black hole. 2, 4, 5, 7–9

UV ultraviolet. 7–9, 17

XMM X-ray Multi-Mirror. 25, 60

XRT X-Ray Telescope. 25

XTI X-ray Timing Instrument. 31, 32, 37, 39–44, 46, 50–55

Chapter 1

Introduction

More than a century has passed since Albert Einstein completely revolutionised our physical understanding of the universe with his theory of general relativity (GR) (Einstein 1916). With a combination of mathematical elegance and outstanding agreement with observations, GR is one of the pillars of modern Physics, but also one of the roots of its present incompleteness; it provided theoretical predictions that took tens of years to confirm, and some that will hardly ever be proven or disproven. In this thesis I will focus on one of its most exciting predictions: black holes (BHs). I will start by giving a short overview of their most relevant characteristics, before treating accretion onto BHs and the astrophysical systems we observe to study it.

1.1 Black Holes

In a general relativistic context, a BH is a region of spacetime in which the gravitational field is so intense that it generates a spacetime singularity enclosed in an event horizon. Matter and radiation crossing the event horizon surface will be increasingly pulled towards the central singularity, surrendering the possibility of leaving this region ever again. According to the *no-hair theorem* of general relativity, BHs are completely characterized by their mass (M), their angular momentum (J), and their electric charge (Q). Two black holes sharing these three parameters are observationally undistinguishable, making them the simplest macroscopic objects in the universe. Being composed by mostly neutral matter, astrophysical BHs are generally believed to have negligible electric charge, leaving solely mass and angular momentum as observable quantities.

The angular momentum of a BH is often expressed as a dimensionless spin parameter $a_* = cJ/(GM^2)$, where c is the speed of light, and G is the gravitational constant. Depending on this dimensionless spin parameter (hereafter just spin), there exist two analytical solutions to Einstein's Field Equations: a static and spherically symmetric spacetime corresponding to a non-rotating black hole (i.e., $a_* = 0$; Schwarzschild 1916), and a stationary, axisymmetric spacetime corresponding to a

rotating BH (i.e., $-1 \leq a_* \leq 1$; Kerr 1963), where the + (-) sign represents a corotating (counterrotating) BH with respect to our definition for the orientation of the axis parallel to the spin. The upper and lower limits on Kerr black holes' spin are crucial to guarantee the existence of the event horizon concealing the singularity, as values beyond these limits would imply a *naked singularity* exposed to the outside universe, a possibility deemed unphysical by Penrose's cosmic censorship conjecture (Penrose 1969).

Notwithstanding the solid mathematical formalism, for several decades the physical existence of BHs was a highly debated topic in the astronomy community. It was thanks to X-ray observations that in the early 1970s the first stellar-mass BH candidate was identified in Cygnus X-1 (Bolton 1972; Webster and Murdin 1972). Since then, owing to the outstanding advancements in detector development and observational methods, an increasing number of BH sources have been discovered. These are usually divided into two main classes: supermassive black holes (SMBHs) spanning from $\sim 10^5$ up to $\sim 10^{10}$ or more solar masses ($M_\odot$); and the aforementioned stellar-mass BHs, comprising objects with masses below $100\,M_\odot$. Despite the existence of some candidates (see, e.g., Abbott et al. 2020; Vitral et al. 2023; Häberle et al. 2024), definitive confirmation of BHs in the intermediate mass gap remains arduous.

The challenge of observing objects which are black by definition, and hence do not emit electromagnetic radiation of any kind, is not trivial. At the present day, however, BHs have been successfully observed with a diverse array of methods and approaches. Dynamical measurements of the orbits of stars around SMBHs in galactic centers provide both an indication of their existence and an estimate of their mass (e.g., Ghez et al. 2008); the first groundbreaking observation of gravitational waves (GWs) from a merger of two stellar-mass black holes by LIGO (Abbott et al. 2016) paved the way for the dawn of multi-messenger astronomy and yielded yet another confirmation of Einstein's theory of general relativity; while the Event Horizon Telescope Collaboration (2019) has recently produced the first image of the regions surrounding a SMBH and emitting in the radio band. Each of these methods is, however, strongly dependent on the specific mass range of the observed object, and limited by current instruments and facilities. On the contrary, thanks to the great similarities between the signatures of physical processes governing the behaviour of matter in regions close to black holes' event horizons, observations in the X-rays enable probing systems belonging to different classes with the same method.

1.2 Accretion onto Black Holes

The gravitational pull exerted by a compact object drives part of the surrounding matter towards falling onto the object itself, in a process which takes the name of *accretion*. Considering a BH sitting in a gas-rich environment, matter initially at

rest and in absence of magnetic fields will experience radial infall towards the BH, being accreted without the emission of radiation. However, if the infalling matter possesses non-zero initial angular momentum from its orbital motion, at some distance from the BH centrifugal forces will become comparable to the gravitational one, causing the accreting gas to move on elliptical orbits and eventually condense into a circumstellar disk structure around the central compact object, the *accretion disk*. The centrifugal barrier will hence prevent matter from further approaching the BH, unless a process capable of transporting angular momentum outwards takes place. In the standard scenario of a geometrically thin and optically thick accretion disk, friction between adjacent layers of the disk dissipates angular momentum of the orbiting matter, leading to the conversion of gravitational energy into thermal emission radiated away from the disk surface (e.g., Shakura & Sunyaev 1973). This mechanism contributes to powering some of the most energetic and luminous sources observed in the universe in the form of relativistic jets, present in both stellar-mass and supermassive BHs. The resulting *accretion luminosity*, stemming from the release of gravitational energy as thermal radiation, can be written as:

$$L_{acc} = \eta \dot{M} c^2 \,, \tag{1.1}$$

where $\dot{M}$ is the *mass accretion rate* (i.e., mass accreted per unit time), and the accretion efficiency η (i.e., ratio between energy produced and rest-mass energy) for a thin disk is in the range 5% - 42% depending on the spin (Thorne 1974). For reference, the efficiency of nuclear fusions powering stars can be estimated to be less than 1%. Owing to the large efficiency of the accretion process, emitted photons scattering into accreting matter in more external layers may reach an outward radiation pressure large enough to overcome the gravitational pull of the BH on infalling gas. This feedback process which regulates the accretion rate up to even inhibiting it, sets a theoretical limit to the highest accretion luminosity a source can have. Under the assumption of spherical symmetry of the system, this boundary is known as the *Eddington limit*, and amounts to a luminosity:

$$L_{Edd} = \frac{4\pi G M_{BH} m_p c}{\sigma_T} = 1.26 \times 10^{38} \left(\frac{M}{M_\odot} \right) \text{ erg s}^{-1} \,, \tag{1.2}$$

where m_p is the proton mass, $\sigma_T = 6.65 \times 10^{-25}$ cm^{-2} is the Thomson cross section, and $M_\odot = 1.988 \times 10^{33}$ g is the mass of the Sun. It is also possible to define the Eddington accretion rate $\dot{M}_{Edd} = L_{Edd}/(\eta c^2)$ (i.e., mass accretion rate required to reach L_{Edd}), and the *Eddington ratio* L_{bol}/L_{Edd}, where L_{bol} is the bolometric luminosity of the source.

Up to this point we have assumed the BH to be situated in a gas-rich environment without actually discussing the physical scenarios leading to this. In the following paragraphs I will give an overview of different accreting BHs, including the source of the accreting matter and the effect they have on their surroundings.

1.3 Active Galactic Nuclei

It is generally believed that most (if not all) galaxies host a supermassive black hole at their center, measuring between 10^5 and 10^{10} times the mass of the Sun. Our own Milky Way galaxy is no exception to this: trajectories of stars in the galactic center provide evidence for an apparently invisible object of about 4×10^6 $M_\odot$ concentrated in a 100 AU radius (e.g., Genzel et al. 2010; Gillessen et al. 2017). In fact, shortly after the groundbreaking work leading to the first direct image of the shadow of a SMBH (Event Horizon Telescope Collaboration 2019), further findings were released from observations of $SgrA*$ (Event Horizon Telescope Collaboration 2022), precisely the SMBH at the center of our galaxy.

These unprecedented results showcase radio emission from SMBHs and matter they accrete from the surrounding gas-dense environments in galactic centers. In some cases the mass accretion rate can be so high to result in radiation that completely outshines the total contribution from stars in the whole galaxy. When in this state the central SMBH is referred to as an active galactic nucleus (AGN), placing among the brightest non-transient sources in the universe.

Historically, observations of bright emission from distant galaxies and raging from radio to gamma-rays, ensued the identification of several different kinds of objects. Early AGN classifications were solely based on phenomenological features, with the interpretation of different spectra with different theoretical models leading to the assumption of a Zoo of sources (Quasars, Seyfert galaxies, Radio galaxies, Blazars). Through the years, however, a joint effort brought to a unified classification, identifying differences between type I and type II AGN and blazars as stemming from a combination of different viewing angles between the system's symmetry axis and our line of sight (LoS). More specifically, type I AGN present both broad and narrow emission lines in their optical spectra, while type II exclusively show narrow lines (Beckmann & Shrader 2012).

As shown by the sketch in Figure 1.1, AGN systems comprise the central SMBH with an accretion disk and a jet, surrounded by dust-free gas clouds forming a broad line region (BLR) and narrow line region (NLR), and by a dust torus. Observing with a near face-on view (i.e., small inclination angle between LoS and AGN jet) will lead to the identification of the source as a blazar. Increasing the inclination angle will result in the observation of both broad and narrow emission line features in the spectrum, respectively from the BLR and NLR, and hence in a type I AGN. Finally, near edge-on views of the system cause emission from the BLR to be obscured by the dusty torus, while leaving radiation coming from the NLR unaffected (type II AGN).

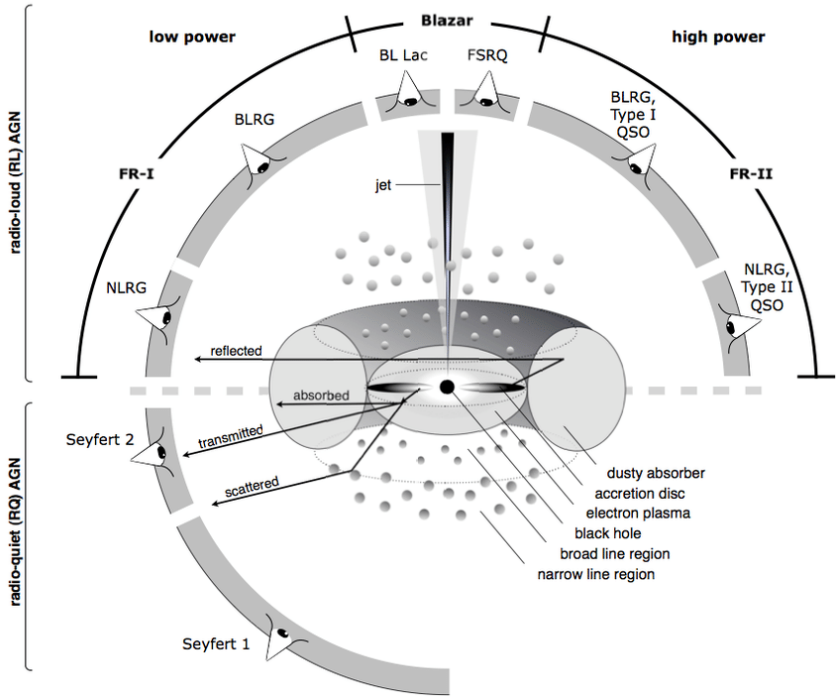

Figure 1.1. Schematic representation of the AGN unification model, with a classification depending on the observing angle and on jet emission. In the standard picture, a supermassive black hole is surrounded by an accretion disk with a sub-pc lenghtscale. The broad line region consists of high-density ($n_e > 10^8$ cm^{-3}) dust-free gas clouds, at a distance of $0.01 - 1$ pc from the BH. A dusty torus then extends from 0.1 to 10 pc; while the low-density ($n_e < 10^6$ cm^{-3}) ionized gas forming the narrow line region stretches up to 100 pc. (Beckmann & Shrader 2012; graphic by Marie-Luise Menzel).

Furthermore, supermassive black holes strongly affect their surrounding environments up to galactic scales: their growth and evolution is strongly coupled to that of their host galaxies. During active periods due to enhanced accretion, SMBHs release enormous amounts of energy in the galaxy in the form of radiative and kinetic processes (e.g., outflows, winds, jets, ...). This AGN feedback mechanism can favour or inhibit star formation, leaving an imprint on the host galaxy. In this context, the study of accreting SMBHs constitutes a way of probing strong gravity regimes and galactic evolution.

The dynamical timescales for accreting black hole systems are limited by causality to be at most of order $\tau \sim \frac{R_g}{c}$, where $R_g = \frac{GM_{\rm BH}}{c^2} \approx 1.5 \text{ km } (\frac{M_{\rm BH}}{M_\odot})$ is the BH's gravitational radius. Therefore, typical time frames for accretion processes directly depend on the BH mass, posing a significant challenge for studying AGN phenomenology and variability, as observations are limited by human lifetimes. However, the vastly similar phenomenology between AGN and accreting stellar-mass BHs, makes it possible to infer crucial properties of the former systems by observing the latter.

1.4 X-ray Binaries

The gravitational collapse of massive star progenitors (i.e., $M \gtrsim 8M_{\odot}$) results in the birth of a compact object remnant: either a neutron star (NS) or a black hole. Stellar-mass BHs are formed in the gravitational collapse of progenitors $M \gtrsim 30M_{\odot}$ or, less frequently, in mergers of binary and multiple systems. It has been speculated that a large fraction (up to half) of all stars in our galaxy are in binary systems, result that we do not expect to vary considerably for other galaxies (Duchêne and Kraus 2013). If the progenitor star is in a binary system which remains bound after the stellar collapse, the BH remnant will start accreting matter from its companion star, given that the latter is in a close enough orbit.

Owing to the extreme gravity regimes resulting in prominent X-ray emission, the system is referred to as a black hole X-ray binary (BHXRB). Limited by strong intergalactic absorption and current instrumental resolution, NS and BH X-ray binaries have mostly been observed in our galaxy and neighbouring ones, for a total of ∼500 sources, 72 of which are BHXRBs (Corral-Santana et al. 2016). BHs in X-ray binaries are generally between 4 and 20 solar masses and are further classified depending on the donor star's mass:

- in a high mass X-ray binary (HMXB) the companion has mass $M_2 \gtrsim 5M_{\odot}$,
- in a low mass X-ray binary (LMXB) the companion has mass $M_2 \lesssim 1M_{\odot}$.

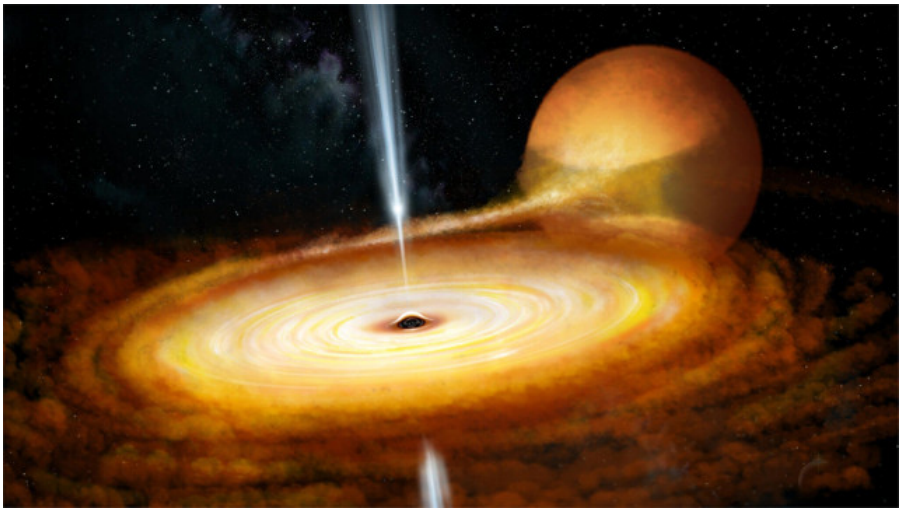

Figure 1.2. Artist's impression of a black hole X-ray binary, depicting a stellar-mass BH accreting matter from a donor star. The material being transferred forms an accretion disk around the central engine, and a highly collimated relativistic jet is launched in the direction orthogonal to disk. Image credits: J. Paice, P. Gandhi (University of Southampton, IUCAA).

The LMXB scenario sees the mass donor evolving to fill its Roche lobe (i.e., region enclosed in a critical gravitational equipotential surface of a binary system), and material being then transferred through the inner Lagrangian point L_1 onto the compact object, in a process which takes the name of *Roche lobe overflow*. These systems are typically older than their high mass counterparts, with the companion star typically being M-K class and hence optically fainter than the compact object: $L_X/L_{\rm opt} \lesssim 0.1$. It is therefore challenging to accurately constrain masses, inclination and other binary parameters of LMXBs.

On the contrary, HMXBs are younger systems characterized by strong optical and ultraviolet (UV) emission by the early-type companion (typically O-B class with $T_{\rm eff} \sim 10^4 - 10^5\,{\rm K}$), even exceeding the X-ray luminosity. Furthermore, accretion is driven by both Roche lobe overflow, and strong stellar winds from the massive donor star being captured by the compact object.

The majority of black hole X-ray binary sources in our galaxy are transient sources, alternating long periods of quiescence characterized by the low luminosity of the system, and recurrent outburst episodes with a luminosity increase by several orders of magnitude due to enhanced accretion.

1.5 Motivation and Outline

Although our understanding of BHs has grown exponentially in the last decades, and despite them probably being the simplest macroscopic objects in the known universe, many questions remain unanswered. For instance, measuring black hole masses and spins is critical to conduct population studies to shed light onto the physical mechanisms driving formation and growth of SMBHs, and on the intermediate mass gap and the existence of intermediate-mass BHs. Investigating the behaviour of accretion flows in BHXRBs, which is thought to scale up to SMBHs, provides valuable insights about the formation and launching of the observed powerful relativistic jets, and enables the study of strong gravity effects near the event horizon, in an effort to test general relativity and explore the possibilities for new physics. For this reasons, this work will provide a detailed analysis of the variability and evolution of the inner accretion flows of the black hole X-ray binary GX 339-4, with the aim to constrain the evolution of its accretion geometry, and measure the BH spin.

The thesis is structured as follows: in Chapter 2 I will give an overview of the X-ray reflection spectroscopy technique used to study accretion onto BHs and measure their spin; in Chapter 3 I will present the scientific case of interest, the observations employed and the data reduction and spectral analysis employed to pursue the targeted goals; in Chapter 4 I will show our results and discuss their possible implications; before concluding and exploring future prospects for complementary analyses in Chapter 5.

Chapter 2

Observing Accreting Black Holes

As already discussed, the *no-hair theorem* states that BHs are completely characterized by just two quantities: their mass and their spin. The former can mostly be accurately estimated without needing to delve into the strong gravity regions in the immediate vicinities of the BH, and governed by general relativistic effects. Owing to great leap in the development of astronomical optics and detectors, we are able to constrain the movement of stars around BHs with incredible accuracy, hence obtaining precise dynamical measurements of their mass without significant observational efforts. On the contrary, accurately constraining the spin of a BH is a considerably more demanding endeavour, since it requires probing regions of spacetime heavily affected by the BH general relativistic nature. In this chapter we will explore the basics of how those measurements are conducted, starting from the first essential ingredient: modelling the X-ray spectral signature of the BH.

2.1 Spectral contributions

The closer matter gets to a BH, the more forcibly it is drawn to rotate around the BH itself, following geodesics imprinted into spacetime by its immense drag. In this scenario, gas in the form of hot and ionized plasma interacts with itself and with radiation, undergoing different processes and producing prominent emission. For stellar-mass BHs the spectral energy distribution (SED) is dominated by X-rays, while for SMBHs emission is mostly concentrated in the optical and UV bands. The sum of all these processes produce the different contributions to the system's spectrum, which are usually classified in 3 major spectral signatures, giving an opportunity to probe the phenomenology and geometry of matter around a BH.

2.1.1 Accretion disk

In the following regime of sub-Eddington mass accretion rate:

$$0.001 \lesssim \frac{\dot{M}}{\dot{M}_{\rm Edd}} \lesssim 0.3\,, \tag{2.1}$$

the accretion disk is assumed to be geometrically thin and optically thick, meaning that the semi-thickness of the disk h at the radial coordinate r is such that $h/r << 1$, and the mean free path of photons inside the disk $l = 1/(\sigma n)$, where σ is the photon scattering cross section and n the number density of scattering particles in the disk, is $l << h$. In these conditions the gas and photons in the accretion disk are in local thermal equilibrium. Each point on the disk surface is expected to emit a blackbody-like spectrum, with its temperature depending on the local orbital velocity and corresponding radial distance from the BH.

As long as the accretion disk is optically thick, its local effective temperature approximately scales as $\sim M^{-1/4} R^{-3/4}$, where M is the BH mass and R is the disk radius (Bambi et al. 2021). Integrating this emission radially over the whole disk results in a peculiar multi-temperature blackbody spectrum, peaked at $E_{\rm peak} \approx 2.36\, kT_{\rm in}$, where k is the Boltzmann constant, and $T_{\rm in}$ is the colour temperature at the disk inner edge $R_{\rm in}$. Here, the colour temperature $T_{\rm in}$ is a correction to the total effective temperature $T_{\rm eff}$ (i.e., the temperature of a blackbody emitting the same total energy per unit area as the disk), achieved by considering a colour correction factor κ. $T_{\rm in}$ is in fact the temperature inferred from fitting a blackbody to the observed disk spectrum, and it is usually larger than $T_{\rm eff}$ as a result of several processes modifying the emitted disk spectrum. For instance, the up-scattering of lower energy photons from outer regions in the inner parts of the disk, and opacity effects due to the disk's non-homogeneous optical depth, all lead to a modified spectrum with respect to a standard blackbody. Considering a pure hydrogen plasma, the inner disk colour temperature is given by

$$T_{\rm in} = \kappa \left[\frac{(L_d/L_E)\, m_P\, c^5}{2GM\, r_{\rm in}^3\, \eta\, \sigma_{SB}\, \sigma_T} \right]^{1/4}, \tag{2.2}$$

where $r_{\rm in}$ is the inner accretion disk radius in units of gravitational radii, L_d/L_E is the ratio between the disk luminosity and the Eddington luminosity, m_P is the proton mass, $\eta \sim 0.1$ is the accretion efficiency, σ_{SB} is the Stefan-Boltzmann constant, σ_T is the Thomson cross section, and $\kappa \approx 1.5 - 2.0$ (Davis et al. 2005) is the colour correction factor. By normalizing for typical values, we numerically obtain

$$E_{\rm peak} \approx 2.9 \text{ keV } \frac{\kappa}{1.7} \left(\frac{L_d}{L_E}\right)^{1/4} \left(\frac{\eta}{0.1}\right)^{-1/4} \left(\frac{M}{10\, M_\odot}\right)^{-1/4} \left(\frac{r_{\rm in}}{2}\right)^{-3/4}. \tag{2.3}$$

Therefore, assuming the disk to extend up to the innermost stable circular orbit (ISCO) radius, we find that emission from the accretion disk in supermassive black holes peaks in the UV band at around $1-100$ eV, while for disks of stellar-mass BHs it peaks in the soft X-rays[1] at around $0.1-1$ keV. A typical thermal disk spectrum is shown in Figure 2.1.

[1] The X-ray band typically encompasses the energy range $0.1-100$ keV, and is divided into soft X-rays (below 10 keV) and hard X-rays (above 10 keV).

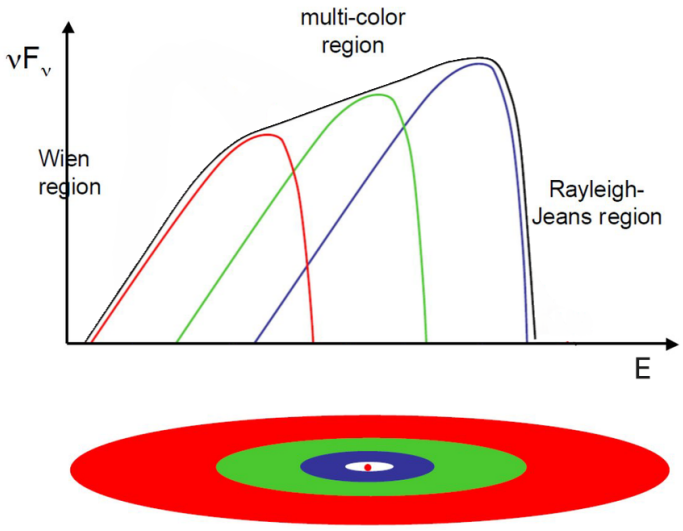

Figure 2.1. Simplified representation of the superposition of single-temperature blackbody emissions from different regions of an accretion disk around a black hole. (Adapted from Woitke 2015).

2.1.2 Corona

Besides the expected thermal disk blackbody, an additional component was ubiquitously detected already in the early observations of accreting stellar-mass and supermassive black holes (see, e.g., Haymes & Harnden 1970; Schreier et al. 1971; Lightman & Shapiro 1975; Elvis et al. 1978). This apparently non-thermal emission is shaped as a power law with a high energy cutoff, and is thought to originate from a hot ($\sim$ 100 keV or $\sim 10^9$ K) ionized, and optically thin ($\tau \lesssim 1$) plasma distribution, located close to the BH. This emitting region is commonly referred to as *corona*, and the nature of features such as its formation mechanism, its stability, and its geometry, constitute an active area of investigation. As for its emission, the most plausible scenario is that of Compton up-scattering of soft photons, emitted from the accretion disk, by hot coronal electrons. Through multiple scatterings a single source photon is Comptonized by electrons in the corona, resulting in a specific photon flux[2] $n(E) \sim E^{-\Gamma}$, where the photon index Γ will depend on the coronal optical depth τ, and electron temperature T_e.

The total seed spectrum from the disk is hence shifted to harder energies, as showcased in Figure 2.2, but limited by the electron energy $E_e = kT_e$. More specifically, as a source photon gains energy through consecutive scatterings, its energy approaches E_e, reducing the likelihood of further up-scatterings and resulting in an exponential rollover $\sim e^{-E/E_{\rm cut}}$.

[2]Specific photon flux is defined as the number of emitted photons per unit time, area and energy; and hence measured in *photons* s^{-1} cm^{-2}.

If we assume the disk to have uniform thickness along the radial direction (i.e., slab-like geometry) the cutoff energy $E_{\rm cut}$ is precisely determined by the coronal electron energy, $E_{\rm cut} \sim 2 - 3\, kT_e$, and is generally between 30 and 300 keV.

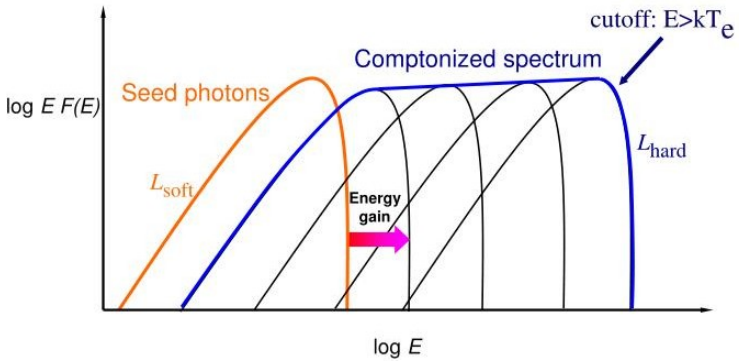

Figure 2.2. Non-thermal continuum spectrum $L_{\rm hard}$ originating from the energy gain due to the Comptonization of seed photons $L_{\rm soft}$ by hot (kT_e) coronal electrons. Image credits: A. Zdziarski (Centrum Astronomiczne M. Kopernika).

2.2 X-ray reflection spectroscopy

For some sources, however, modelling the spectrum with only a disk blackbody and a Comptonized continuum, is not sufficient. Namely, prominent residuals around 7 and $20 - 30$ keV, provide evidence for the need of a more sophisticated model. In fact, photons up-scattered in the corona can be emitted towards the accretion disk, where they may undergo various interactions and processes before finally escaping in the direction of the observer. Spectroscopical studies of the features imprinted into these *reflected* photons, can provide important insights about the inner accretion flow and the strong gravity region in which it is situated (e.g., Bambi et al. 2021).

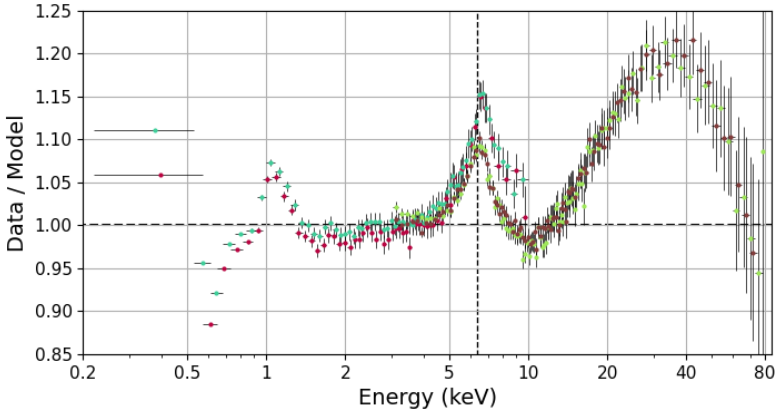

Figure 2.3. Observed relativistic reflection features of the BHXRB GX 339-4 from *NuSTAR* and *NICER* data (rebinned for visual purposes). The figure shows the ratio between data, and a model comprising thermal disk emission and a Comptonized continuum component.

2.2.1 Reflection spectrum

Being the accretion disk optically thick, incoming photons from the corona are reprocessed in the very upper layers of the disk itself (i.e., the disk atmosphere). Here, X-ray photons undergo photoelectric absorption ($\sigma_{\rm abs}(E) \sim E^{-3}$), and electron scattering ($\sigma_{\rm es}(E) \sim const.$), where the former (latter) process is dominant below (above) $E \approx 12$ keV.

Photons absorbed by atoms in the disk ionize a K-shell electron (n=1), leading to an absorption edge in the spectrum. An electron from the outer L-shell (n=2) will then fill the gap left in the K-shell by emitting an X-ray photon with energy equal to the transition energy between valence levels at play. At this point, if the emitted photon manages to escape, it contributes to a *fluorescence* line in the spectrum, otherwise it is reabsorbed and leads to the emission of a higher level electron called an Auger electron. Although many elements in the disk undergo this process, the probability for photoelectric absorption drastically increases for heavier species ($\sim Z^4$). Being iron the most stable (and hence one of the most abundant) elements, and considering the fact that the X-ray continuum flux decreases with increasing energy, fluorescent emission by neutral iron Kα at 6.4 keV results in the most prominent line in the spectrum.

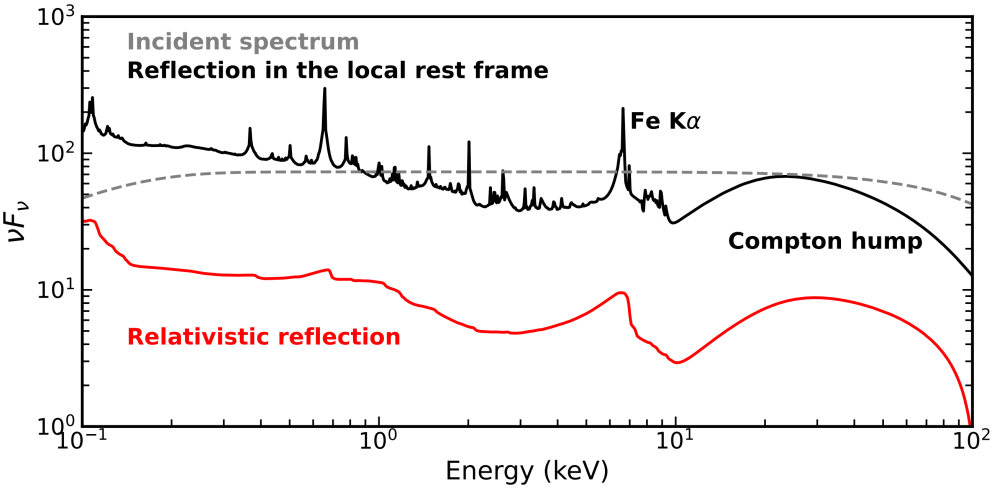

Figure 2.4. Local (black) and relativistic (red) reflection spectra for an accretion disk extending to the innermost stable circular orbit. Starting from an incident spectrum in the form of Comptonized continuum ($\Gamma = 2$, $kT_e = 60$ keV), the emission in the rest-frame of the gas in the disk is calculated with the `xillver` model, assuming an iron abundance with respect to the solar value $A_{\rm Fe} = 3$, and a ionization parameter $\xi = 100$ erg cm s^{-1}. Relativistic effects are computed by convolving the local reflection spectrum with the relativistic broadening kernel `relconv`, and are shifted downwards for visual clarity. Image courtesy of Honghui Liu.

As intuitive to think, if iron is ionized, the line shifts to higher energies: from 6.4 keV for Fe I, up to 6.9 keV for Fe XXVI. Several additional lines from other elements are also present below 4 keV, but result hardly distinguishable in the blurred spectrum detected by a distant observer. Together with emission lines, photoelectric effect also causes absorption edges, which for iron are placed between 7.1 keV (Fe I) and 9.3 keV (Fe XXVI). This, combined with Compton down-scattering of high energy photons, originates an excess above the power law continuum peaked around $20 - 30$ keV, namely the *Compton hump* (George & Fabian 1991).

The diagnostic power of X-ray reflection spectroscopy strongly relies on the effect that inner accretion disk physics has on the detected spectrum. In fact, the local reflection spectrum in the rest frame of the gas in the disk is profoundly modified by several relativistic effects driven by the strong gravity regime. For instance, Figure 2.5 shows how, starting from a narrow emission line in the local spectrum, rotation of the accretion disk will generate a two-sided line profile due to Doppler shift with respect to the observer. Owing to the relativistic motion of the disk material, the beaming effect will enhance the blueshifted peak. Furthermore, photons escaping the black hole's pull experience strong gravitational redshift, leading to a "red wing" in the line profile, more pronounced the closer their emission point is to the BH. The combination of all these features imprinted on the overall spectrum produces broadened and skewed emission lines, carrying insights about the physical parameters of the system.

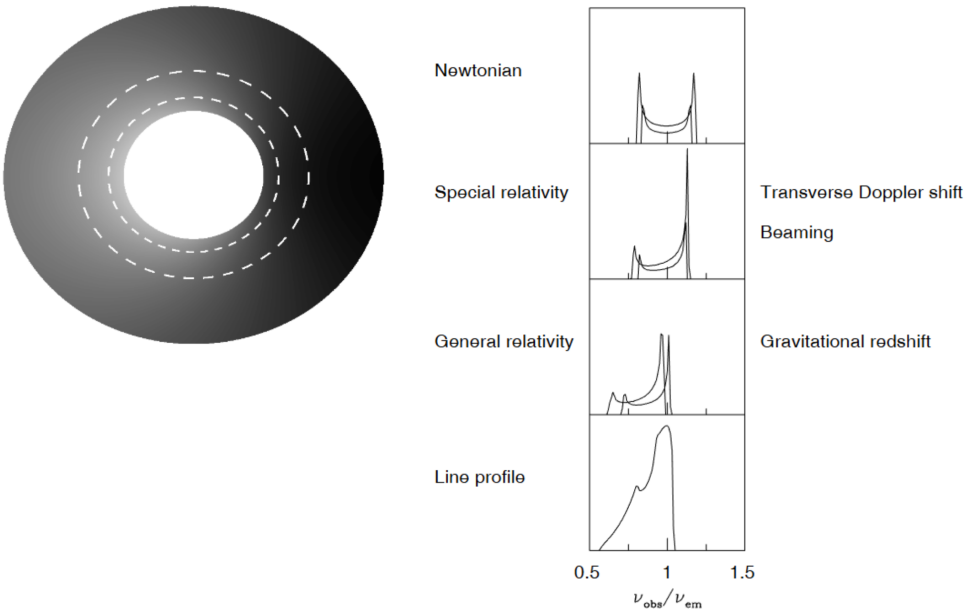

Figure 2.5. Representation of the relativistic effects modifying a narrow emission line with energy $\nu_{\rm em}$ (Fabian et al. 2000).

2.2.2 Impact of model parameters

Many physical parameters of the system have an impact on the shape of the reflection spectrum. To this end, it is possible to define the *ionization parameter*

$$\xi \equiv \frac{4\pi F}{n_e}\,, \tag{2.4}$$

where F is the incident flux from the corona between 13.6 eV and 13.6 keV, and n_e is the disk's electron number density. For lower ionization states more bounded electrons are available to interact with incoming photons, leading to more pronounced absorption and emission lines, with the opposite happening for higher ionization states. Furthermore, a larger density results in higher disk surface temperature due to enhanced free-free processes, also amplifying softer contributions to the spectrum, while higher elemental abundances (especially iron abundance A_{Fe}) strengthen line features.

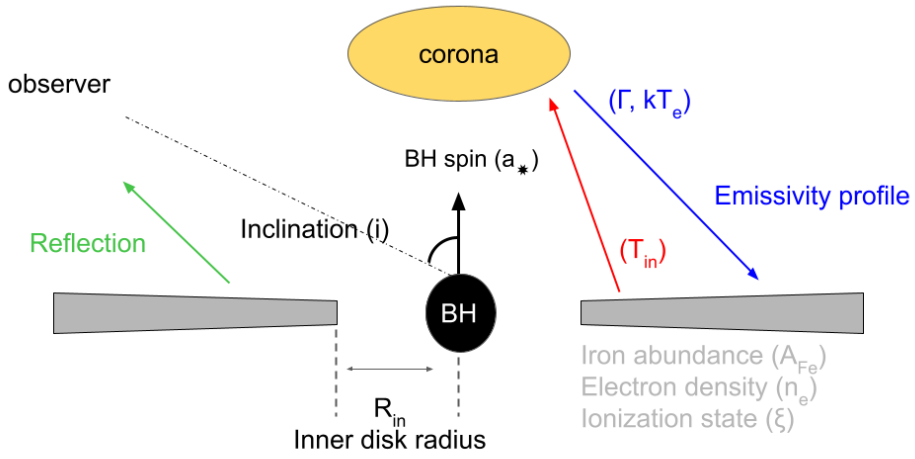

Figure 2.6. Sketch of the disk corona system, with the most relevant parameters contributing to the reflection spectrum.

The most crucial parameter for X-ray reflection spectroscopy is probably the inner accretion disk radius R_{in}, which can span from coinciding with the general relativistic innermost stable circular orbit (ISCO) radius R_{ISCO}, to being truncated far from it. R_{in} profoundly impacts the shape of the iron line: a disk extending all the way to the ISCO results in an elongated red wing of the broadened iron line. Moreover, being the ISCO a monotonic function of the BH spin, measuring R_{in} also provides a way to estimate the spin itself. The iron line profile is also modified by the inclination angle i between the BH spin axis and our line of sight: a more face-on view of the system leads the two peaks in the line profile to merge due to the absence of the Doppler effect.

The last determining factors are the characteristics of the coronal emission, which can be described by its photon index Γ, cutoff energy E_{cut}, and *emissivity profile*. The latter describes the radial dependence of the intensity of the reflected emission $\epsilon(r)$, by assuming a balance between this and the incident intensity at each point of the disk. Two main approaches can be taken: assuming a coronal geometry automatically determines an emissivity profile but makes the analysis model-dependent, while a more conservative model-independent approach can be taken by using a phenomenological broken power law profile

$$\epsilon(r) \sim \begin{cases} r^{-q_{\mathrm{in}}} & \text{for } r < R_{\mathrm{br}} \\ r^{-q_{\mathrm{out}}} & \text{for } r > R_{\mathrm{br}} \end{cases} , \tag{2.5}$$

where R_{br} is the breaking radius, and q_{in} and q_{out} respectively the inner and outer emissivity indices. Furthermore, if $q_{\mathrm{in}} = q_{\mathrm{out}}$ the emissivity is a simple power law.

2.3 Outbursts of Black Hole X-ray Binaries

Although not the only determining factor, mass accretion rate is crucial in shaping both spectral features and overall flux of radiation emitted by accreting black holes. Observing the associated spectral variability of AGN is strongly limited by the dynamical timescales of the processes at play, far out of reach for humanly-possible studies. For BHXRBs, however, the much smaller length scales involved in the phenomena make observing long-term evolutions of the accretion flow feasible. The majority of these sources are transient, and undergo frequent outbursts thought to stem from instabilities (e.g., thermal viscous and magnetorotational instabilities), triggering an increase in the mass accretion rate that can approach the Eddington limit, and last weeks to months.

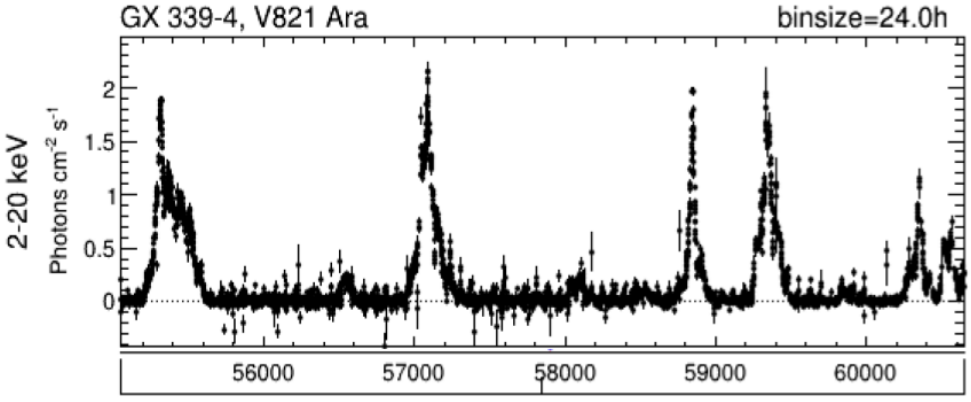

Figure 2.7. *MAXI* light curve showcasing the count-rate evolution of GX 339-4 in the time period between the years 2011 (∼ MJD 55500) and 2024 (∼ MJD 60500).

In particular, if mass transfer from the companion is greater than the accretion rate onto the central BH, matter starts accumulating in the cooler outer regions of the disk, causing a slow temperature rise. At around $\sim$ 4000 K, initially neutral hydrogen starts becoming ionized, driving a viscosity increase and allowing for more efficient outwards transfer of angular momentum. The accretion rate is therefore enhanced, resulting in an increasing X-ray luminosity, but also exceeding the binary mass transfer rate. This ultimately causes the disk's mass, temperature, and viscosity to drop, causing the luminosity to decay, and the outburst to end (Fender & Belloni 2012).

On this basis, it is possible to identify different *states* of a transient source, depending on the mass accretion rate and other physical properties, and possessing profoundly different spectral signatures. Transient BHXRBs spend most of their time in a *quiescent* state, namely a period of reduced accretion in which the X-ray source is relatively faint. During quiescence, the mass accretion rate is several orders of magnitude below the Eddington limit, and the spectrum is rather hard, with extremely low or completely absent soft emission from the disk.

In general, spectral states are set apart by comparing their *hardness ratio*:

$$\text{Hardness ratio} = \frac{\text{Hard X-ray flux}}{\text{Soft X-ray flux}}\,, \tag{2.6}$$

where the definition of hard and soft X-ray bands is case-dependent, without a strict convention adopted. During an outburst, the transition of a source between different spectral states can be tracked through its path in the hardness-intensity diagram (HID), a plot depicting the X-ray flux as a function of the hardness ratio. As shown in Figure 2.8, typical outbursts trace a peculiar *q-shaped* anticlockwise path in the HID, starting from quiescence and progressively increasing in flux and transitioning to softer spectral states before returning to their original hard and faint quiescent state.

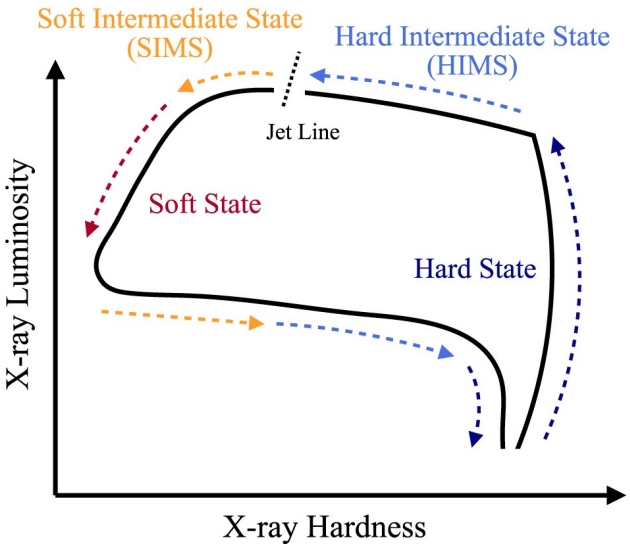

Figure 2.8. Simplified representation of the hardness-intensity diagram (HID) showing the temporal evolution of a typical outburst of BHXRBs (Adapted from Wang et al. 2022).

Low Hard State

While persistent black hole X-ray binary sources (e.g., Cygnus X-1) are observed as emitting at a somewhat steady X-ray flux, transient systems usually found in a quiescent state can transition into increased luminosity states due to mechanisms enhancing their accretion rate. When these mechanisms are triggered, the source starts undergoing an outburst by entering a state characterized by low luminosity and high hardness, thus deemed *low hard state*. Through the evolution the accretion rate increases, as does the luminosity, while hardness remains rather constant, hence we see a vertical transition in the HID. The spectrum is dominated by coronal non-thermal emission, with its characteristic power law shape having photon index $\Gamma \sim 1.6 - 1.7$ and a high energy cutoff, while the contribution of the disk thermal emission is negligible. Outflows are observed both in form of disk winds at lower energy bands (UV, optical, infrared (IR)), and of a compact radio jet (Belloni 2005).

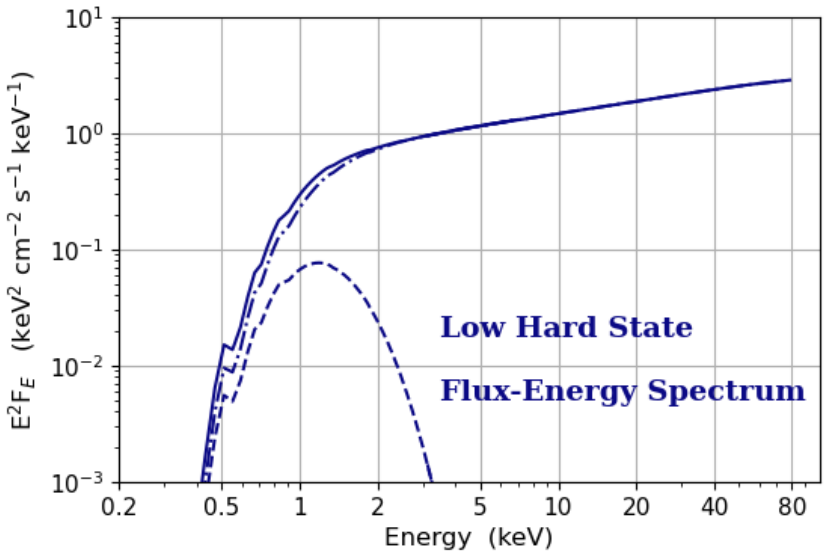

Figure 2.9. Spectrum of a hard state observation of GX 339-4 from *NuSTAR* and *NICER*.

Intermediate States

Through time, the luminosity continues to increase while simultaneously the spectrum becomes softer, corresponding to a rising contribution from the disk. In this *hard intermediate state* the radio emission becomes steeper, and the outflow velocity increases rapidly, originating a fast relativistic jet (Fender, Belloni, and Gallo 2004), marked in the HID by the crossing of a so-called "jet-line".

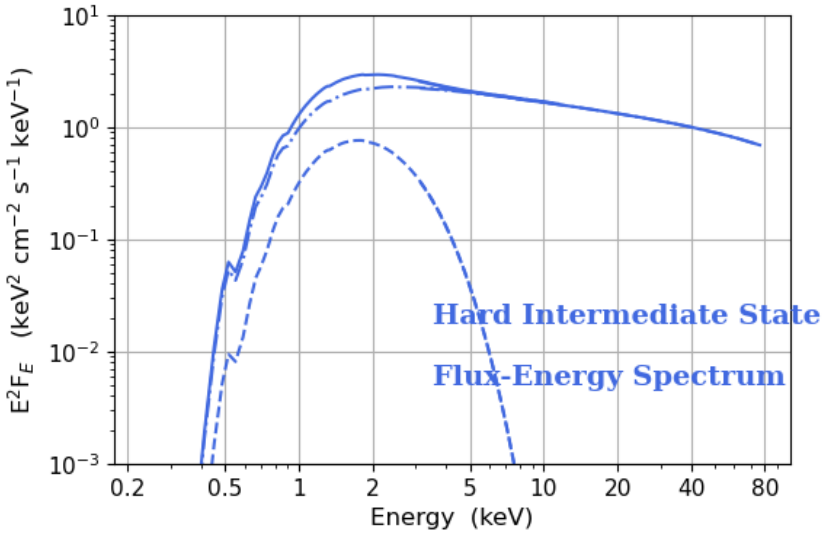

Figure 2.10. Spectrum of a hard intermediate state observation of GX 339-4 from *NuSTAR* and *NICER*.

During the phase transition, the source keeps moving along the top horizontal

branch in the HID with a progressive softening of the non-thermal continuum, reaching a photon index $\Gamma \sim 2.4 - 2.5$. In this *soft intermediate state* the thermal disk component starts dominating over the coronal power law, and the source reaches maximum brightness.

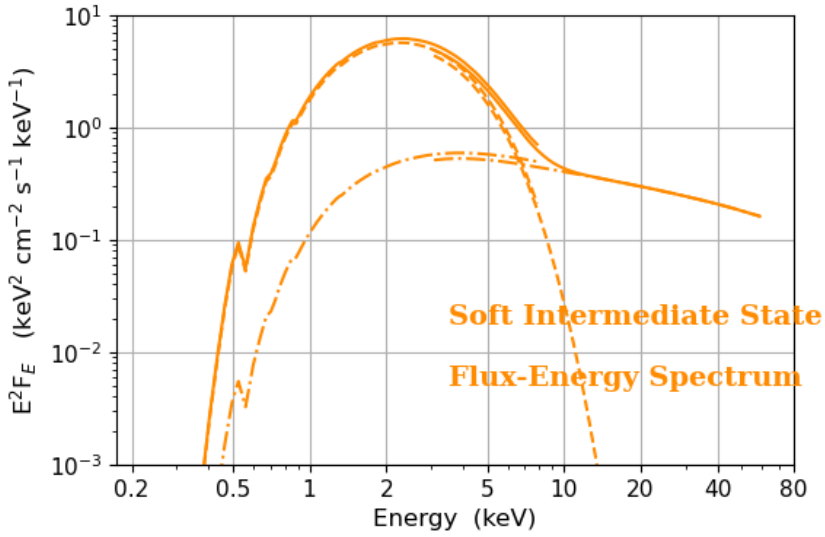

Figure 2.11. Spectrum of a soft intermediate state observation of GX 339-4 from *NuSTAR* and *NICER*.

High Soft State

The peak luminosity point also corresponds to the softest spectrum: the inner disk temperature reaches ~ 1 keV, with the thermal component being up to orders of magnitude brighter than the Comptonized continuum. Jet emission in the radio usually reduces down to becoming negligible, while other kinds of outflows such as disk winds can be detected in the X-rays. During this *high soft state*, the source's brightness starts gradually decreasing, initiating the decaying phase of the outburst.

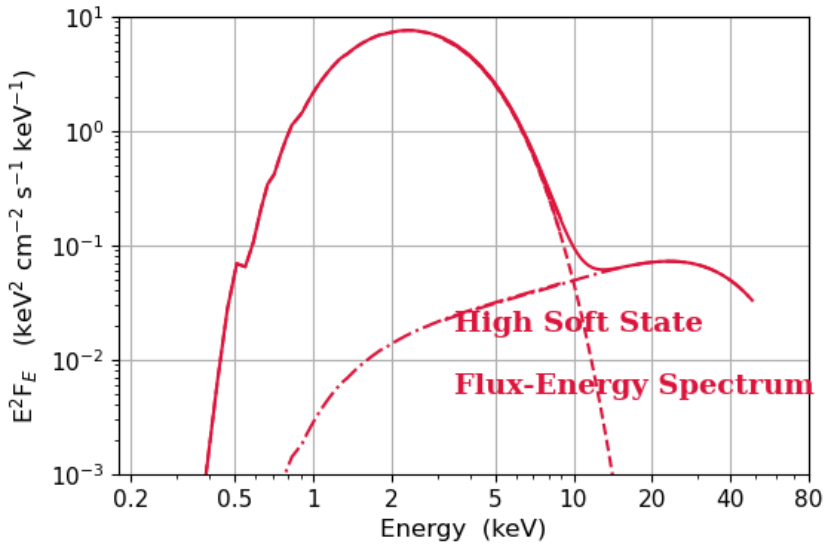

Figure 2.12. Spectrum of a soft state observation of GX 339-4 from *NuSTAR* and *NICER*.

After the luminosity decay following the high soft state, the source undergoes an opposite phase transition from softer to harder spectra. The outburst then ends with a progressive decrease of the mass accretion rate, leading the source to transition through intermediate states and low hard state for a second time, before eventually settling again in a quiescent state.

2.4 Open Questions

Leveraging X-ray reflection spectroscopy to study outbursts of BHXRBs provides an outstanding tool for tackling the many unanswered questions that still surround the field of black hole accretion. In the following paragraphs I will give an overview of the two major problems this thesis aims to investigate.

2.4.1 Inner Accretion Disk Radius

A marker to track BH systems' variability and spectral evolution is the inner radius ($R_{\rm in}$) at which the accretion disk is truncated, and matter transitions to a hot ($\sim 10^9$ K), optically thin flow radially plunging into the black hole. If the accretion rate is inside a certain range (i.e., $0.001\,\dot{M}_{\rm Edd} \lesssim \dot{M} \lesssim 0.3\,\dot{M}_{\rm Edd}$), a geometrically thin and optically thick disk forms. The inner regions of such a disk are capable of efficient radiative cooling, leading to temperatures of $\sim 10^7$ K for BHXRBs and $\sim 10^5$ K for AGN, and extend up to ISCO radius (Steiner, McClintock, et al. 2010).

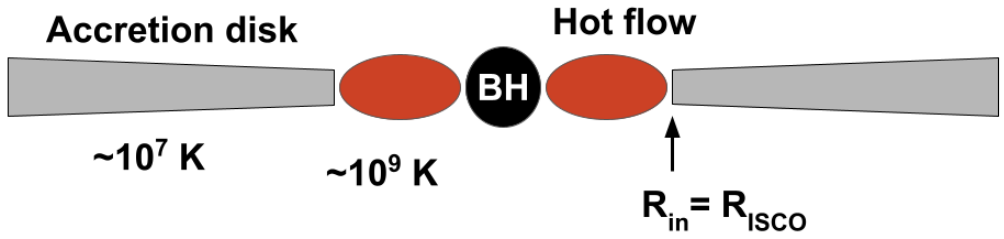

Figure 2.13. Schematic illustration of an accreting BH system comprising a geometrically thin and optically thick accretion disk (grey) extending up to the ISCO radius ($R_{\rm ISCO}$), and a hot flow of matter (red) plunging into the BH.

If the accretion rate is below some critical value ($\dot{M} \lesssim 0.001\,\dot{M}_{\rm Edd}$), the inner disk is expected to be truncated far from the ISCO radius, and replaced by a geometrically thick and optically thin advection-dominated accretion flow (ADAF) (Narayan and Yi 1994). Owing to the low density, the flow is unable to efficiently cool through the emission of radiation, and hence becomes much hotter ($kT_e \sim 100$ keV) than the inner disk temperature. This scenario is depicted in the sketch in Figure 2.14, and is expected to well model the behaviour of accreting BHs in quiescent and low hard states (Bambi et al. 2021), but is also found to be a possible unstable solution for larger mass accretion rates (e.g., Andrzej A. Zdziarski, Gierliński, et al. 2004).

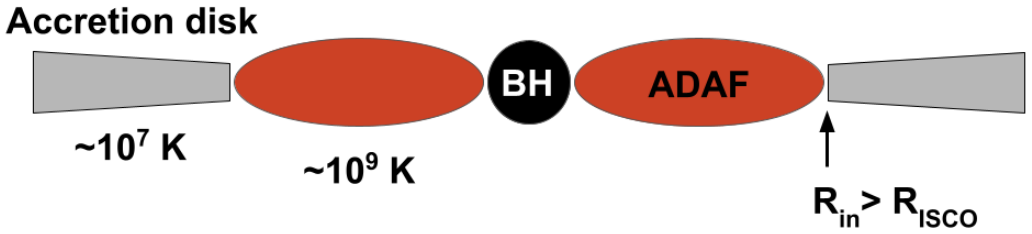

Figure 2.14. Schematic illustration of an accreting BH system comprising a truncated accretion disk (grey), and a hot, geometrically thick and optically thin flow of matter plunging into the BH as an advection-dominated accretion flow (red).

In intermediate accretion rate states however, the problem of disk truncation is still open, with many possibilities being investigated, and observational results still not being in perfect agreement with each other. The transition between truncated disk and disk at the ISCO could either happen smoothly, or abruptly. To this end, relativistic reflection spectroscopy is a crucial tool for investigating the evolution of the inner accretion disk regions throughout an outburst, and more specifically in the high-flux hard states such as the intermediate ones were open problems still lie. In fact, it is especially in such spectral states that reflection features are most prominent, providing an accurate probe of the inner disk truncation radius by constraining the shape of the red-tail of the iron line.

2.4.2 Coronal Geometry

X-ray reflection spectroscopy also enables investigating the nature of the corona, in an effort to broaden our understanding of its formation mechanism, stability, and geometry. In fact, there is still a lack of consensus about the mechanisms exploiting accretion power to fuel and sustain the hot and rarefied gas comprising it. Magnetohydrodynamic instabilities in the accretion flow, magnetic reconnection, and interaction with the black hole spin, could all be contributing factors, and lead to a static corona structure or to an outflowing scenario (e.g., Beloborodov 1999; Poutanen, Veledina, and Beloborodov 2023).

Although still unclear, the exact morphology of this hot plasma near the BH is of great importance, as it impacts the illumination and subsequent emissivity profile of the reflecting accretion disk (see, e.g., Wilkins & Fabian 2012; Gonzalez et al. 2017). Figure 2.15 showcases some examples of possible corona geometries.

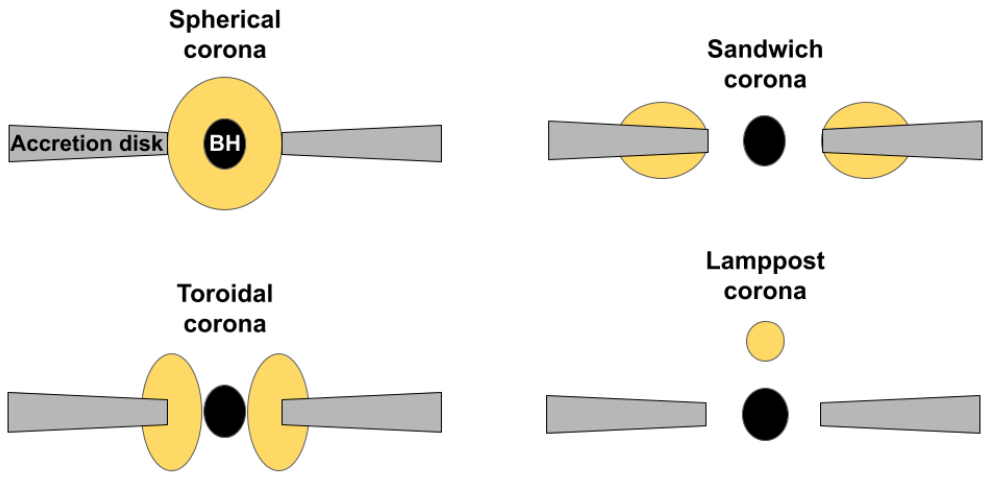

Figure 2.15. Sketch representation of possible corona geometries: spherical geometry (top left panel), sandwich geometry (top right panel), toroidal geometry (bottom left panel), and lamppost geometry (bottom right panel).

Shapiro, Lightman, and Eardley (1976) first introduced a scenario in which the inner region of the disk is hot and up-scatters soft photons from outer regions of the disk, while also enshrouding the black hole as a spherical corona. However, Imaging X-ray Polarimetry Explorer (*IXPE*; Weisskopf et al. 2022) data of Cygnus X-1 the seems to disfavour this spherical geometry, unable to produce the observed polarization signature (Krawczynski et al. 2022). These innovative results favour instead elongated coronae on the accretion disk plane, such as the so-called *sandwich* geometry, in which the corona is a hot, slab-like structure which might correspond to an accretion disk atmosphere (Haardt & Maraschi 1991; 1993); or a *toroidal* corona

which extends beyond the inner accretion disk radius (Poutanen & Svensson 1996) as an advection-dominated accretion flow (Esin, McClintock, and Narayan 1997).

Another model is that of a compact corona aligned with the black hole spin axis (Martocchia & Matt 1996), namely a *lamppost* geometry, which could physically be interpreted as the base of the jet (Markoff, Nowak, and Jörn Wilms 2005). Despite having been widely adopted for its simple implementation and good agreement with observational data, the lamppost corona model also seems to be disfavoured by recent results by Saade et al. (2024), who compared several works comprising *IXPE* observations of accreting BHs, and found the polarization signature to be mostly consistent with a slab-like corona and accretion geometry to be widely similar between supermassive and stellar-mass BHs.

Chapter 3

Scientific Case and Methods

In order to investigate the open problems described in the previous chapter, I conducted a broadband X-ray spectral analysis of a black hole X-ray binary, employing relativistic reflection spectroscopy techniques on data from the Nuclear Spectroscopic Telescope Array (*NuSTAR*; Harrison et al. 2013), and the Neutron star Interior Composition ExploreR (*NICER*; Gendreau et al. 2016). In this chapter, I will discuss the object of this study, namely GX 339-4, together with giving an overview of the selected observations of its outburst in 2021. Subsequently, I will present the data reduction process, giving an overview of the telescopes providing this data, before summarizing the spectral analysis models employed in this work.

3.1 The source: GX 339-4

GX 339-4 is commonly referred to as the archetypal black hole X-ray binary, owing to its transient nature, with frequent outbursts every 1-3 years, and prominent relativistic reflection features found in its spectrum in both hard and soft states (e.g., García et al. 2015; Miller et al. 2004; Liu et al. 2022). It was discovered in 1973 by Markert et al. (1973), and has since then been one of the most extensively studied accreting BH sources across all wavelengths. By analyzing its near-infrared spectrum, Heida et al. (2017) have constrained the mass of the BH to be between 2.3 and 9.5 $M_\odot$, and placed a lower limit to the distance at 5 kpc.

These results from direct observations are consistent with findings from spectral and timing analysis of GX 339-4 X-ray data (e.g., Parker, J. A. Tomsick, Kennea, et al. 2016; Sreehari et al. 2019), while in a recent work Zdziarski, Ziółkowski, and Mikołajewska (2019) implemented detailed evolutionary models for the companion star on data by Heida et al. (2017) and Buxton et al. (2012), finding a BH mass of $4 - 11$ $M_\odot$, a distance of $8 - 12$ kpc, and a binary inclination angle $37° < i < 78°$. The orbital period of the binary is estimated at $P_{\rm orb} = 1.7587 \pm 0.0005$ days, and the mass donor is thought to be a K1-2 type star measuring between 0.5 and 1.4 $M_\odot$ (Zdziarski et al. 2019), making the system a low mass X-ray binary.

Previous studies also found the black hole in GX 339-4 to be consistent with a high spin value ($a_* \approx 0.95$, García et al. 2015; Parker, J. A. Tomsick, Kennea, et al. 2016; $a_* > 0.86$, Liu et al. 2023). The inclination angle of the accretion disk has been consistently constrained by X-ray reflection spectroscopy measurements to be in the range 35 to 50 degrees (e.g., Liu et al. 2023, 2022; Wang-Ji et al. 2018; García et al. 2015).

Parameter	Value	Unit	Reference
Black hole mass	$4 - 11$	$M_\odot$	Zdziarski et al. 2019
Companion mass	$0.5 - 1.4$	$M_\odot$	Zdziarski et al. 2019
Distance	$8 - 12$	kpc	Zdziarski et al. 2019
Binary inclination	$37 - 78$	degrees	Zdziarski et al. 2019
Orbital period	1.7587 ± 0.0005	days	Zdziarski et al. 2019
Black hole spin	> 0.86		Liu et al. 2023

Table 3.1. Key parameters of the black hole X-ray binary GX 339-4.

Past GX 339-4 outbursts have been extensively studied using a wide array of telescopes, although results from different analyses have not always been consistent. For instance, Plant et al. (2015) reported the disk being largely truncated ($R_{\rm in} > 100 R_g$) throughout the entire low hard state (at luminosities $0.1\% - 15\%$ the Eddington limit) from several *X-ray Multi-Mirror* (*XMM-Newton*; Jansen et al. 2001) observations. Conversely, Fürst et al. (2015) utilized *NuSTAR* and *Swift X-Ray Telescope* (*XRT*; Gehrels et al. 2004; Burrows et al. 2005) observations of the 2013 hard-only outburst (i.e., the source failed to transition to a soft state), finding no evidence of a strongly truncated inner accretion disk radius $R_{\rm in} \lesssim 100\ R_g$ at luminosities spanning 1% to 6% $L_{\rm Edd}$.

Wang et al. (2018, 2020) investigated the low hard state of the 2015, 2017 and 2019 failed outbursts with *NuSTAR*, *NICER* and *Swift/XRT*, reporting modest truncation ($3\ R_g < R_{\rm in} < 15\ R_g$) between 0.5% and 5% $L_{\rm Edd}$ and larger truncation ($R_{\rm in} > 49\ R_g$) at luminosity 0.5% $L_{\rm Edd}$. Furthermore, Liu et al. (2023) considered precisely the 2021 outburst observed by the *Hard X-ray Modulation Telescope* (*Insight-HXMT*; S.-N. Zhang et al. 2020), and found $R_{\rm in}$ close to the ISCO ($R_{\rm in} \lesssim 3.2\ R_g$) for the whole hard to soft transition in the range $10\% - 35\%\ L_{\rm Edd}$.

In this context, our work provides an independent study of the 2021 outburst, leveraging the broad and continuous (i.e., without any gaps) spectral coverage and negligible pile-up effect of *NuSTAR* and *NICER*. By largely extending the luminosity range probed ($0.05\% - 20\%\ L_{\rm Edd}$) and refining the analysis techniques, this study offers new insights into the evolution of the inner accretion disk geometry.

Results are then compared with those of Liu et al. (2023) and other previous investigations to explore the consistency of disk truncation across different outbursts and luminosity regimes. Precisely to enable efficient comparisons with previous works, and to estimate the luminosity of the source and derive its Eddington ratio, a BH mass of 10 $M_{\odot}$ and a distance of 8 kpc are assumed for GX 339-4 in this thesis.

3.2 Observations of the 2021 outburst

At the beginning of 2021, a sudden flux increase from GX 339-4 was detected by the *Monitor All-sky X-ray Image* (*MAXI*; Matsuoka et al. 2009), drawing the attention of several telescopes around the globe. Among those, multiple observational campaigns of the source were conducted by *NuSTAR*, and by *NICER*, providing a wealth of data to thoroughly investigate the evolution of BHXRB accretion properties with outstanding broadband coverage and spectral resolution.

As displayed in Figure 3.1*MAXI* is a wide-field X-ray telescope mounted on the International Space Station (ISS), and performing a full sky survey of X-ray sources every 96 minutes (ISS orbit time). It was developed by the Japanese Aerospace Exploration Agency (JAXA) and launched in 2009, with the main objectives of providing early detection of X-ray transient events and long-term monitoring of the intensity fluctuation of known X-ray sources. *MAXI* light curve data products in four energy bands ($2-20$ keV, $2-4$ keV, $4-10$ keV, $10-20$ keV) were publicly available and obtained from the mission's website[1].

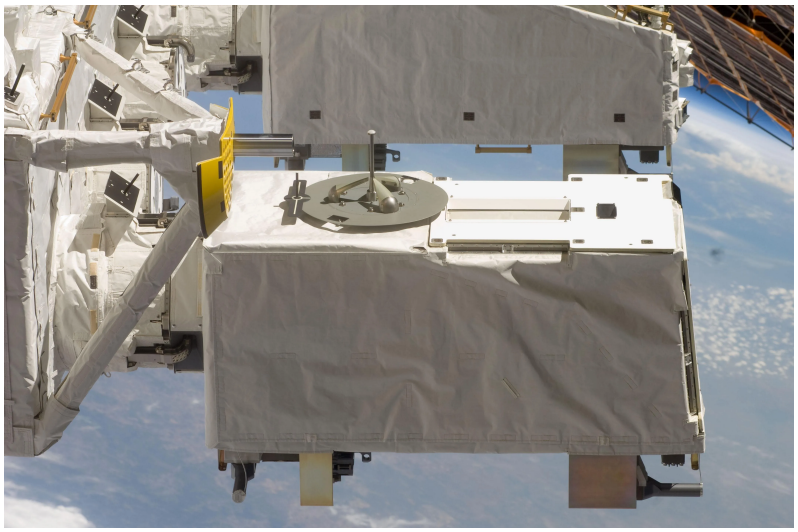

Figure 3.1. Side view of the *MAXI* sensor mounted on the Japanese Experiment Module - Exposed Facility aboard the International Space Station. Image credits: National Aeronautics and Space Administration (NASA).

[1] http://maxi.riken.jp/top/index.html

Mass accretion rate enhancement in GX 339-4 led to an outburst starting in late January 2021, with a transition back to quiescence taking place in early November of the same year. As showcased by Figure 3.2, this outburst was followed in its entirety by *MAXI*, and comprised a count rate increase by more than two orders of magnitude with respect to quiescence values of ~ 0.01 photons cm^{-2} s^{-1}.

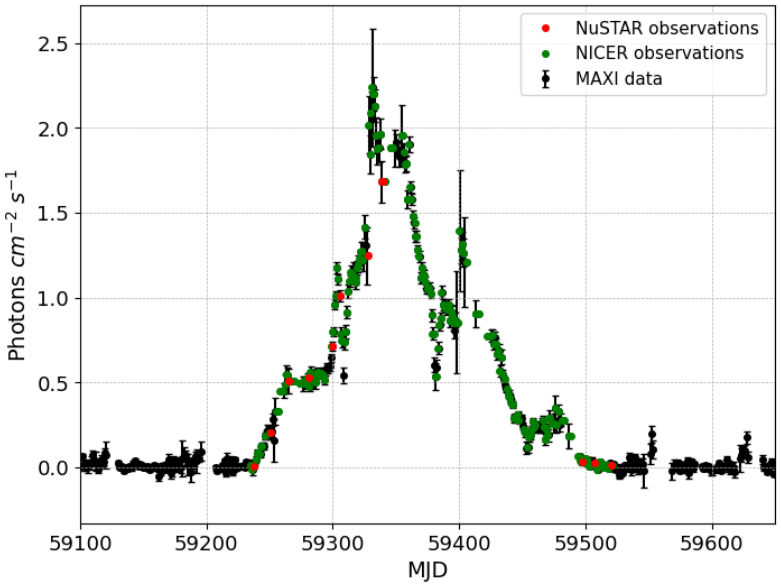

Figure 3.2. *MAXI* light curve of the 2021 outburst of GX 339-4. Observations by *NuSTAR* and *NICER* in the time frame of the outburst were projected onto the respective *MAXI* observation closest in time, hence they do not constitute an accurate representation of *NuSTAR* and *NICER* detected count rates, but merely a way to visualize and select observations on the basis of their date and time.

Since for the purpose of conducting X-ray reflection spectroscopy analyses, good coverage and spectral resolution in the hard X-ray band (especially between ~ 5 and ~ 40 keV) is crucial, the presence of *NuSTAR* observations was the discriminant factor in the evaluation of the dataset to be considered. Therefore, all of the 13 *NuSTAR* observations of GX 339-4 during the 2021 outburst were taken into account. To this regard, Figure 3.2 provides a complete overview of how *NuSTAR* data is widespread over the entire rise of the outburst, while for the decaying phase only three observations at its very end are present.

Aiming to extend the sensitivity in the soft X-ray band, quasi-simultaneous *NICER* data were also taken into consideration: observations ending up to one day in advance or starting up to one day following *NuSTAR* time frames, were grouped for spectral analysis as comprising a single observing epoch. Adopting this strategy resulted in a dataset including the 13 aforementioned *NuSTAR* observations, and 24 quasi-simultaneous *NICER* observations.

Furthermore, being 3 *NuSTAR* high flux observations quasi-simultaneous themselves, the complete dataset is composed of 11 different epochs. As already mentioned, the first 8 epochs are rather evenly-spaced and describe the rising part of the outburst up until its very peak, while the last 3 fall in the late decaying phase. Beyond broadening the energy coverage and improving spectral resolution, a multi-mission approach also contributes to strengthening the result's statistical significance by increasing the observing time and hence total counts, and to minimizing individual instrument-specific systematics (e.g., calibration uncertainties, detector responses, or background noise), enhancing the robustness and reliability of the analysis compared to single-instrument studies.

As a means to give a first categorization of the dataset, the HID of the outburst was plotted: Figure 3.3 gives a clear view of the complete source evolution. Most importantly, the diagram's q-shape, characteristic of BHXRB outbursts, gives a strong confirmation of the occurred state transition, and of the *NuSTAR* and *NICER* coverage of all spectral states during the hard-to-soft rise. From this description, reading the HID as a counter-clockwise transition gives the opportunity to roughly start subdividing epochs into low hard, intermediate and high soft states.

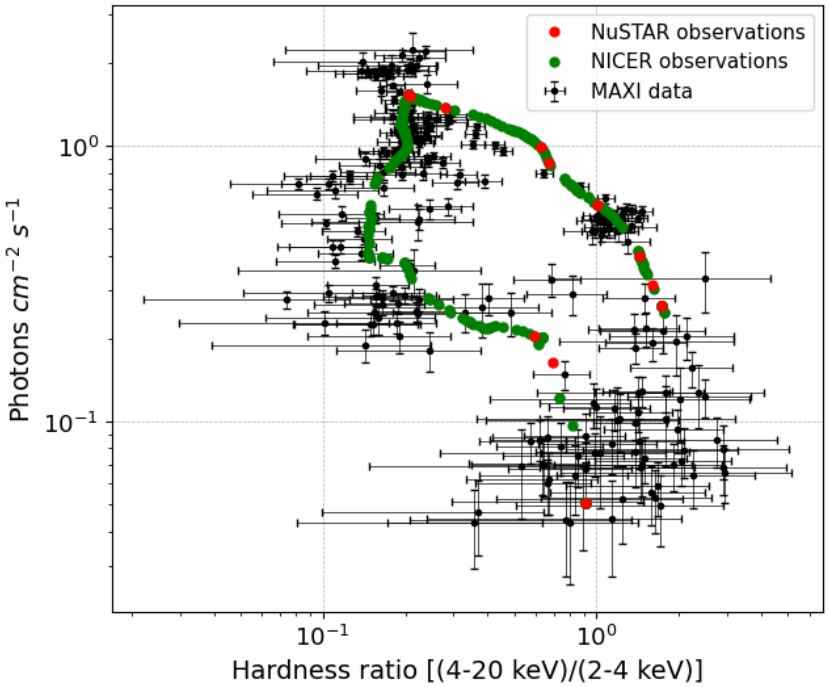

Figure 3.3. *MAXI* hardness-intensity diagram of the 2021 outburst of GX 339-4. For visual clarity, only data points with relative errors below 0.7 are plotted. Observations by *NuSTAR* and *NICER* in the time frame of the outburst were projected onto the respective *MAXI* observation closest in time, hence they do not constitute an accurate representation of *NuSTAR* and *NICER* detected count rates, but merely a way to visualize and select observations on the basis of their date and time.

3.3 Data Reduction and Products Extraction

A detailed overview of the complete dataset is provided in Table A.1. All *NuSTAR* and *NICER* data were publicly available and obtained from NASA's High Energy Astrophysics Science Archive Research Center (HEASARC)[2]. Furthermore, a thorough review of the dataset confirmed the absence of any flagged issues such as increased solar activity or non-standard instrument settings, ensuring all observations were suitable for processing through the respective pipelines and Calibration Database (CALDB), part of HEASARC's software suite (HEASoft).

3.3.1 NuSTAR

The Nuclear Spectroscopic Telescope Array is a mission of the NASA Small Explorers program launched on June 13, 2012, and still operational to this day. It was launched from Kwajalein Atoll in the Republic of the Marshall Islands into a low-Earth, near-equatorial orbit. *NuSTAR* originates from a collaboration between NASA's Jet Propulsion Laboratory and the California Institute of Technology, and is the first hard X-ray focusing telescope, opening a new window onto the high energy universe thanks to its broad observing bandpass and outstanding spectral resolution. It is equipped with a deployable mast, granting a 10.14 m focal length to its two co-aligned grazing-incidence conical optics (Hailey et al. 2010). *NuSTAR*'s telescopes consists of two separate Focal Plane Modules (FPMs) labelled FPMA and FPMB, similar but not identical. Each focusing optic has its own FPM, consisting of solid state Cadmium-Zinc-Telluride (CdZnTe) pixel detectors (state-of-the-art room temperature semiconductors), with by a Cesium-Iodide (CsI) anti-coincidence shield surrounding the detectors' housings (Harrison et al. 2010). Each focal plane (or detector unit) comprises four CdZnTe sensors placed in a 2×2 array, and measuring arrival time, energy and position of the interaction of each incident X-ray.

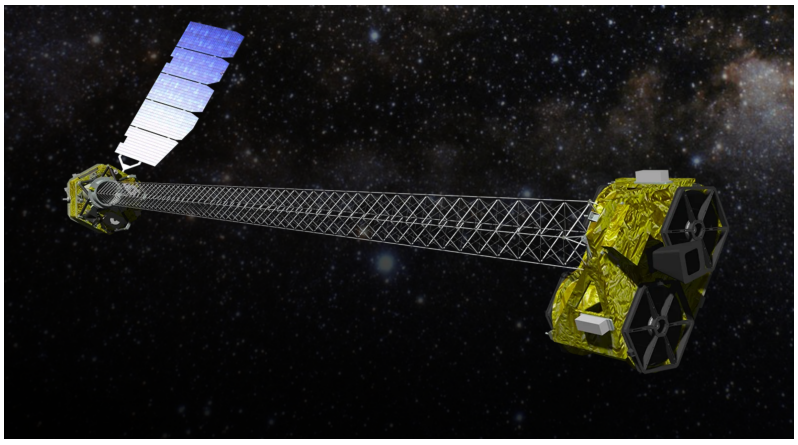

Figure 3.4. Artist's concept of *NuSTAR* on orbit. Image credits: NASA/Jet Propulsion Laboratory.

[2] https://heasarc.gsfc.nasa.gov/

NuSTAR covers a wide energy bandpass from 3 keV to 79 keV, extending the sensitivity of focusing far beyond the $\sim$ 10 keV high energy cutoff which limited most previous X-ray satellites. It offers exceptional energy resolution of 400 eV at 10 keV and of 900 eV at 60 keV (full-width half-maximum, FWHM), and a temporal resolution of $\sim$ 0.1 ms. The angular resolution is of 18 arcseconds (FWHM) with a $12' \times 12'$ field of view, providing high spatial resolution and sensitivity over a broad sky area. Furthermore, the detectors' readout system is able to avoid pulse pile-up (i.e., multiple incoming photons being detected as a single higher-energy event) and can measure fluxes with 1% accuracy even at incident rates up to 10^4 counts per second (Harrison et al. 2010).

NuSTAR observations were processed with the latest NuSTAR Data Analysis Software (NuSTARDAS) package version 2.1.4 released on August 22, 2024, as part of HEASoft version 6.34, and employing CALDB fpm20240812 calibration files. As recommended by the *NuSTAR* Team, Stage 1 and 2 data processing was performed through the `nupipeline` script, which automatically runs in sequence all the necessary calibration tasks for both FPMA and FPMB, and generates calibrated, cleaned and filtered Level 2 event files[3]. More specifcally, Stage 1 data reduction comprises various calibration steps, such as bad pixels flagging, energy and gain correction, and the conversion of raw coordinates into sky coordinates; while Stage 2 is devoted to the screening of event files by calculating passages of the South Atlantic Anomaly, filtering and generating Good Time Intervals, generating sky exposure maps, and calculating detector focal plane and optics coordinates from sky coordinates.

Subsequently, for each cleaned and calibrated Level 2 event file, the source was extracted from a region centered on GX 339-4 coordinates and enclosed in a radius of 100 arcseconds. Similarly, the background was extracted from a circular, source-free region of radius 130 arcseconds in the opposite corner of the detector. Figure 3.5 (a) and (b) show an example of source and background regions extraction on the *SAOImage DS9* application, respectively for FPMA and FPMB.

[3]For more detailed information on the data reduction and product extraction practices recommended by the *NuSTAR* Team, refer to the NuSTARDAS users guide at `https://heasarc.gsfc.nasa.gov/docs/nustar/analysis/nustar_swguide.pdf`

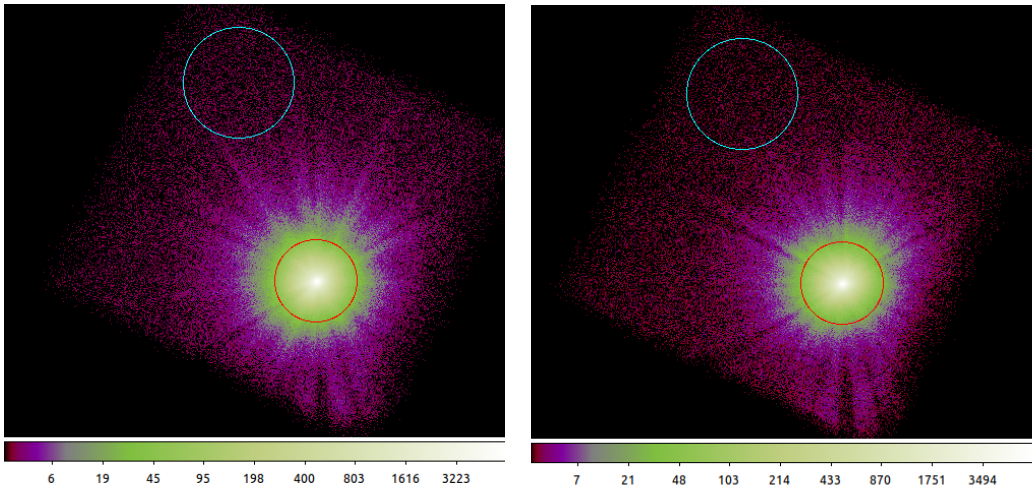

(a) FPMA source and background regions. **(b)** FPMB source and background regions.

Figure 3.5. *SAOImage DS9* visualization of the Level 2 Event file from a *NuSTAR* intermediate state observation (ObsID 90702303005) from both Focal Plane Modules. The time-integrated counts are shown in logarithmic scale, as well as the source (red) and background (cyan) selected circular regions for products extraction.

Finally, Stage 3 is dedicated to computing high-level scientific products, extracted from the processing of Level 2 event files and of other auxiliary files generated during previous data reduction steps. In this regard, the `nuproducts` task was used to generate source and background light-curves and spectra, redistribution matrix and ancillary response files, and source image file in sky coordinates, in order to implement spectral analysis as described in the following section.

3.3.2 NICER

The Neutron star Interior Composition ExploreR is a NASA Explorer Mission of Opportunity launched on June 3, 2017, from the John F. Kennedy Space Center in Florida, and deployed as an external attached payload aboard the International Space Station. The observatory is led by NASA's Goddard Space Flight Center in collaboration with the Massachusetts Institute of Technology. NICER's hearth is the X-ray Timing Instrument (XTI), an highly modular collection of 56 co-aligned X-ray concentrators acting as grazing-incidence optics (Balsamo et al. 2012; Okajima et al. 2016), each with an associated silicon-drift detector (Prigozhin et al. 2016).

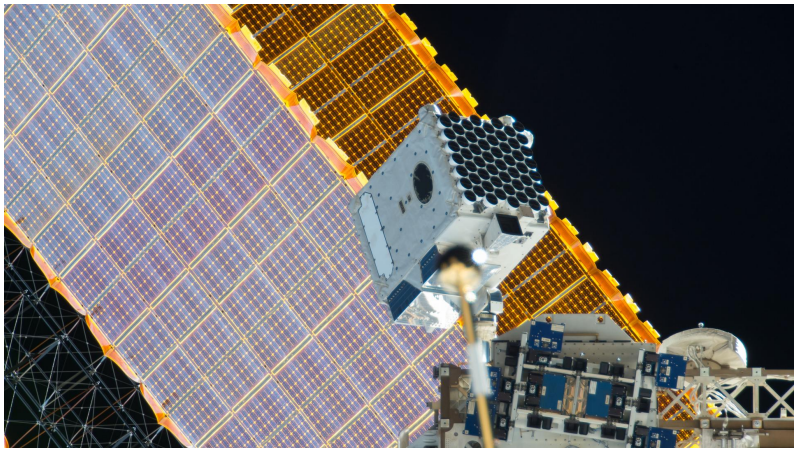

Figure 3.6. External view of *NICER*'s X-ray Timing Instrument mounted on the International Space Station. Image credits: NASA.

XTI provides high-throughput and low-background soft X-ray timing and spectroscopy. More specifically, it is capable of an unprecedented time-tagging resolution of under 300 ns, the highest of any astronomy instrument previously flown, and great energy resolution in its 0.2-12 keV bandpass (85 eV at 1 keV, and 137 eV at 6 keV; Prigozhin et al. 2016). Furthermore, *NICER* is free from photon pile-up effects, a vastly problematic issue which has caused significant systematics in previous X-ray reflection spectroscopy studies (e.g., Miller et al. 2006; Reis et al. 2008; Done & Diaz Trigo 2010).

NICER observations were processed employing the latest NICER Data Analysis Software (NICERDAS) version 12 and the CALDB xti20240206 calibration files released on February 27, 2024. The steps recommended by the *NICER* Team were followed by running the standard pipeline processing script, `nicerl2`, designed to perform Level 2 analysis including calibration, screening, and filtering of *NICER* data. Furthermore, extraction of high-level scientific products was performed with the dedicated pipeline tools `nicerl3-lc` and `nicerl3-spect`, generating light-curves, source and background spectra, and instrumental response and effective area files. Background spectra were computed by employing the *scorpeon* model, which takes into account contributions from the South Atlantic Anomaly, cosmic rays, polar and precipitating electrons, the cosmic X-ray background and galactic X-ray halo, and other non-X-ray backgrounds.

3.4 Spectral Analysis and Models

All resulting *NuSTAR* and *NICER* spectra were associated with their respective background and instrumental response files, and grouped with the `ftgrouppha` task in HEASoft. Using the optimal binning strategy (Kaastra & Bleeker 2016), and the additional constraint of a minimum of 30 counts per spectral bin with the *optmin*

mode, ensured good statistical significance to each spectral bin, therefore enabling the use of the χ^2 statistics to find best-fit values. Spectral analysis was conducted with `XSPEC v12.14.1` (Arnaud 1996), a command-driven, interactive, X-ray spectral fitting-program, which is completely detector independent, and currently the most widely-used spectral analysis software in high energy astrophysics.

With the aim to work with the broadest possible spectral band for each individual epoch, all non-background-limited data was considered for each observation, only ignoring spectral bins with signal-to-noise ratio $S/N > 1$, and those outside of the *NuSTAR* $(3 - 79$ keV) and *NICER* bandpass $(0.2 - 12$ keV). This approach is justified by the grouping of data with an optimal binning strategy and a minimum of 30 counts per bin, which ensures the validity of χ^2-based statistical fitting methods, as the Gaussian approximation for uncertainties holds. The balance between leveraging the full spectral information and maintaining robust fitting procedures, especially crucial in extremal spectral regions where the signal is faint but still statistically significant, is key to accurately constrain the coronal temperature, highly dependent on the high energy cutoff.

Table A.2 provides a detailed overview of each Epoch's noticed energy range for spectral analysis with `XSPEC`, from which is already possible to notice some spectral features of the observations. For instance, Epochs 5 through 8 showcase a progressive decrease of the *NuSTAR* S/N at high energies, owing to the weakening of the harder non-thermal component consistent with a hard-to-soft state transition. Although Epochs 10 and 11 also show a reduced *NuSTAR* energy band, a similar reduction of the high energy range can be observed in *NICER* data as well, suggesting the S/N decrease to stem from lower count rates. The same is not observed for the previously considered observations, which maintain stable S/N for the hard range of *NICER* spectra.

The analysis and fitting of spectra evolving across different epochs of the outburst has required the use of several `XSPEC` models for the individual components presented in Chapter 2.1 and 2.2. Absorption by grains in the interstellar medium (ISM) was accounted for via the Tübingen-Boulder multiplicative models (Wilms et al. 2000), which calculate the observed spectrum on the basis of the galactic extinction of the emitted X-rays. In particular, `TBabs` allows for fitting the sole equivalent hydrogen column density n_H, while `TBFeO` additionally enables estimating the oxygen O and iron Fe abundances, and redshift z.

The soft thermal component was described with the `diskbb` multicolor disk model (Mitsuda et al. 1984), assuming an optically thick and geometrically thin disk, with a temperature profile $T(r) \propto r^{-3/4}$ leading to the observed spectrum being a superposition of blackbody radiation from annuli at different temperatures, and depending from the inner disk temperature $T_{\rm in}$ and a normalization factor.

In order to model the hard X-ray component, two different models were tested, namely `nthComp` (Zdziarski et al. 1996; Życki et al. 1999) and `simplcut` (Steiner et al. 2017). The former is an additive model, and describes the spectrum produced by inverse Compton scattering of soft seed photons in a hot corona depending on a seed photon temperature $kT_{\rm bb}$, an asymptotic power law photon index Γ, an electron temperature kT_e, and a normalization factor. Conversely, the latter is a convolution model aimed at providing a fully self-consistent description of the Comptonization process. More specifically, it ensures that the Compton power law photons once originated as thermal disk emission by linking the two with a scattered fraction parameter $f_{\rm sc}$ (i.e., fraction of accretion disk photons which are Compton scattered by the corona) depending on the geometry and optical depth of the corona; and also accounts for the possibility of reflection photons being once again Compton scattered by the corona (see the reflection Comptonization component in Figure 3.7). `simplcut` gives the possibility to choose between two scattering kernels: `nthcomp` itself, and a custom exponential cutoff implementation[4]. Besides $f_{\rm sc}$, other model parameters are, as for `nthcomp`, the spectral index Γ, the electron temperature kT_e shaping the high energy cutoff, substituted by $E_{\rm cut}$ for the second scattering kernel, and a reflection fraction $R_{\rm F}$ defined as the ratio between scattered photons which return to illuminate the disk and those reaching infinity.

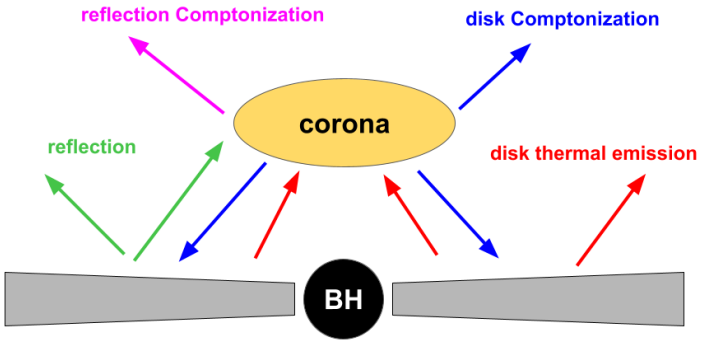

Figure 3.7. Sketch of the disk-corona model with the main spectral components: disk thermal emission (red), Comptonization of seed disk photons (blue), reflection of coronal emission (green), Comptonization of the reflection component (magenta).

As regards the reflection component, spectral modelling of relativistic reflection features started with the simple superposing of the iron Kα broadened emission edge to the standard thermal and power law components (e.g., `diskline` by Fabian et al. 1989; and `laor` by Laor 1991). The quality of current spectral data, however, has allowed for the development of advanced spectral models which take into consideration the complete local reflection spectrum (e.g., `reflionx` by Ross & Fabian 2005; and `xillver` by García & Kallman 2010). The observed reflection spectrum

[4]For additional information refer to Steiner et al. 2017

is then computed by applying a convolution model to the accretion disk rest-frame reflection, which accounts for broadening of line profiles due to relativistic effects. However, this approach neglects possibility of observing photons emitted with angle θ_e different from the disk inclination angle i, due to the effect of light bending in the strong gravity region. Therefore, the current most advanced reflection models directly combine local reflection and relativistic effects, while also taking into account deflection of light rays by the black hole's gravitational field (e.g., `relxill` by García et al. 2014; Dauser et al. 2014; and `kyn` by Dovčiak et al. 2004). For a comprehensive review of the development and comparisons between reflection models see, e.g., Bambi et al. 2021.

This work made use of `relxill`[5], which combines the `xillver` reflection code and the `relline` broadening kernel (Dauser et al. 2010), and currently is the most popular and most advanced reflection model. Similarly to Figure 2.6, `relxill` describes an observed spectrum depending on key parameters of the accretion disk such as inclination angle i, inner disk radius $R_{\rm in}$, electron density n_e, ionization state ξ, and iron abundance $A_{\rm Fe}$; on coronal emission properties (photon index Γ, electron temperature kT_e, and emissivity profile); and on the black hole spin a_*. Another important parameter is the reflection fraction R_f, defined as the ratio of the intensity of the primary source irradiating the disk and the intensity directly going to infinity (Dauser et al. 2016)[6].

[5] `https://www.sternwarte.uni-erlangen.de/~dauser/research/relxill/`

[6] Note that this reflection fraction is not the same as the one defined in the `simplcut` model

Chapter 4

Spectral Fitting Results and Discussion

This chapter presents the results and discussion of the spectral analysis grounded on methods and model components described in Chapter 3. Two primary models were employed for this study: a continuum-only model (M1) to assess baseline spectral properties, and a reflection-inclusive model (M2) to conduct a detailed investigation of accretion disk truncation and coronal geometry. Both models considered for the analysis described herein make use of the elemental abundances measured in Wilms et al. (2000), and of photoelectric cross section values by Verner et al. (1996). Uncertainties are reported at 90% confidence level unless specifically noted.

The following section provides an overview of M1 fitting results, which serve as a benchmark for identifying the reflection signature analyzed and discussed in later sections.

4.1 Model 1 (no reflection)

As a means to assess the presence and strength of reflection features, the 11 epochs were first individually fitted with a simple absorbed continuum model (M1). This model comprises a multicolor disk component (`diskbb`) representing the thermal disk emission, a Comptonized component (`nthComp`) describing the high energy emission from up-scattering of disk photons in the corona, and an absorption component (`TBabs`) accounting for X-ray absorption by the ISM along the LoS. Instrumental cross-normalizations were included via `constant` factors to address any flux calibration offsets between instruments. The final model in `XSPEC` notation reads:

```
constant × TBabs × (diskbb + nthComp) .
```

In order to assure consistency between model components, the $T_{\rm in}$ `diskbb` parameter was tied to the $kT_{\rm bb}$ parameter of `nthComp`. Furthermore, since *NuSTAR* observations are composed by FPMA and FPMB data, the former was taken as reference

by freezing its cross-normalization constant to one, while constants for FPMB and *NICER*'s XTI were left free to vary independently for each epoch. In case of multiple observations by the same telescope in a single epoch, cross-normalization constants referring to the same instrument were tied to each other. The same approach was adopted for Model 2, described in the following section.

In Table 4.1, presenting M1 spectral fitting results, the magnitude of χ^2 values over degrees of freedom (d.o.f.) clearly indicates this model constitutes a rather poor fit to the data. In fact, apart from the last two epochs in the decaying part of the outburst, every other fit presents one or more strong contributions to the residuals due to both astrophysical and instrumental effects. For instance, the discrepancies between different *NICER* observations in Epochs 1, 5 and 9 clearly show that the source variability can be so intense to produce significant flux differences even on timescales of hours.

Data below 2 keV show an evident excess in the residuals, which seems to get stronger with increasing flux and soft disk emission during the rise of the outburst, while still maintaining a certain characteristic shape. Being ubiquitously present in mild-to-strong soft emission epochs, and consistent between different *NICER* observations in a same epoch, the nature of these residuals may be instrumental (i.e., stemming from XTI calibration systematics). This issue is known and documented in the literature (see, e.g, Adegoke et al. 2024; Svoboda et al. 2024; Steiner et al. 2024), and an astrophysical contribution to this effect cannot be excluded. In particular, it has been suggested that the excess might be partly imputable to absorption edge structures and related effects being more complicated than captured by `TBabs` and `TBFeO` as well as most other interstellar medium absorption models.

Furthermore, focusing on higher energies promptly reveals features we would expect to originate from relativistic reflection. In fact, M1 residuals across most epochs present a prominent excess around 6.4 keV followed by strong absorption around $7 - 12$ keV, and, in some cases, by a large hump between 15 and 40 keV. These features are largely consistent with relativistic reflection signatures, and hence motivate further analysis incorporating a model taking into account the reprocessing of hard coronal photons in the accretion disk atmosphere which will be described in the coming Section 4.2.

Although generally speaking best-fit results for M1 parameters cannot be confidently interpreted as statistically meaningful, owing to the poorness of the fits themselves, some considerations and trends can nonetheless be extrapolated from Table 4.1. Firstly, despite not being fully consistent between different epochs, estimates for hydrogen column density along the LoS indicate values $\sim 0.55 - 0.65 \times 10^{22}$ cm^{-3}, in agreement with previous reflection spectroscopy studies of GX 339-4 (e.g., Liu et al. 2022), and slightly higher than galactic N_H surveys reporting values of $\sim 0.39 \times 10^{22}$

Epoch	N_H (10^{22} cm^{-3})	$T_{\rm in}$ (keV)	Γ	kT_e (keV)	$\chi^2/d.o.f.$
1	$0.66^{+0.01}_{-0.02}$	0.14±0.01	$1.57^{+0.006}_{-0.008}$	93^{+243}_{-35}	4349/798
2	0.56±0.01	$0.31^{+0.03}_{-0.01}$	$1.616^{+0.002}_{-0.003}$	95^{+31}_{-17}	3540/651
3	$0.586^{+0.007}_{-0.004}$	$0.29^{+0.01}_{-0.004}$	$1.68^{+0.002}_{-0.001}$	990^{p}_{-496}	6806/769
4	0.562±0.005	$0.331^{+0.007}_{-0.009}$	1.704±0.001	1000^{p}_{-493}	7701/858
5	0.703±0.002	$0.532^{+0.005}_{-0.007}$	2.283±0.003	1000^{p}_{-42}	24071/847
6	0.573±0.002	0.828±0.001	2.38±0.01	1000^{p}_{-235}	6109/703
7	0.597±0.002	0.850±0.001	$1.96^{+0.03}_{-0.02}$	36^{+47}_{-10}	2758/653
8	0.617±0.002	0.843±0.001	1.53±0.03	8.0±0.5	2451/874
9	0.52±0.01	0.251±0.008	1.68±0.004	1000^{p}_{-651}	4614/919
10	$1.2^{+0.3}_{-0.2}$	0.13±0.02	$1.69^{+0.02}_{-0.01}$	940^{p}_{p}	338/280
11	$0.7^{+0.03}_{-0.02}$	0.1^{f}	$1.73^{+0.03}_{-0.02}$	997^{p}_{p}	332/318

Table 4.1. M1 best-fit results for each Epoch. ^{p} and $_{p}$ flags indicate the parameter was pegged at the upper or lower bound during the fitting process, implying a lower or upper limit respectively, while ^{f} indicates the parameter was frozen during the fit.

cm^{-3} (HI4PI Collaboration 2016; Kalberla et al. 2005; Dickey & Lockman 1990). The inner accretion disk temperature and photon index behave as expected, increasing with the progressive mass accretion rate enhancement throughout the outburst, corresponding to a hotter disk and softer spectra, and going back to low hard state typical values for the last three epochs. Furthermore, the high energy excess driven by the Compton hump significantly hinders the fits' constraining power on the cut-off energy in the hard X-rays, and hence on the coronal electron temperature. A similar effect might also lead to the unexpectedly low power law photon index values for Epochs 7 and 8, in which the source is supposed to be in a soft state ($\Gamma \sim 2.5-3$).

In the following pages, M1 best-fit spectra and residuals are presented in chronological order from Figure 4.1 to Figure 4.6, giving a first overlook of the anticipated state transition of the source. The red thermal disk component, and overall flux, progressively get stronger until reaching the outburst peak in Epoch 8, where, conversely, the blue coronal emission is at its weakest. Subsequently, the outburst decay described by Epochs 9, 10 and 11, presenting a decreasing flux trend (reduced by up three orders of magnitude between the outburst peak and the last epoch) and weakening disk component.

(a) Epoch 1

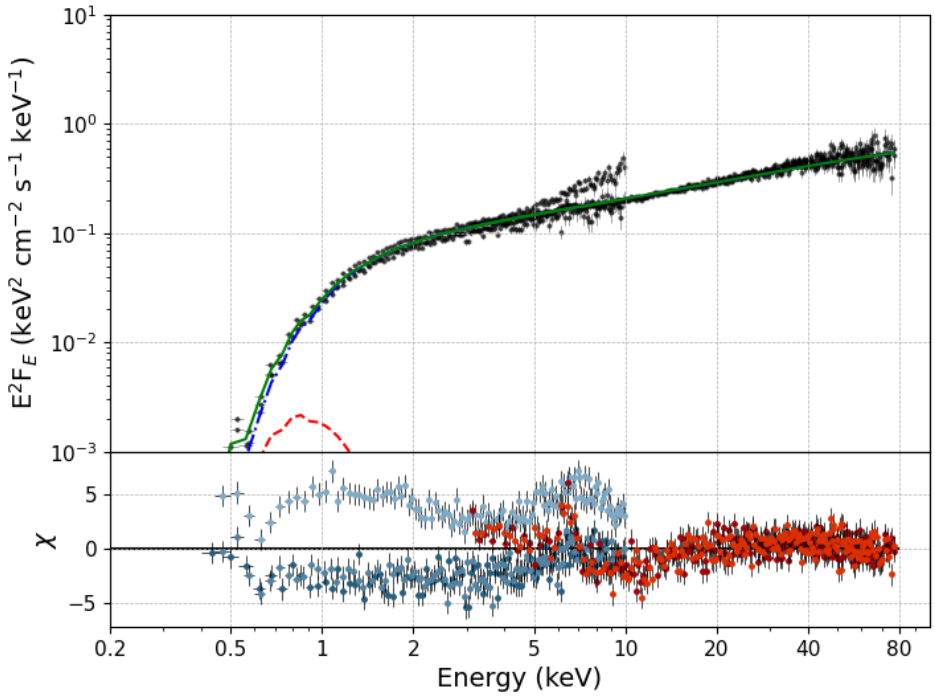

(b) Epoch 2

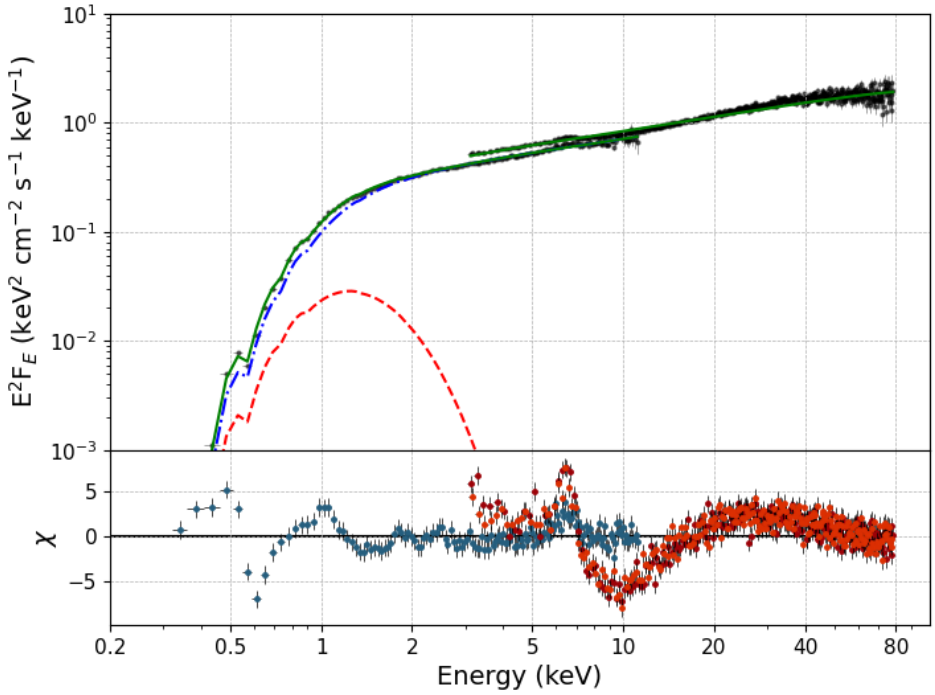

Figure 4.1. M1 best-fit spectrum for GX 339-4 in Epoch 1 (a) and Epoch 2 (b). The upper panels show *NuSTAR* and *NICER* data (black data points), the best-fit spectrum (green solid line), the continuum component (red dashed line), and the Comptonization component (blue dashed-dotted line). The lower panels indicate the residuals between *NICER* XTI observations (navy blue gradient) and *NuSTAR* FPMA (dark red) and FPMB (orange) observations, and the best-fit model (black solid line).

(a) Epoch 3

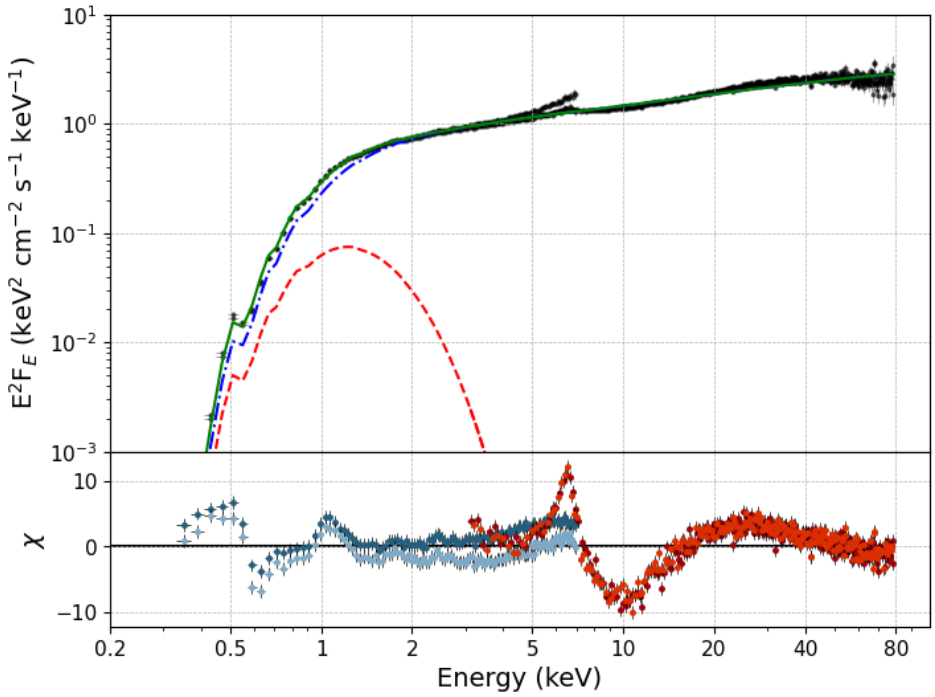

(b) Epoch 4

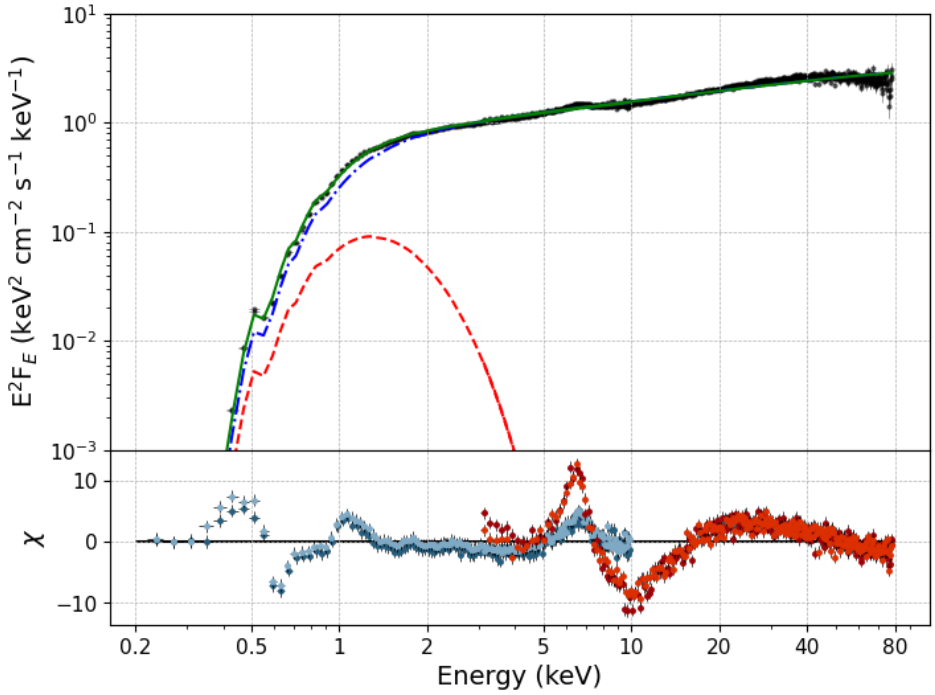

Figure 4.2. M1 best-fit spectrum for GX 339-4 in Epoch 3 (a) and Epoch 4 (b). The upper panels show *NuSTAR* and *NICER* data (black data points), the best-fit spectrum (green solid line), the thermal disk component (red dashed line), and the Comptonization continuum (blue dashed-dotted line). The lower panels indicate the residuals between *NICER* XTI observations (navy blue gradient) and *NuSTAR* FPMA (dark red) and FPMB (orange) observations, and the best-fit model (black solid line).

(a) Epoch 5

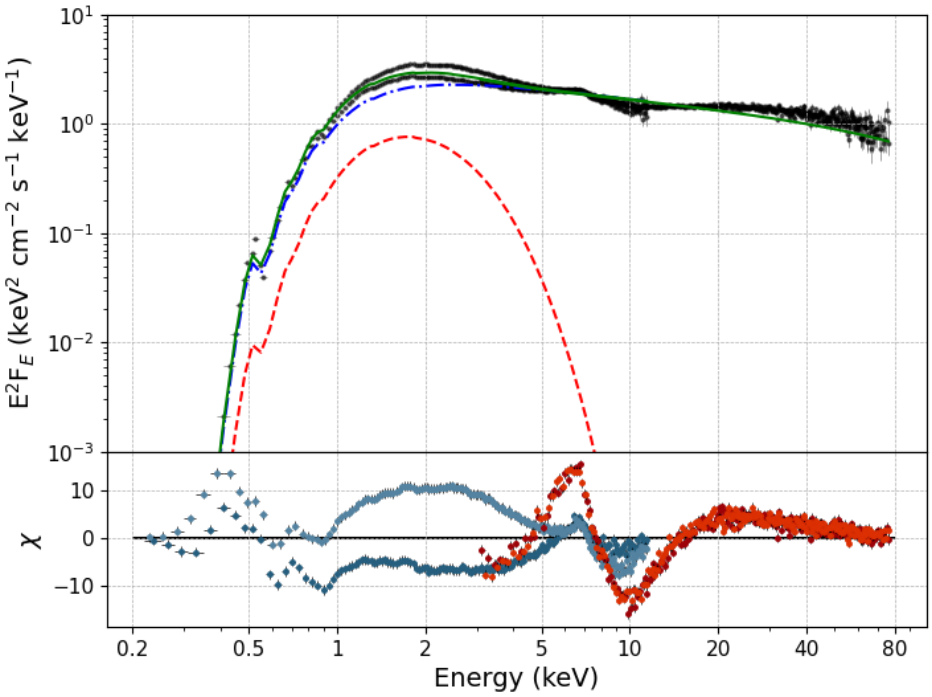

(b) Epoch 6

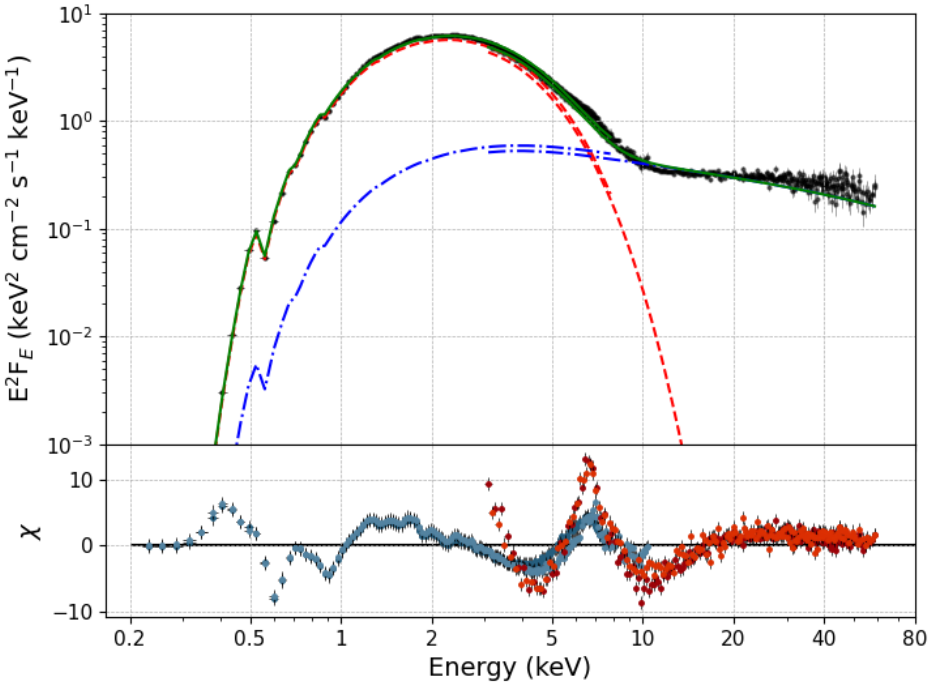

Figure 4.3. M1 best-fit spectrum for GX 339-4 in Epoch 5 (a) and Epoch 6 (b). The upper panels show *NuSTAR* and *NICER* data (black data points), the best-fit spectrum (green solid line), the thermal disk component (red dashed line), and the Comptonization continuum (blue dashed-dotted line). The lower panels indicate the residuals between *NICER* XTI observations (navy blue gradient) and *NuSTAR* FPMA (dark red) and FPMB (orange) observations, and the best-fit model (black solid line).

(a) Epoch 7

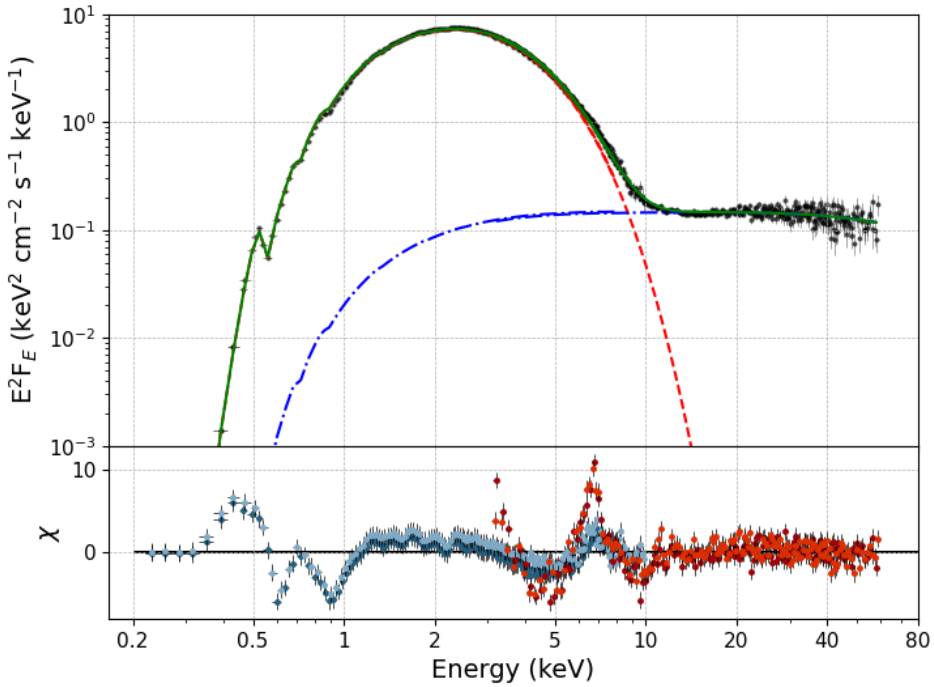

(b) Epoch 8

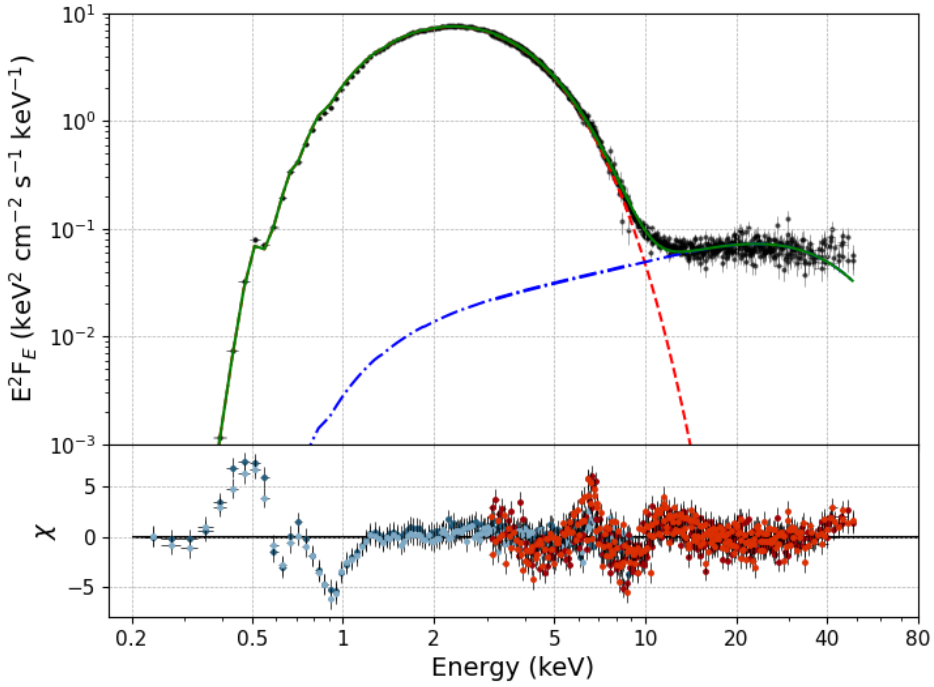

Figure 4.4. M1 best-fit spectrum for GX 339-4 in Epoch 7 (a) and Epoch 8 (b). The upper panels show *NuSTAR* and *NICER* data (black data points), the best-fit spectrum (green solid line), the thermal disk component (red dashed line), and the Comptonization continuum (blue dashed-dotted line). The lower panels indicate the residuals between *NICER* XTI observations (navy blue gradient) and *NuSTAR* FPMA (dark red) and FPMB (orange) observations, and the best-fit model (black solid line).

(a) Epoch 9

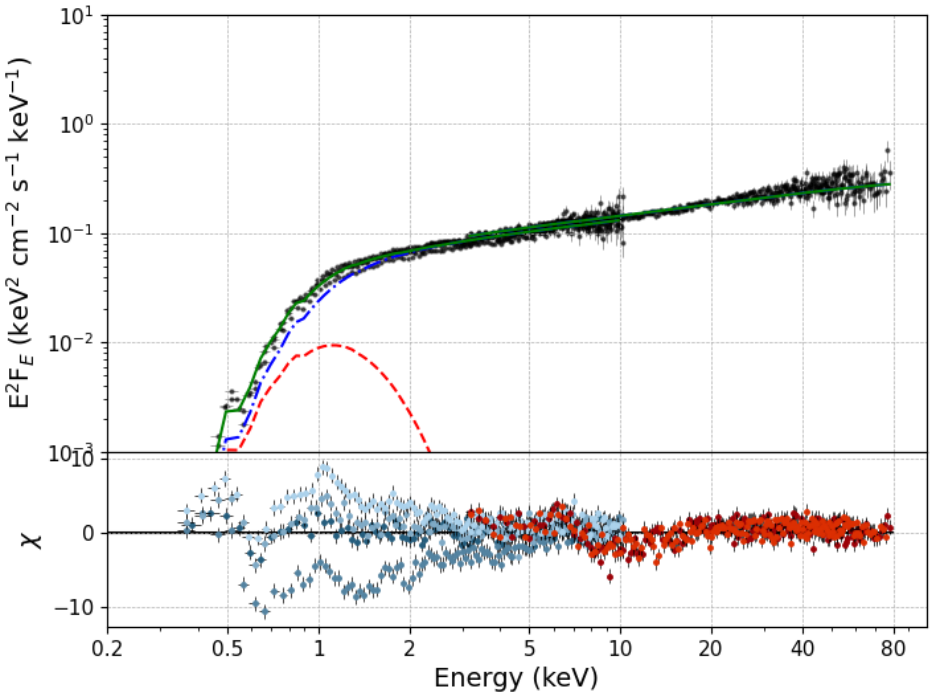

(b) Epoch 10

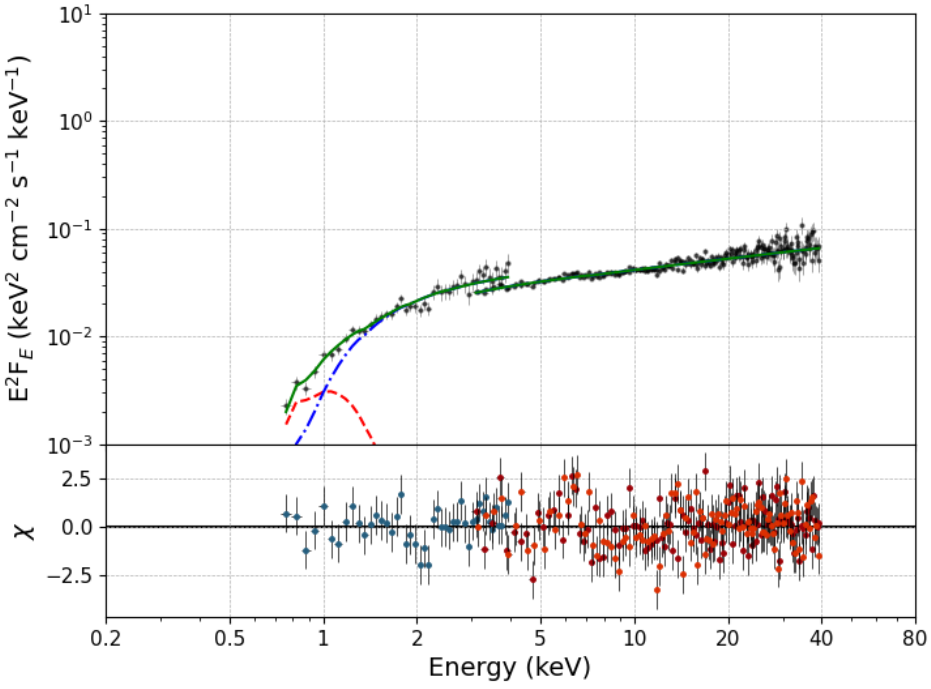

Figure 4.5. M1 best-fit spectrum for GX 339-4 in Epoch 9 (a) and Epoch 10 (b). The upper panels show *NuSTAR* and *NICER* data (black data points), the best-fit spectrum (green solid line), the thermal disk component (red dashed line), and the Comptonization continuum (blue dashed-dotted line). The lower panels indicate the residuals between *NICER* XTI observations (navy blue gradient) and *NuSTAR* FPMA (dark red) and FPMB (orange) observations, and the best-fit model (black solid line).

(a) Epoch 11

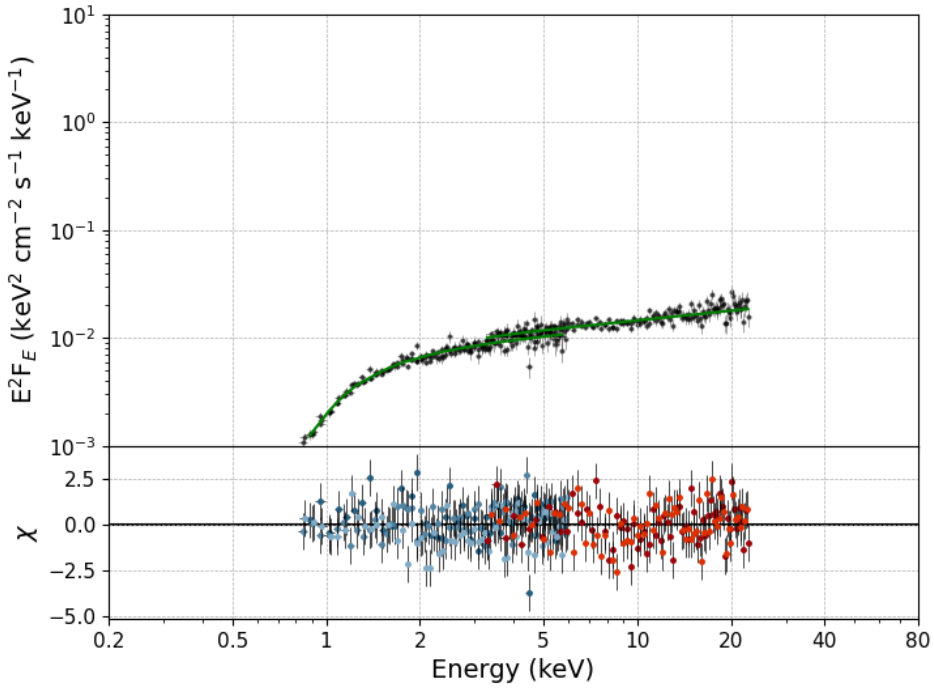

Figure 4.6. M1 best-fit spectrum for GX 339-4 in Epoch 11 (a). The upper panels show *NuSTAR* and *NICER* data (black data points), the best-fit spectrum (green solid line), the thermal disk component (red dashed line), and the Comptonization continuum (blue dashed-dotted line). The lower panels indicate the residuals between *NICER* XTI observations (navy blue gradient) and *NuSTAR* FPMA (dark red) and FPMB (orange) observations, and the best-fit model (black solid line).

The valuable insights both into possible systematics affecting the data, and into the physical behaviour of the source, given by M1 spectral fitting, will be treated more thoroughly in the following section by implementing a reflection-inclusive model.

4.2 Model 2 (reflection-inclusive)

To fully characterize the impact of disk reprocessing on the spectrum, a second, more complete model (M2) was considered. The most important change with respect to M1 was the introduction of the `relxillCp` component, where the "Cp" suffix indicates that the seed spectrum illuminating the disk is a power law continuum originating from Comptonization. `relxill` models do not allow for an arbitrary illuminating spectrum, but instead consider Comptonization originated from a seed disk temperature of $kT_* = 50$ eV resulting in a power law extending to energies uder 0.1 keV and thus an overprediction of low energy flux of BHXRBs (Ubach et al. 2024). For the purpose of solving this issue, we implemented the

`nthratio`[1] model component, which is based upon `nthComp` and used to first-order correct the aforementioned `relxill` soft excess.

The second step was to include a self-consistent treatment of Comptonization with `simplcut`. This convolution model implementation, however, brought some incompatibilities with `nthratio`: the definition and behaviour of the power law high energy cutoff in `simplcut` triggered several model computation errors for `nthratio`. In particular, values of kT_e below 25 keV seemed to destabilize the overall fitting process by conflicting with `nthratio`'s soft energy normalization. This occurrences ultimately led to the consideration of alternatives for correcting `relxill`'s low energy flux overestimation.

Thus, as a substitute to `nthratio`, a multiplicative broken power law model `mbknpo` was adopted following the approach of Svoboda et al. 2024. This model applies a break to the power law shape of the reflection component below a certain reference energy, hence causing the photon spectrum to have a turn over and follow the red tail of a multicolour disk below this energy, preventing the unphysical runaway flux issue. In `XSPEC` notation `mbknpo` is defined as:

$$\texttt{mdef mbknpo}\ \ \frac{\max(E,B)-B}{|E-B+\epsilon|}+\left(1-\frac{\max(E,B)-B}{|E-B+\epsilon|}\right)\cdot\left(\frac{E}{B}\right)^{I}\ \texttt{: mul}\ , \tag{4.1}$$

where B is the break energy, I is the index used for the correction at $E < B$, and $\epsilon \equiv 10^{-7}$ is a constant to prevent the divergence of numerical calculations. Throughout the spectral fitting process, the break energy is fixed to $B = kT_{\rm disk} \times 4.5$, derived from empirical exploration of Comptonization models (Ubach et al. 2024), and the spectral index is fixed to $I = \Gamma - 1.5$ (Svoboda et al. 2024, Steiner et al. 2024), where Γ is the photon index of the illuminating component.

In order to assess the combination of *NICER* instrumental features under 2 keV and the complex LoS-dependent ISM composition, resulting in the prominent excess in the soft band residuals discussed in Section 4.1, the `TBabs` interstellar medium absorption model was replaced by `TBFeO`. The new configuration enabled exploring non-solar abundance settings for oxygen and iron, vastly improving the spectral fits quality. The complete model (M2) is the following:

```
constant × TBFeO × (simplcut × (diskbb + relxillCp × mbknpo)) .
```

The remaining residuals were then treated by introducing narrow emission edges and absorption gaussians, by employing the `edge` and `gabs` model components in

[1] https://github.com/garciafederico/nthratio

XSPEC. Figure 4.7 gives an overview of the effect this approach had on the fitting process by comparing selected best-fit results for M2 with and without accounting for the remaining soft band *NICER* features with two `edge` components. In this instance, the great similarity in the features' shape across different observing epochs provides support for their interpretation as originating from imperfect instrumental calibration. The improvements in the total χ^2 were calculated to be $\Delta\chi^2 = 22$, $\Delta\chi^2 = 215$, $\Delta\chi^2 = 156$, and $\Delta\chi^2 = 85$ corresponding to four additional d.o.f., respectively for Epochs 5, 6, 7, and 8, fully supporting the approach taken.

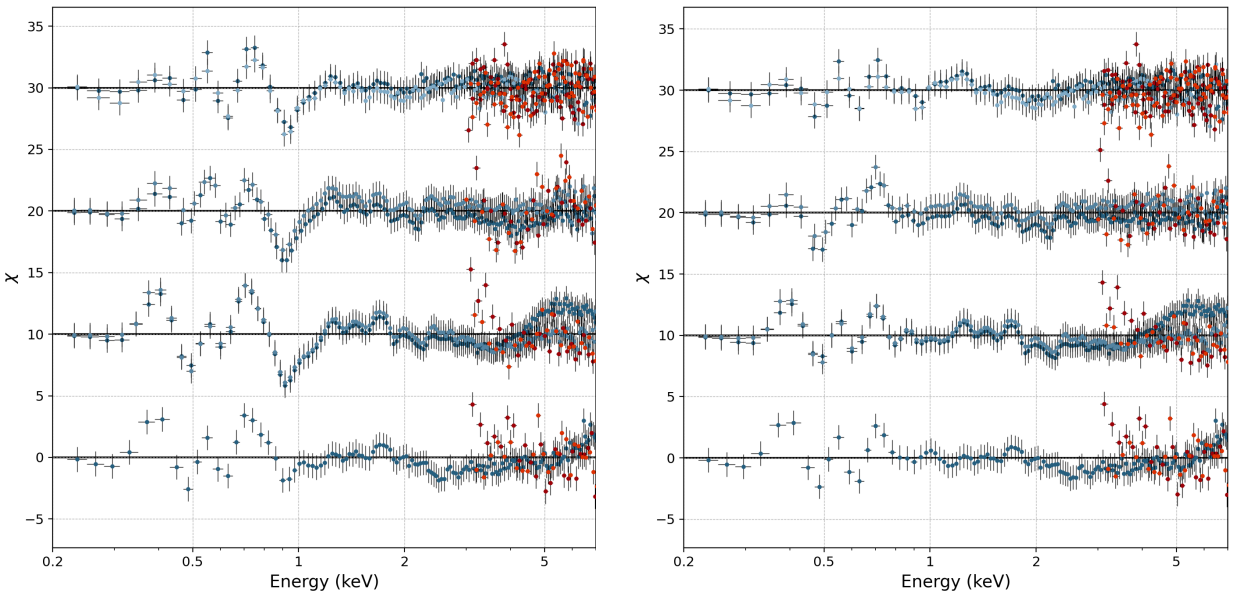

Figure 4.7. Residuals between *NICER* XTI observations (navy blue gradient) and *NuSTAR* FPMA (dark red) and FPMB (orange) observations, and the best-fit for M2 (black solid line), for Epochs 5, 6, 7, and 8, corresponding to the soft state of the source. Epochs are vertically shifted for visual purposes, and are ordered from bottom (thus corresponding to Epoch 5) to top (Epoch 8). The right panel shows the complete model, considering narrow edges to fit remaining line features in the soft band; while the left panel is produced without the introduction of gaussian absorptions and edges.

All M2 spectral fitting was performed tying together model parameters across all the *NICER* and *NuSTAR* observations in a same epoch, with the obvious exception of cross-normalization constants. Additionally, common parameters between model components, such as `simplcut`'s and `relxillCp`'s Γ and kT_e, were tied together to assure consistency. Unless otherwise indicated, the spin parameter of the BH was fixed to its maximal value of $a_* = 0.998$, while, being the source galactic, the redshift was fixed to zero. The reflection fraction parameter in `relxill` was fixed to -1, as the continuum component is already provided by `simplcut`, while the reflection fraction parameter in `simplcut` itself was fixed to 1 in order to avoid degeneracy with the scattering fraction. A phenomenological power law emissivity

with index q was assumed, since implementing a broken power law profile failed to bring even a modest improvement of the fits for any epoch, therefore indicating a power law emissivity is enough to fit the data.

Joint fitting for interstellar absorption parameters estimation

For the sake of conducting a consistent and accurate treatment of interstellar absorption, and considering that $N_{\rm H}$, Fe and O columns should be the same regardless of the source state, joint fitting of several epochs throughout different spectral states was performed to best estimate column densities, and then utilize the inferred values for fitting individual epochs. To best incorporate the phase transition, together with low hard and high soft states, the analysis was performed by combining and jointly fitting Epochs 1, 4, 5, 6, and 9 with M2.

In this process, state-independent parameters such as instruments' cross-normalization constants, absorption edges below 2 keV, disk inclination i, disk iron abundance $A_{\rm Fe}$, and most importantly $N_{\rm H}$, Fe and O interstellar abundances, were tied together between epochs; while all the remaining state-dependent parameters (i.e., Γ, $f_{\rm sctr}$, kT_e, $T_{\rm in}$, $R_{\rm in}$, q, $log\,\xi$, and $log\,N$) were tied together between observations of a same epoch, but left free to vary between different epochs corresponding to different source states. The results of the spectral fitting are presented in Table 4.2.

$N_{\rm H}$ (10^{22} cm^{-3})	O (solar)	Fe (solar)	χ^2 / $d.o.f.$	$\chi^2_{\rm red}$
0.58 ± 0.01	1.26 ± 0.04	$1.15\ ^{+0.07}_{-0.09}$	5033 / 3496	1.440

Table 4.2. M2 joint fitting results for ISM elemental abundances. Oxygen and iron abundances are given with respect to the solar value.

Furthermore, as already mentioned in Section 4.1, the source showed variability so intense to produce significant flux differences even on timescales of hours, leading to prominent discrepancies between different *NICER* observations belonging to the same epoch, either due to enhanced source variability, or to increased background levels. For instance, M1 spectral fits for Epochs 1, 3, 5 and 9 are affected by this issue. In order to account for these large inter-observation differences, not corrected by standard cross-normalization methods, the `crabcorr` model was implemented (Steiner et al. 2010), nevertheless, residual mismatches in spectral shape remained. Considering the need for a more flexible strategy, the photon index Γ was allowed to vary between *NICER* observations within the same epoch. However, despite providing a marked improvement to the spectral fit ($\Delta\chi^2 = 4322$ for 6 additional d.o.f.), this approach did not fully solve the issue. Thus, observations presenting very strong flux inconsistencies were removed from consideration in the respective

previously mentioned epochs, in order to reach a satisfactory quality of the analysis.

NICER observations identified by ObsIDs 3133010106, 4133010104, and 4133010261 captured periods of very intense source variability, and were hence removed from the respective Epochs 1, 5, and 9. Additionally observations 3558010601 and 4652010101 were also removed from consideration in Epochs 3 and 9 respectively, due to their high background levels compared to other *NICER* observations in the same epochs.

Additionally, from Figure 4.7 is also possible to notice some discrepancy between the intensity detected by *NICER* and by *NuSTAR* around $3-5$ keV. Similar issues have already been encountered in numerous recent studies (e.g., Tao et al. 2019; Nath et al. 2024; Steiner et al. 2024). There have been some indications that these slight inconsistencies in the low energy band may stem from *NuSTAR* calibration issues (Madsen et al. 2020; Chakraborty et al. 2021). In our case, these discrepancies were evaluated to not significantly affect our estimates, and hence treated as negligible in the overall spectral fitting process.

Black hole spin measurement joint fitting

Aiming to obtain an estimate of the black hole spin, the same five epochs and fitting strategy as for the interstellar absorption parameters estimation (i.e., Epochs 1, 4, 5, 6, and 9) were considered. Notably, considering observations spanning different spectral states of the source contributed to breaking the degeneracy between inner disk radius and BH spin, allowing for a simultaneous inference of the two parameters. Furthermore, joint fitting also enabled a more accurate estimate of state-independent parameters such as the inclination angle and iron abundance of the disk, the results of which are provided in Table 4.3, together with the measured BH spin values.

a_*	i (deg)	$A_{\rm Fe}$ (solar)	χ^2 / $d.o.f.$	$\chi^2_{\rm red}$
$0.9974\ ^{+0.0002}_{-0.0004}$	45.4 ± 0.1	4.28 ± 0.03	5020 / 3495	1.436

Table 4.3. M2 joint fitting results for the BH spin, disk inclination angle and iron abundance.

Individual epoch fitting

Each epoch of the outburst was then fitted individually, considering M2 and fixing the values for the $N_{\rm H}$, Fe, and O columns to those obtained from multi-epoch fitting (Table 4.2). Low energy features in the *NICER* data were considered individually for each epoch by multiplying one or two `edge` or `gabs` components to the standard M2, in order to provide the best possible treatment. Furthermore, owing the low flux levels in Epochs 10 and 11 leading to rather weak reflection features, the disk inclination angle and emissivity profile were frozen (respectively to $i = 40^{\circ}$ and $q = 3$) during spectral fits for these data groups. The resulting spectra for each epoch of the outburst are plotted in the following pages.

(a) Epoch 1

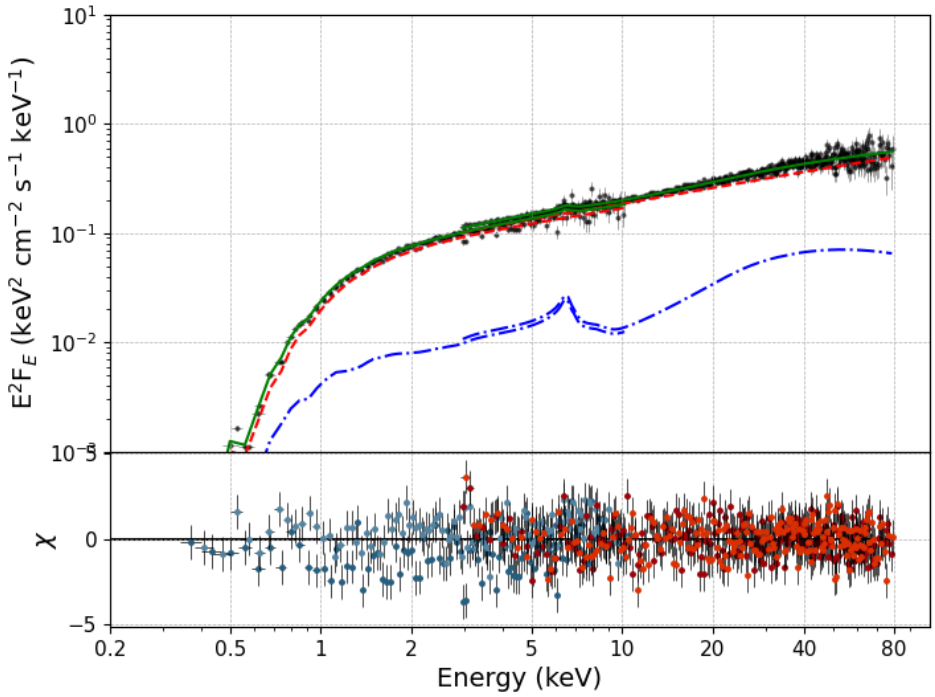

(b) Epoch 2

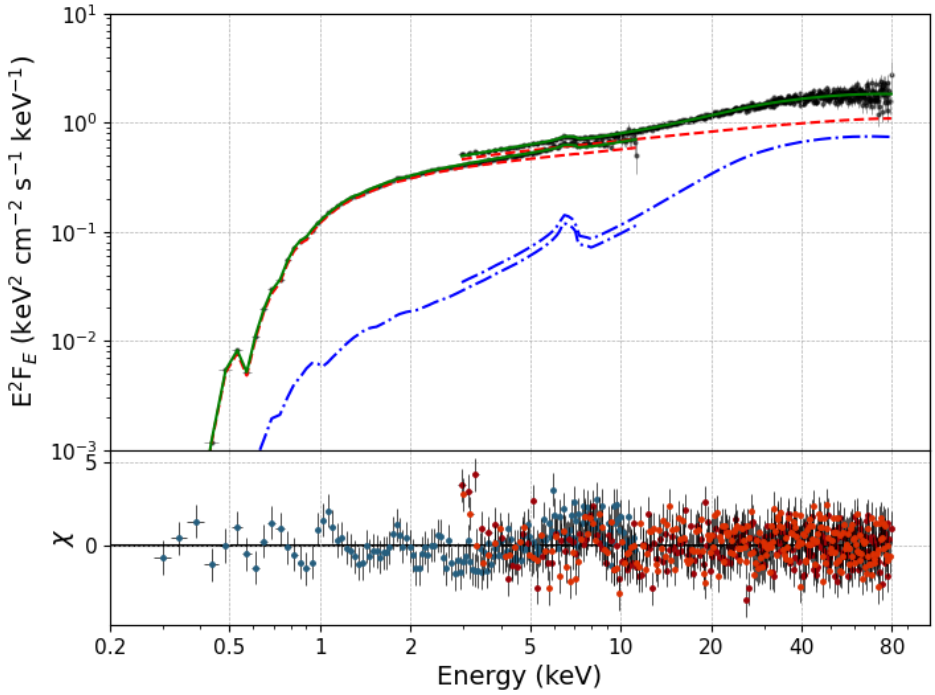

Figure 4.8. M2 best-fit spectrum for GX 339-4 in Epoch 1 (a) and Epoch 2 (b). The upper panels show *NuSTAR* and *NICER* data (black data points), the best-fit spectrum (green solid line), the continuum component (red dashed line), and the Comptonization component (blue dashed-dotted line). The lower panels indicate the residuals between *NICER* XTI observations (navy blue gradient) and *NuSTAR* FPMA (dark red) and FPMB (orange) observations, and the best-fit model (black solid line).

(a) Epoch 3

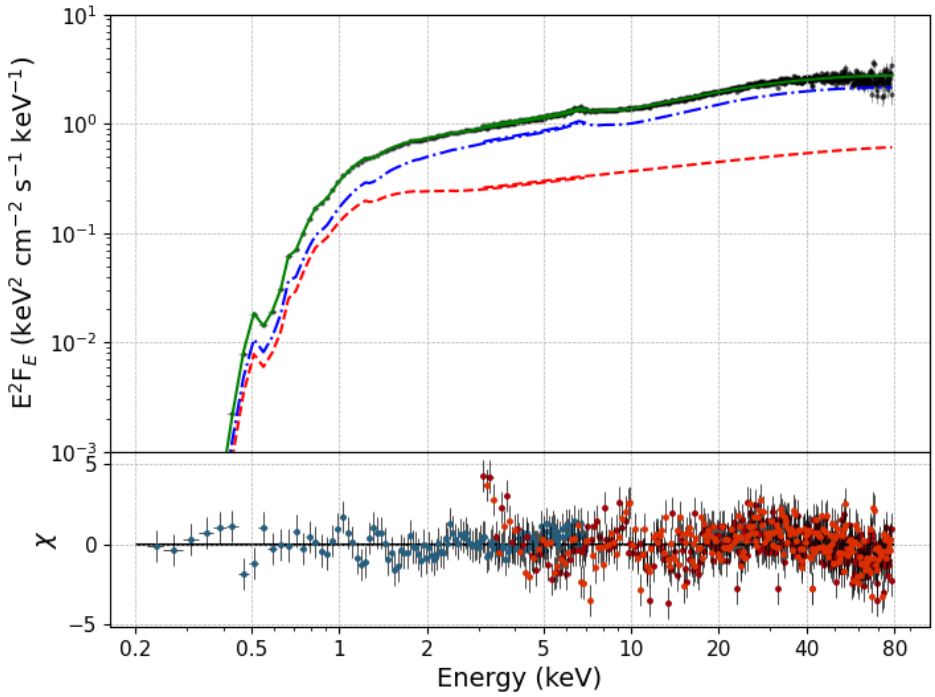

(b) Epoch 4

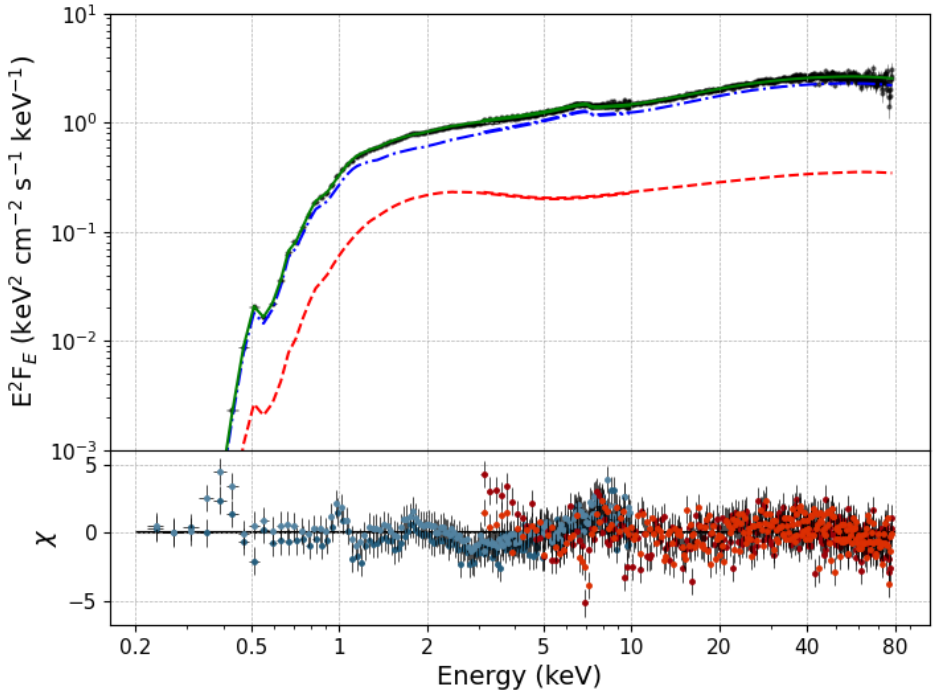

Figure 4.9. M2 best-fit spectrum for GX 339-4 in Epoch 3 (a) and Epoch 4 (b). The upper panels show *NuSTAR* and *NICER* data (black data points), the best-fit spectrum (green solid line), the continuum component (red dashed line), and the Comptonization component (blue dashed-dotted line). The lower panels indicate the residuals between *NICER* XTI observations (navy blue gradient) and *NuSTAR* FPMA (dark red) and FPMB (orange) observations, and the best-fit model (black solid line).

(a) Epoch 5

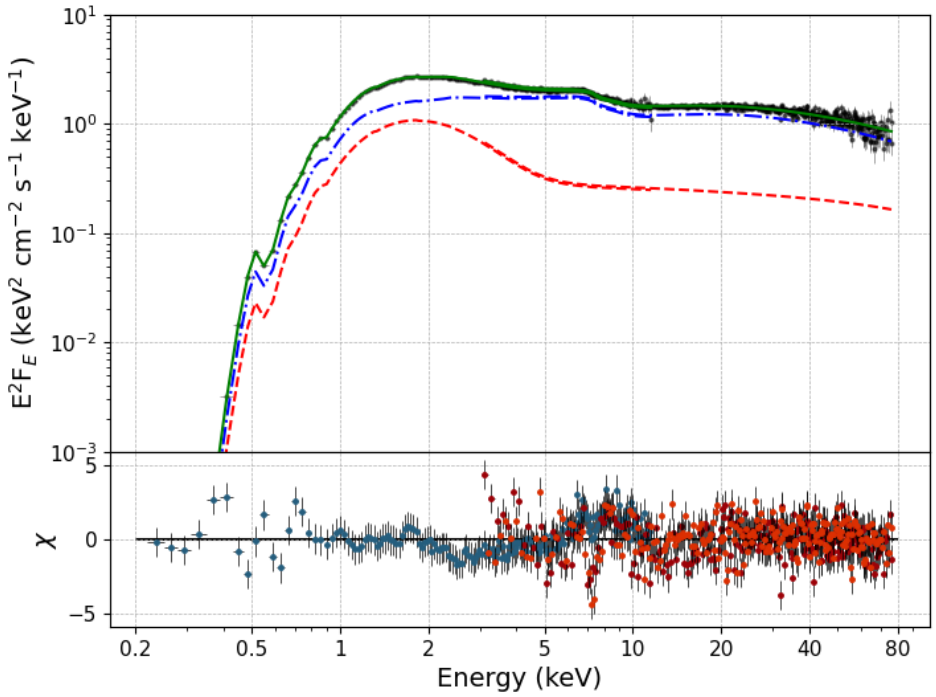

(b) Epoch 6

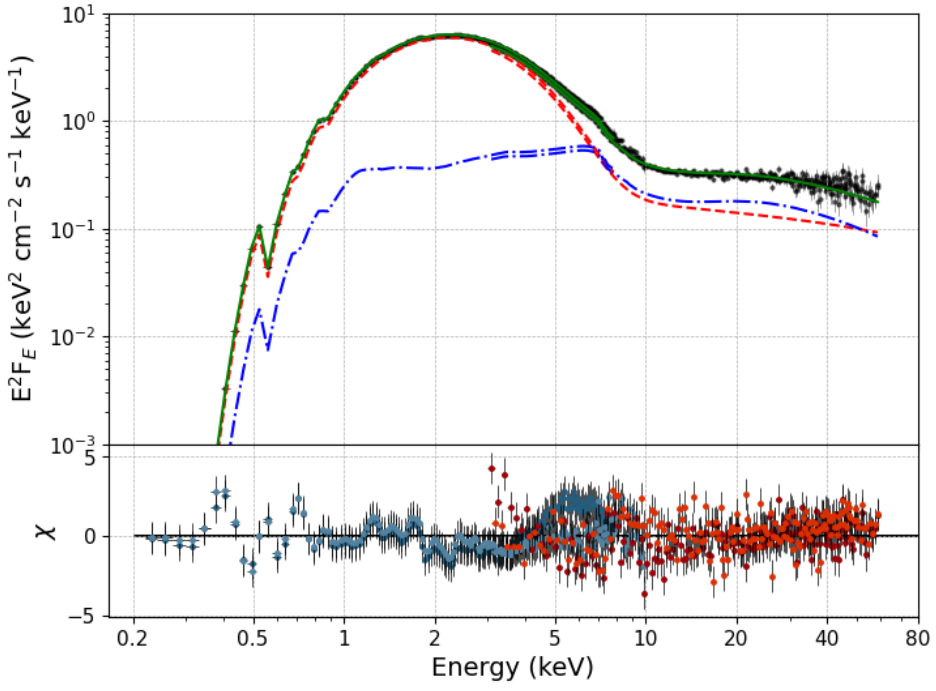

Figure 4.10. M2 best-fit spectrum for GX 339-4 in Epoch 5 (a) and Epoch 6 (b). The upper panels show *NuSTAR* and *NICER* data (black data points), the best-fit spectrum (green solid line), the continuum component (red dashed line), and the Comptonization component (blue dashed-dotted line). The lower panels indicate the residuals between *NICER* XTI observations (navy blue gradient) and *NuSTAR* FPMA (dark red) and FPMB (orange) observations, and the best-fit model (black solid line).

(a) Epoch 7

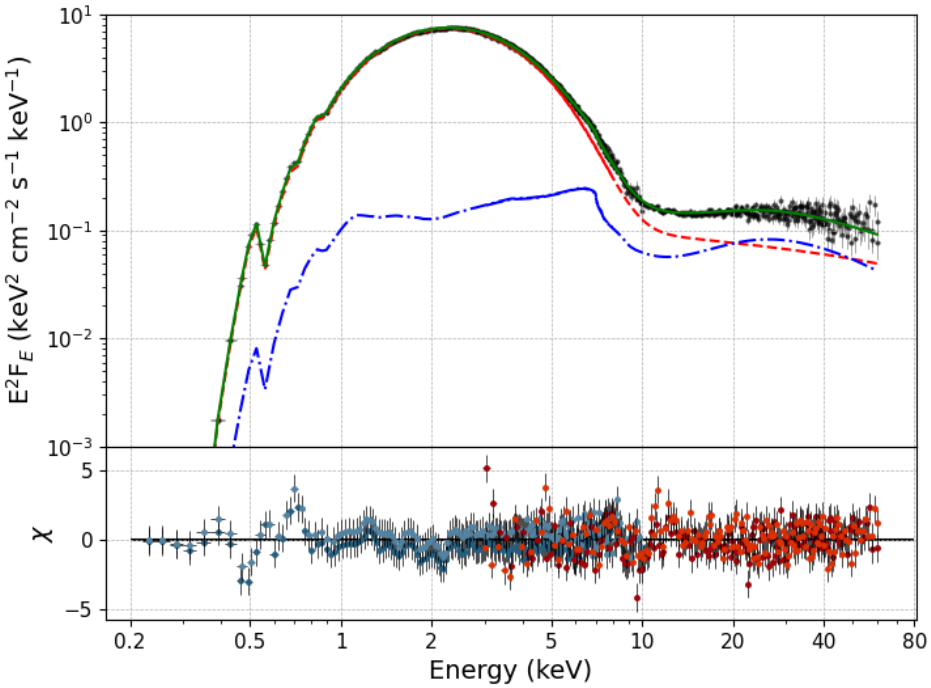

(b) Epoch 8

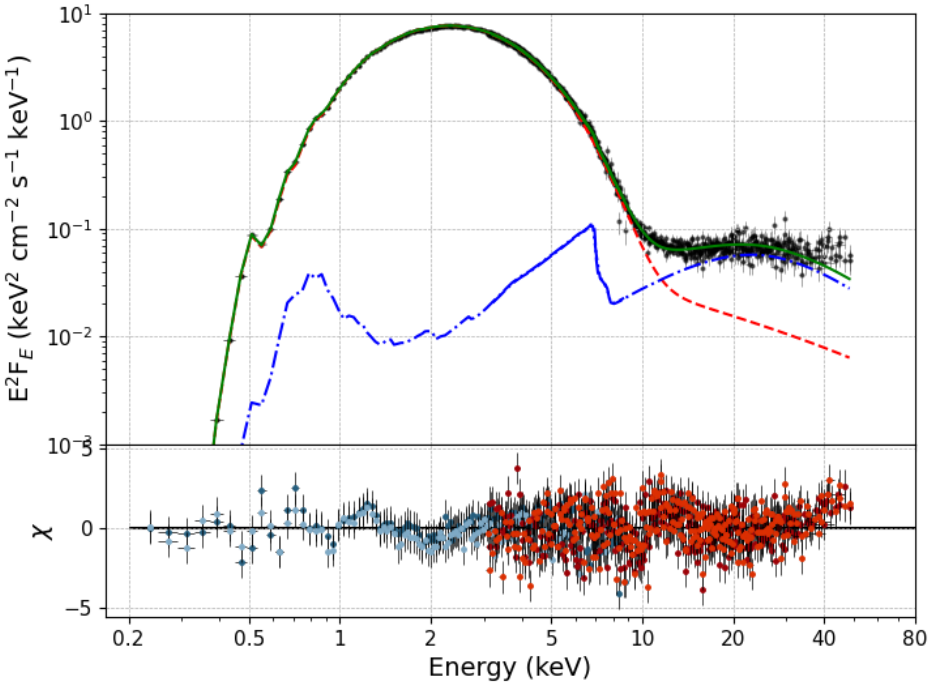

Figure 4.11. M2 best-fit spectrum for GX 339-4 in Epoch 7 (a) and Epoch 8 (b). The upper panels show *NuSTAR* and *NICER* data (black data points), the best-fit spectrum (green solid line), the continuum component (red dashed line), and the Comptonization component (blue dashed-dotted line). The lower panels indicate the residuals between *NICER* XTI observations (navy blue gradient) and *NuSTAR* FPMA (dark red) and FPMB (orange) observations, and the best-fit model (black solid line).

(a) Epoch 9

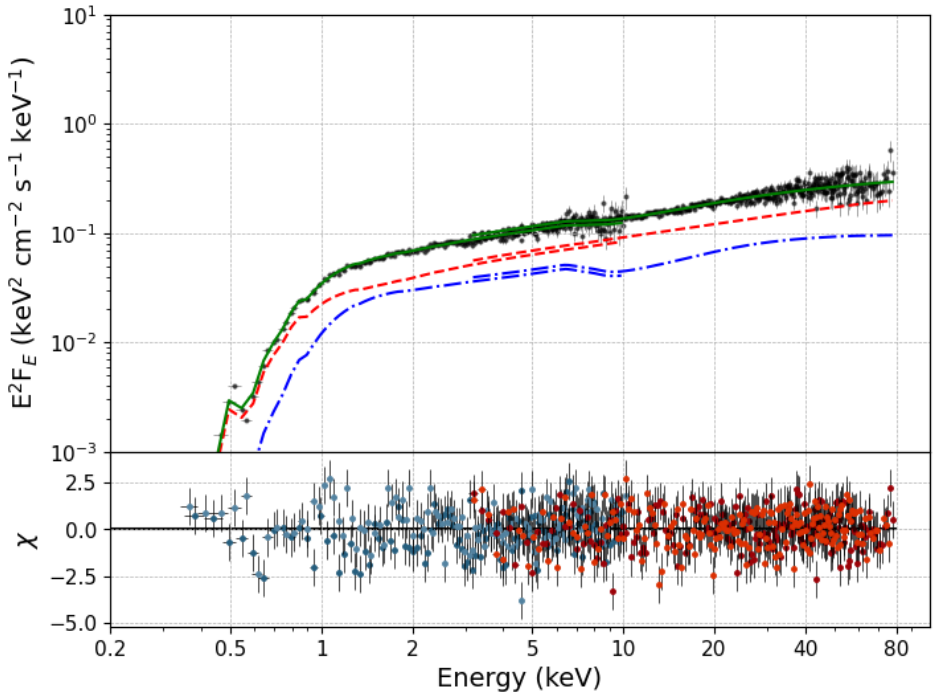

(b) Epoch 10

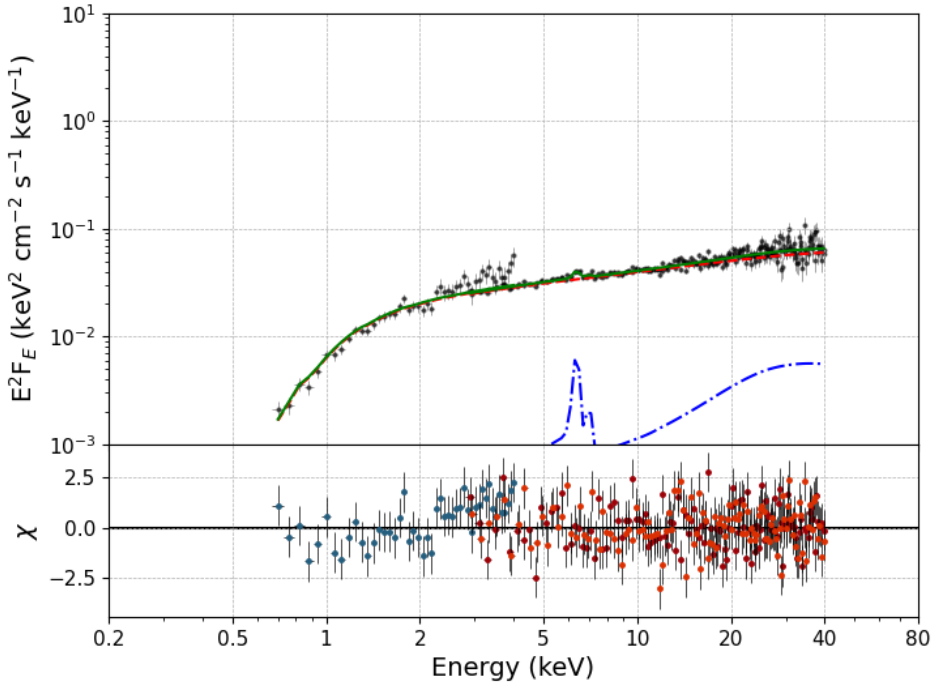

Figure 4.12. M2 best-fit spectrum for GX 339-4 in Epoch 9 (a) and Epoch 10 (b). The upper panels show *NuSTAR* and *NICER* data (black data points), the best-fit spectrum (green solid line), the continuum component (red dashed line), and the Comptonization component (blue dashed-dotted line). The lower panels indicate the residuals between *NICER* XTI observations (navy blue gradient) and *NuSTAR* FPMA (dark red) and FPMB (orange) observations, and the best-fit model (black solid line).

(a) Epoch 11

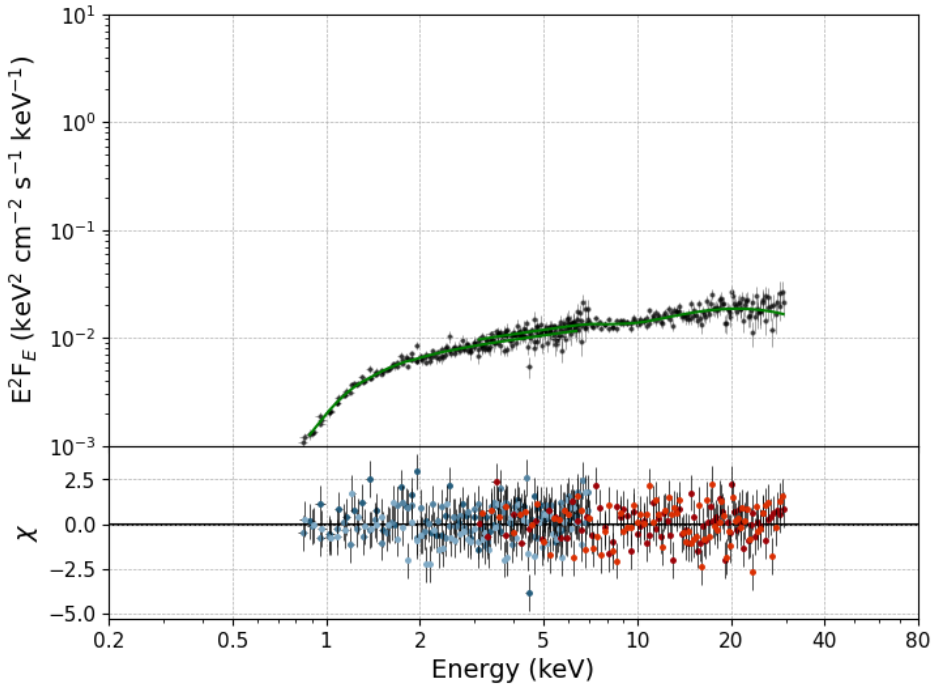

Figure 4.13. M2 best-fit spectrum for GX 339-4 in Epoch 11 (a). The upper panels show *NuSTAR* and *NICER* data (black data points), the best-fit spectrum (green solid line), the continuum component (red dashed line), and the Comptonization component (blue dashed-dotted line). The lower panels indicate the residuals between *NICER* XTI observations (navy blue gradient) and *NuSTAR* FPMA (dark red) and FPMB (orange) observations, and the best-fit model (black solid line).

M2 spectral fitting results for the most important model parameters are presented in Table 4.4 and Table 4.5. In order to estimate the flux emitted by the source, neglecting the effect of interstellar absorption, the `cflux` convolution model was employed in addition to M2. Notable trends between model parameters and the source luminosity and their implications will be further explored in the subsequent discussion section (4.3).

Epoch	$L_{\rm Edd}$ (%)	Γ	$f_{\rm sctr}$	kT_e (keV)	$T_{\rm in}$ (keV)	i (deg)
1	$1.335^{+0.006}_{-0.010}$	1.571±0.008	$0.05^{+0.66}_{-0.02}$	301^{p}_{-174}	$0.02^{+0.01}_{-0.02}$	41.0±3.0
2	$5.29^{+0.02}_{-0.08}$	$1.742^{+0.005}_{-0.006}$	$0.61^{+0.03}_{-0.02}$	143^{+115}_{-49}	$0.171^{+0.003}_{-0.004}$	$46.0^{+3.0}_{-2.0}$
3	$9.02^{+0.02}_{-0.09}$	$1.738^{+0.006}_{-0.003}$	0.52±0.01	400^{p}_{-29}	$0.336^{+0.013}_{-0.008}$	$42.7^{+0.7}_{-0.8}$
4	$9.97^{+0.01}_{-0.03}$	1.733±0.003	$0.563^{+0.008}_{-0.007}$	49^{+1}_{-2}	0.67±0.02	$36.0^{+1.0}_{-2.0}$
5	$12.98^{+0.06}_{-0.04}$	$2.111^{+0.005}_{-0.008}$	$0.228^{+0.014}_{-0.007}$	400^{p}_{-201}	$0.534^{+0.005}_{-0.006}$	$42.0^{+1.0}_{-2.0}$
6	14.83±0.04	$2.229^{+0.005}_{-0.012}$	$0.0429^{+0.0006}_{-0.0023}$	400^{p}_{-83}	0.772±0.002	33.0±1.0
7	$17.48^{+0.06}_{-0.08}$	2.23±0.02	0.018±0.001	400^{p}_{-187}	$0.811^{+0.001}_{-0.002}$	31.0±2.0
8	$17.6^{+0.10}_{-0.05}$	$2.75^{+0.03}_{-0.05}$	$0.0096^{+0.0012}_{-0.0007}$	400^{p}_{-178}	$0.8261^{+0.0010}_{-0.0009}$	41.0±1.0
9	$0.98^{+0.007}_{-0.006}$	$1.638^{+0.01}_{-0.011}$	$0.32^{+0.01}_{-0.02}$	319^{p}_{-191}	$0.187^{+0.007}_{-0.008}$	$44.0^{+9.0}_{-13.0}$
10	$0.49^{+0.13}_{-0.07}$	$1.70^{+0.02}_{-0.01}$	$0.07^{+0.07}_{-0.01}$	29^{+334}_{-10}	$0.07^{+0.01}_{-0.02}$	40.0^{f}
11	$0.078^{+0.002}_{-0.015}$	1.7±0.1	$0.07^{+0.07}_{-0.01}$	25^{+21}_{p}	$0.04^{+0.12}_{p}$	40.0^{f}

Table 4.4. M2 best-fit results for each Epoch. ^{p} and $_{p}$ flags indicate the parameter was pegged at the upper or lower bound during the fitting process, implying a lower or upper limit respectively, while ^{f} indicates the parameter was frozen during the fit.

Epoch	$R_{\rm in}$ (R_g)	q	$log\,\xi$	$log\,N$ (cm^{-3})	$A_{\rm Fe}$ (solar)	$\chi^2/d.o.f.$	$\chi^2_{\rm red}$
1	$4.1^{+0.7}_{-0.5}$	$10.0^{p}_{-2.0}$	$3.13^{+0.03}_{-0.05}$	$17.21^{+0.1}_{-0.09}$	$10.0^{p}_{-0.7}$	798/672	1.187
2	$3.5^{+0.4}_{-0.5}$	$5.0^{+1.2}_{-0.9}$	$1.7^{+0.06}_{-0.39}$	$15.0^{+0.08}_{p}$	$4.1^{+0.3}_{-0.2}$	817/648	1.261
3	4.0±0.2	$10.0^{p}_{-0.8}$	3.22±0.02	$16.0^{+0.2}_{-0.6}$	3.9±0.1	826/633	1.305
4	$1.7^{+0.2}_{-1.7}$	2.96±0.07	2.87±0.03	19.52±0.06	$4.9^{+0.7}_{-0.2}$	1149/847	1.357
5	$1.5^{+0.1}_{-0.2}$	3.8±0.1	2.87±0.02	$20.0^{p}_{-0.05}$	2.7±0.2	939/646	1.454
6	2.3±0.2	$3.46^{+0.11}_{-0.09}$	$2.63^{+0.04}_{-0.02}$	$19.7^{+0.1}_{-0.2}$	$5.0^{+0.1}_{-0.2}$	856/688	1.245
7	$1.6^{+0.8}_{-1.6}$	$3.3^{+0.2}_{-0.1}$	$2.88^{+0.05}_{-0.06}$	19.0±0.1	$9.0^{p}_{-2.0}$	723/653	1.108
8	1.0±1.0	$3.0^{+0.2}_{-0.1}$	$1.3^{+0.07}_{-0.1}$	$18.25^{+0.18}_{-0.09}$	$10.0^{p}_{-0.7}$	1224/866	1.413
9	$2.9^{+0.8}_{-0.6}$	$10.0^{p}_{-3.0}$	$3.6^{+0.06}_{-0.05}$	$20.0^{p}_{-0.4}$	$8.0^{p}_{-3.0}$	710/634	1.120
10	120^{p}_{-28}	3.0^{f}	$0.01^{+1.85}_{-0.01}$	$19.0^{+0.6}_{-1.5}$	$8.0^{p}_{-4.0}$	333/283	1.175
11	107^{p}_{-8}	3.0^{f}	$3.7^{+0.2}_{-0.6}$	$20.0^{p}_{-2.0}$	2.0±1.0	364/356	1.022

Table 4.5. M2 best-fit results for each Epoch. ^{p} and $_{p}$ flags indicate the parameter was pegged at the upper or lower bound during the fitting process, implying a lower or upper limit respectively, while ^{f} indicates the parameter was frozen during the fit.

4.3 Discussion

Single-epoch spectral fitting for M2 provided statistically acceptable results across the different stages of the outburst, with reduced χ^2 values consistently close to unity, indicating a reliable agreement between the model and the observed spectra. The analysis followed the spectral evolution of the source from the hard state through the intermediate state and into the soft state, enabling us to probe and characterize its evolving spectral behaviour.

Spectral states

Combining the evolution of the shape of the broadband energy spectrum of the source across all epochs, and the trend of Γ and $T_{\rm in}$, it is possible to identify the different spectral states through which GX 339-4 transitioned during the 2021 outburst. In particular, the source can be classified as being in the low hard state for Epochs 1 to 4 and 9 to 11, owing to photon index values below 1.8, as shown in Figure 4.14. Additionally, figure 4.15, describes how the rising inner disk temperature in these epochs is correlated to the increase in Eddington ratio and hence to the mass accretion rate, with Epochs 2, 3, and 4 being up to two orders of magnitude brighter than their lower flux counterparts (bright low hard state).

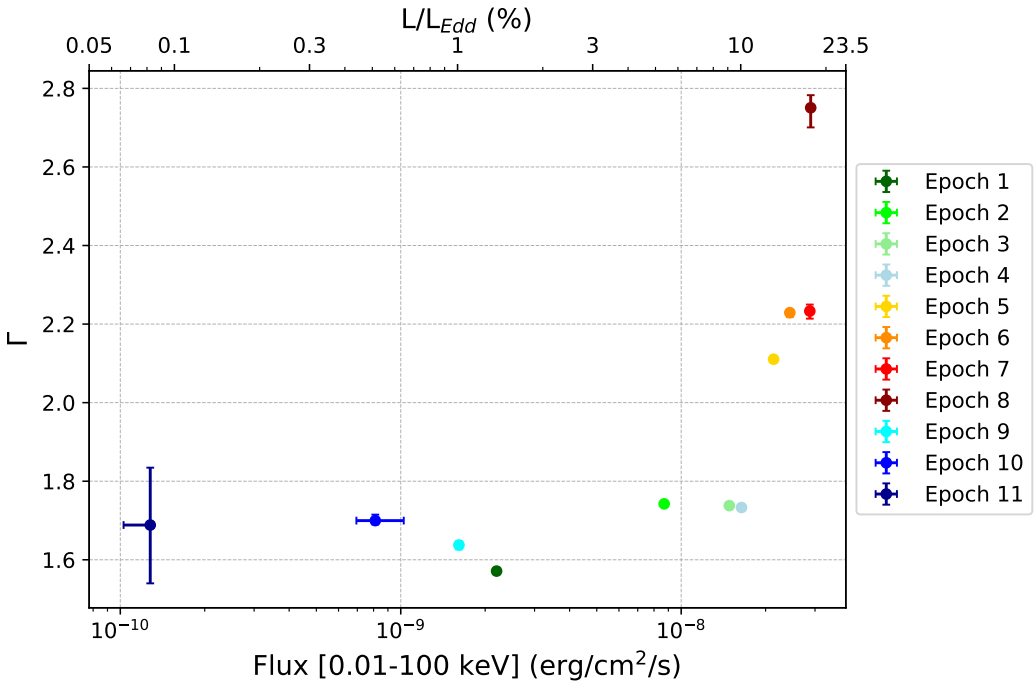

Figure 4.14. M2 best-fit results for the evolution of the photon index Γ across the 11 epochs, plotted as a function of the unabsorbed flux in the $0.01-100$ keV energy band, and of the Eddington ratio.

As the source transitioned through intermediate states, both the photon index and the disk contribution increased with respect to the low hard state, indicating the progressive softening of the spectrum to $\Gamma \approx 2.2$ as the disk became hotter. This is the scenario that best describes Epochs 5, 6, and 7: in the former the contribution to the total flux is rather balanced between disk thermal emission and coronal Comptonization, subsequently the inner disk temperature increases from 0.5 to reaching 0.8 keV in the latter two epochs, with the disk completely dominating the spectrum over coronal emission.

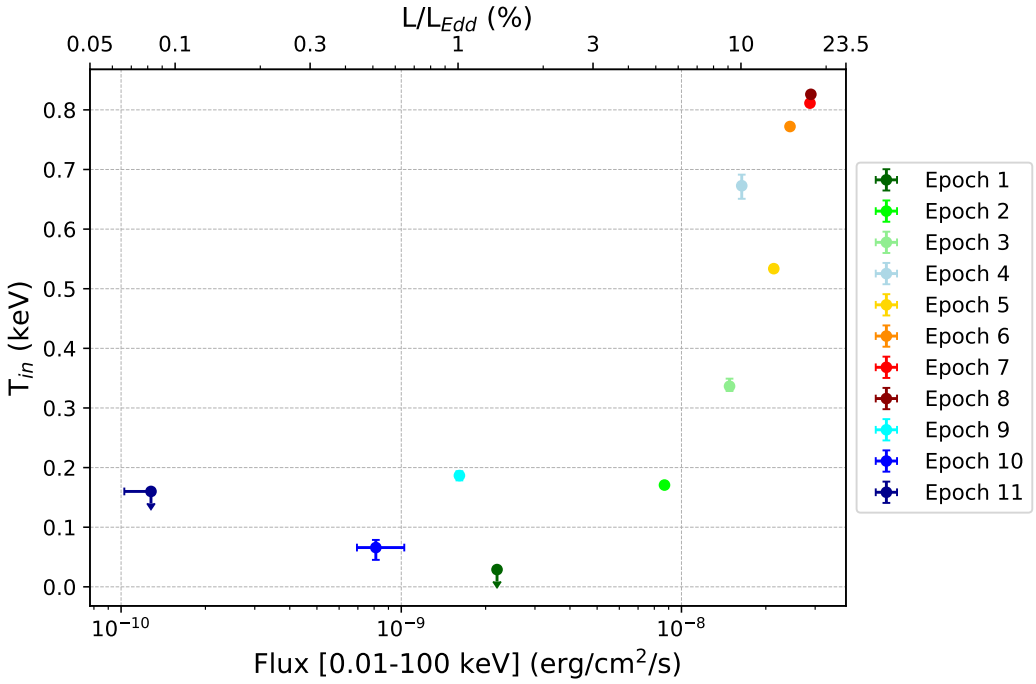

Figure 4.15. M2 best-fit results for the evolution of the inner accretion disk temperature $T_{\rm in}$ across the 11 epochs, plotted as a function of the unabsorbed flux in the $0.01 - 100$ keV energy band, and of the Eddington ratio.

The completion of the hard-to-soft state transition is then testified by Epoch 8, when the source reaches the high soft state ($\Gamma = 2.75^{+0.03}_{-0.05}$) with Eddington ratio $L/L_{\rm Edd} = (17.6 \pm 0.1)\%$, before the final decaying phase with the aforementioned low hard states of Epochs 9 to 11.

Inner disk radius

The inner accretion disk radius is a crucial parameter to understand the accretion process and its geometry. In this context, Figure 4.16 displays our findings regarding the evolution of $R_{\rm in}$, suggesting modest disk truncation in the bright hard state, and the inner disk being located close to the innermost stable circular orbit radius

in the softer states.

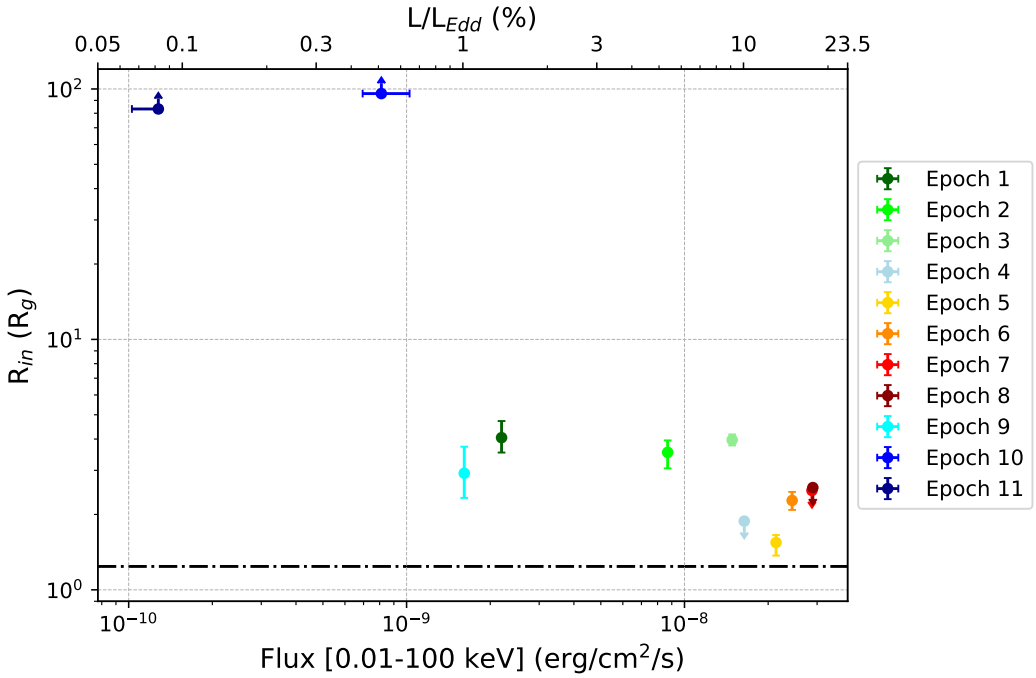

Figure 4.16. M2 best-fit results for the evolution of the inner accretion disk radius $R_{\rm in}$ across the 11 epochs, plotted as a function of the unabsorbed flux in the $0.01-100$ keV energy band, and of the Eddington ratio. The horizontal grey line represents the ISCO radius for a BH with spin $a_* = 0.998$.

More specifically, for luminosities between 1 and 10% the Eddington limit, corresponding to the low hard state Epochs 1, 2, 3, and 9, the accretion disk remains modestly truncated around 4 R_g. Wang et al. (2018; 2020) investigated GX 339-4 in the same luminosity range finding modest truncation in this range ($3\,R_g \lesssim R_{\rm in} \lesssim 15\,R_g$), and larger truncation ($R_{\rm in} > 49\,R_g$) for luminosities below 0.5% $L_{\rm Edd}$, in agreement with the lower limits of $\sim 100\ R_g$ found in our study for Epochs 10 and 11.

As the luminosity increases above 10% $L_{\rm Edd}$ with the state transition, we find that the disk progressively moves closer to BH. In particular, our results are consistent with a scenario where the accretion disk's inner edge extends up to the ISCO radius in the soft state, with Epochs 4 to 8 all showing values of $R_{\rm in}$ below 3 R_g. Considering that an *Insight-HXMT* analysis of GX 339-4 during this same outburst by Liu et al. (2023) found similar evidence against strong disk truncation in this luminosity range, our results provide additional and mission-independent supporting evidence to the hypothesis that the disk is already close to the ISCO from the very early stages of the hard-to-soft transition, when the source is in the bright hard state.

Aiming to further test this hypothesis and to provide a comprehensive picture of past studies of black hole X-ray binary sources, we compared our results to data from Liu et al. (2023) in Figure 4.17. Measurements for GX 339-4 are reported in red for this thesis and in black and grey for other studies of the source (Miller et al. 2006; Reis et al. 2008; Tomsick et al. 2008; 2009; Shidatsu et al. 2011; Kolehmainen et al. 2014; Garcia et al. 2015; Plant et al. 2015; Basak & Zdziarski 2016; Wang-Ji et al. 2018; Liu et al. 2023). In particular, results from timing mode data of *XMM-Newton* in grey show disagreement with measurements by other instruments, finding a strongly truncated disk even at large fractions of the Eddington limit. However, this may be due to complex pile-up effects introducing systematics in the measurements (see the discussion by Wang-Ji et al. 2018).

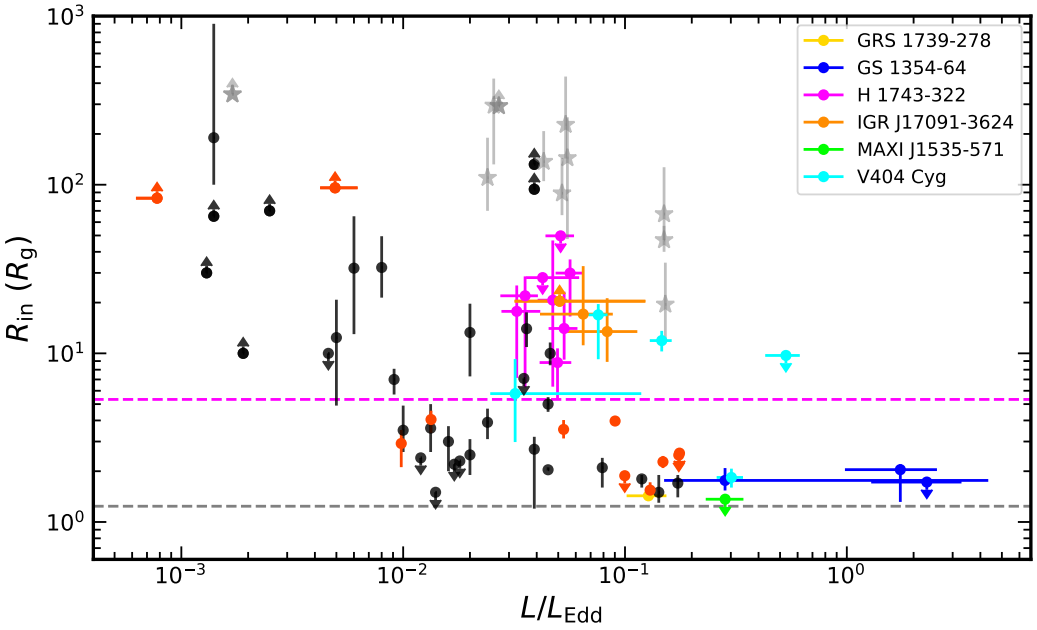

Figure 4.17. Evolution of the inner accretion disk radius as a function of the Eddington-scaled luminosity. Red data points represent results of this work, while data in black and grey are from previous studies of GX 339-4 (Miller et al. 2006; Reis et al. 2008; Tomsick et al. 2008; 2009; Shidatsu et al. 2011; Kolehmainen et al. 2014; Garcia et al. 2015; Plant et al. 2015; Basak & Zdziarski 2016; Wang-Ji et al. 2018; Liu et al. 2023), with measurements marked by grey stars referring to *XMM-Newton* observations. Additional colour-coded data from six other sources (Liu et al. 2023) is reported. The grey and magenta horizontal dashed lines represent the ISCO radius for a BH with spin 0.998 and 0.2 (corresponding to the spin estimated for H 1743-332) respectively.

Furthermore, apart from the clear trend noticeable in GX 339-4 measurements, data from six other sources yields additional evidence that the inner disk can indeed reach the ISCO in the bright hard state, with almost all measurements being consistent with $R_{\rm in}$ being truncated at radii smaller than 2 $R_{\rm ISCO}$ (Liu et al. 2023).

Corona

The results of this study probe the geometry and evolution of the corona during the outburst. Specifically, the variability in the high-energy cutoff and scattered fraction offers valuable insights about the coronal size, height, and physical properties. Being the high-energy cutoff in the X-ray spectrum directly related to the electron temperature in the corona, it provides information about the nature of the electron distribution, while the scattered fraction reflects the strength of the Comptonization component, which weakens as the disk emission dominates in softer states.

During the hard state, the electron distribution in the corona is generally thought to be thermal, characterized by a Maxwellian distribution (e.g., Zdziarski et al. 1996), allowing for more accurate constraints of the limited electron temperature via the high-energy cutoff in the spectrum. As the source transitions to the intermediate and soft states, coronal emission gets weaker and more efficient cooling of thermal electrons would be observed as lower cutoff energies in the spectrum. Conversely, our findings reported in Figure 4.18 suggest an increase of the coronal electron temperature with the source brightening. This tendency of the spectrum to extend to higher energies, might be explained by the distribution of coronal electrons developing a significant non-thermal component. Non-thermal coronal models have been proposed to explain such behaviour, where a fraction of the electron population possesses a power law distribution, likely linked to magnetic reconnection events in the corona (e.g., Liu et al. 2024).

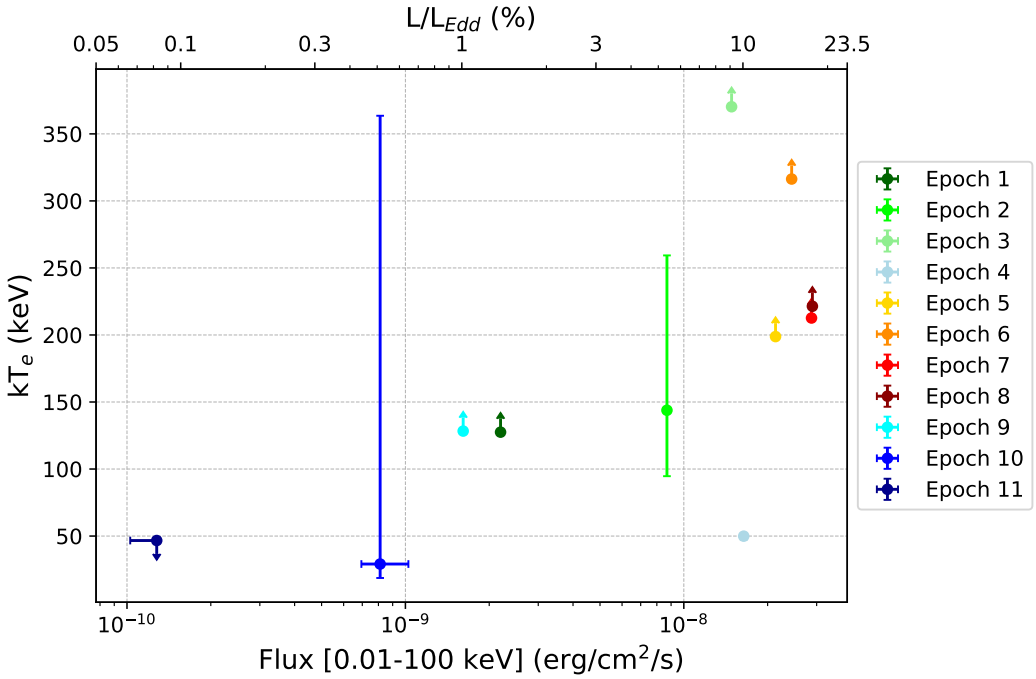

Figure 4.18. M2 best-fit results for the evolution of the coronal electron temperature kT_e across the 11 epochs, plotted as a function of the unabsorbed flux in the $0.01 - 100$ keV energy band, and of the Eddington ratio.

For the scattered fraction, a decreasing trend is generally expected, consistent with the weakening of coronal features and the increasing dominance of the disk's thermal emission during the spectral evolution. The declining trend followed by our results and displayed in Figure 4.19, may be interpreted as an initially extended corona progressively reducing in size, hence resulting in less scatterings of seed disk photons. Similar results were found in a recent study by Fan et al. (2024).

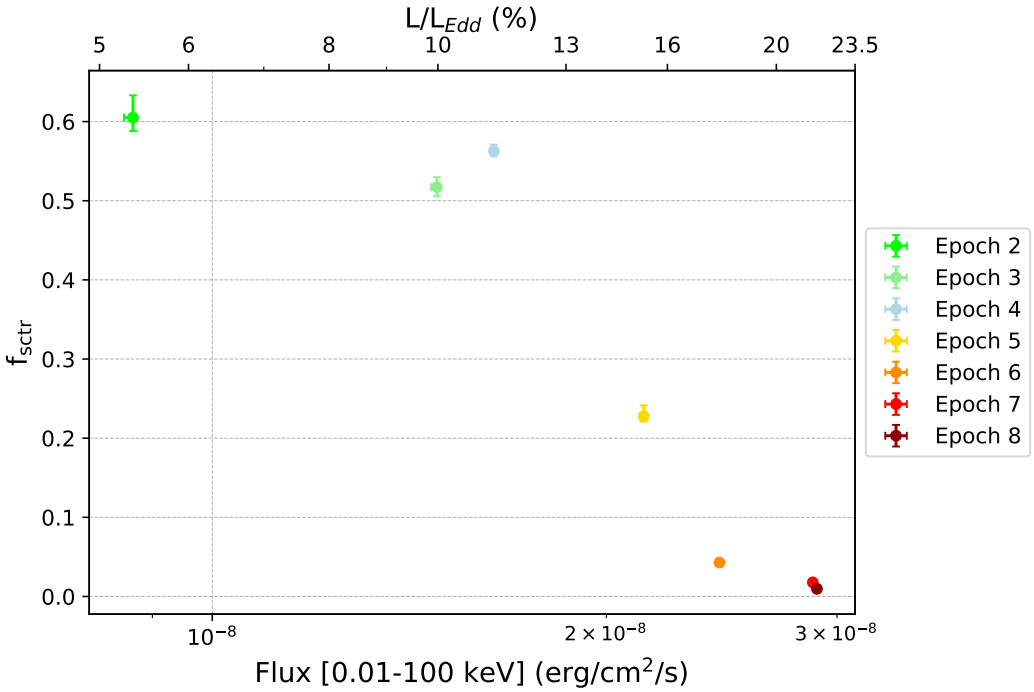

Figure 4.19. M2 best-fit results for the evolution of the scattered fraction $f_{\rm sctr}$ across 7 of the 11 epochs, plotted as a function of the unabsorbed flux in the $0.01 - 100$ keV energy band, and of the Eddington ratio.

However, we also observe low values of the scattered fraction in lower flux observations for Epochs 1, 9, 10, and 11, which were excluded from plotting in Figure 4.19 for visual purposes, but can be found in Table 4.4. These could result from a degeneracy between the reflection and continuum components, arising because the reflection features can mimic parts of the coronal emission, especially when the reflection fraction is high, or the continuum is faint.

Black hole spin

As anticipated in Section 4.2, joint fitting several epochs of the outburst has allowed for an estimation of the BH spin parameter for GX 339-4, finding $a_* = 0.9974^{+0.0002}_{-0.0004}$. Similar near-maximal spin values are in good agreement with those reported in previous reflection spectroscopy measurements, for instance Ludlam et al. 2015 found a lower limit of 0.97, and Parker et al. 2016 measured a_* to be $0.95^{+0.02}_{-0.08}$. Additionally, a recent study by Shyam et al. 2024 estimated $a_* \sim 0.99$, providing further support to the hypothesis that GX 339-4 harbours a rapidly spinning black hole.

However, despite the satisfactory agreement with past result and good statistical significance, the estimation of the BH spin strongly relies on the assumptions made

about the coronal geometry, which might introduce systematics in the measurement. Testing alternative coronal geometries through various emissivity configurations, is beneficial to assess the influence of model assumptions on the inferred spin value. Exploring these variations can improve the reliability of spin constraints obtained from reflection spectroscopy and reduce potential biases linked to disk illumination asymmetries and coronal structure, and represents a key focus for future research.

Inclination angle and iron abundance

Besides the estimation of the black hole spin, jointly fitting epochs from different spectral states provided a powerful tool to obtain more credible and accurate measurements of parameters that are expected to stay constant between observations. Furthermore, in our case the estimates of the accretion disk inclination angle and iron abundance obtained by jointly fitting Epochs 1, 4, 5, 6, and 9, provided an additional comparison to assess the accuracy of individual epoch fitting results, shown in Figures 4.20 and 4.21.

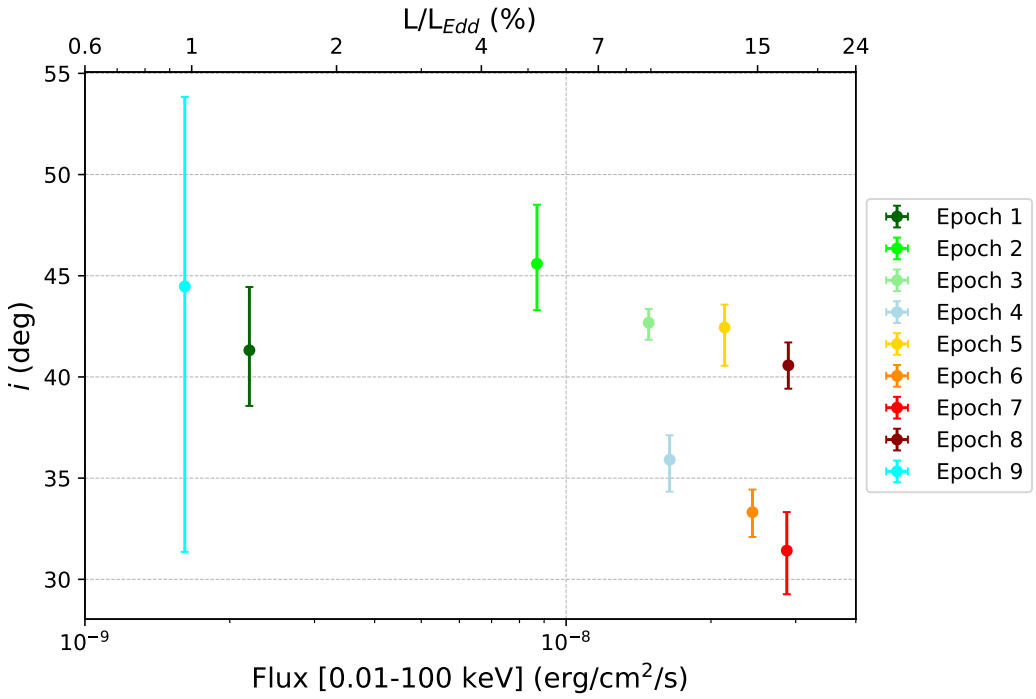

Figure 4.20. M2 best-fit results for the evolution of the inclination angle of the accretion disk across the first 9 epochs, plotted as a function of the unabsorbed flux in the $0.01 - 100$ keV energy band, and of the Eddington ratio. The inclination angle for Epochs 10 and 11 was frozen to 40° to best constrain other model parameters in these very low flux states.

In general, the constraints for i obtained from single-epoch fitting show consistency with a value between 30° and 50°, with the majority of the estimates clustering around 40° to 45°, in good agreement with the value of $45.4° \pm 0.1°$, obtained by jointly fitting several epochs. Additionally, our results are consistent with infrared studies of the binary inclination angle $37° < i_{\rm binary} < 78°$ (Zdziarski et al. 2019). It is important to note, however, that relativistic reflection methods only enable probing the inner regions of the accretion disk, the inclination of which may not coincide with the binary orbital inclination, as a warped disk structure might be present (e.g., Pringle 1996).

Regarding $A_{\rm Fe}$, the majority of results from fitting individual epochs show partial agreement with the joint fitting estimate of 4.28 ± 0.03. Notably, all measurements indicate significantly super-solar values, which deviate from typical expectations for GX 339-4. Since the source is a low mass X-ray binary, such elevated iron abundances are somewhat unexpected, as the donor star is likely a low-mass, evolved star, generally not associated with enhanced metallicity.

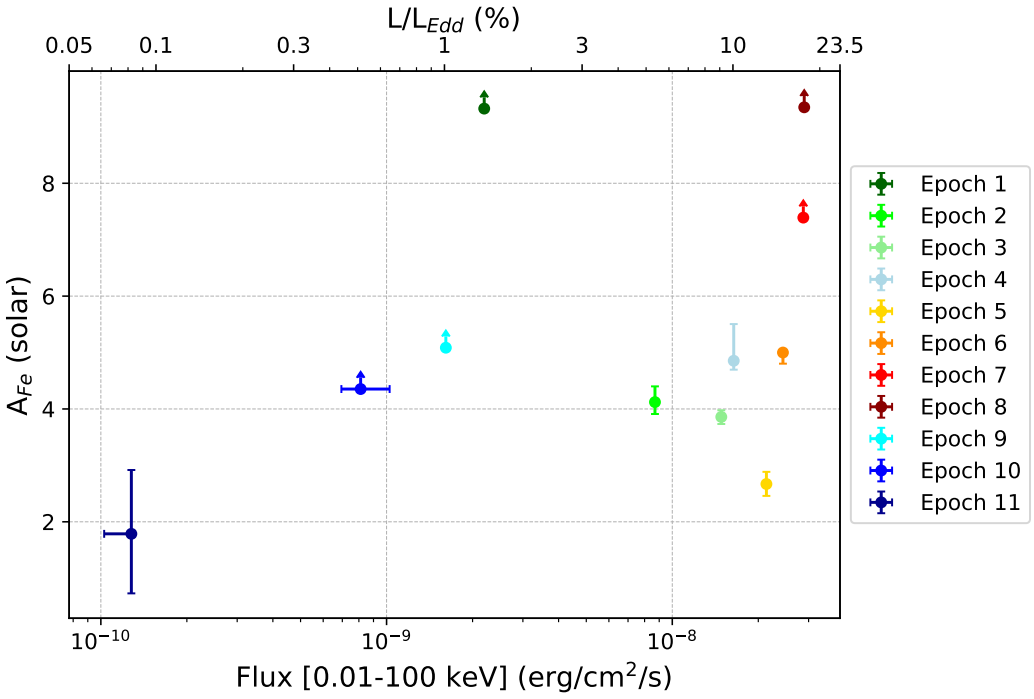

Figure 4.21. M2 best-fit results for the evolution of the iron abundance of the accretion disk $A_{\rm Fe}$ across the 11 epochs, plotted as a function of the unabsorbed flux in the $0.01 - 100$ keV energy band, and of the Eddington ratio.

However, super-solar iron abundances are a commonly reported outcome in X-ray reflection spectroscopy studies of accreting BHs, and are not unique to GX 339-4 (e.g., Parker et al. 2015; Walton et al. 2017). García et al. 2018 argue that this issue may be attributed to shortcomings in current reflection models, particularly at high disk densities. These model inaccuracies may either be due to unexplored physical mechanism in the disk contributing to the spectral signature or to limitations in current atomic data used for modelling. However, the presence of high iron abundances remains an open question in the field, emphasizing the need for improved theoretical models and more precise atomic data.

Chapter 5

Conclusions and Future Prospects

In this thesis, I investigated the evolution of the accretion geometry of the black hole X-ray binary GX 339–4 during the outburst it underwent in 2021. Making use of 13 observations from *NuSTAR* and 24 quasi-simultaneous observations from *NICER*, grouped in 11 multi-mission epochs, I was able to probe the variability of the source throughout the entirety of the outburst and especially track the hard-to-soft state transition. Leveraging the broadband X-ray coverage obtained by combining *NuSTAR* and *NICER* data, I employed the state-of-the-art relativistic reflection spectroscopy model `relxill` to constrain spectral features originating from the reprocessing of high energy photons from the corona by the accretion disk atmosphere. The full model additionally comprised a multi-temperature blackbody accretion disk component, and a self-consistent treatment of the inverse Compton scattering of seed disk photons in the corona, aiming at a photon-conserving and reflection Comptonization-inclusive treatment.

Implementing both single and multi-epoch spectral fitting, the source was found to fully transition to a soft state, completing the characteristic "q-shaped" path in the hardness-intensity diagram. The overall quality of the fits strengthens the confidence in the physical reliability of the parameters derived from this model, and in the trends observed in the evolution of the spectral components. Results of this investigation point to a scenario in which the inner edge of the accretion disk is modestly truncated in the bright hard state and during the entire state transition ($R_{\rm in} \lesssim 2R_{\rm ISCO}$), in agreement with recent evidence for this and other BHXRB sources (e.g., Liu et al. 2023). Subsequently, the disk progressively moves closer to the BH and extends up to the innermost stable circular orbit radius in the soft state. Furthermore, our results are consistent with an extended corona which is both steadily decreasing in size and characterized by a growing non-thermal electron distribution throughout the state transition. Additionally, we find the black hole spin to be $a_* = 0.9974^{+0.0002}_{-0.0004}$, in good agreement with estimates of a near maximally-spinning BH from previous studies (Parker et al. 2016; Liu et al. 2023).

Key goals for future work are to extend the BH spin estimation by exploring alternative coronal geometries, as different configurations could influence the strength and shape of reflection features and emissivity profiles, and to additionally implement a relativistic disk model to fully combine reflection spectroscopy, and the complementary method for spin measurements: continuum-fitting.

By refining the spectral modelling, exploring a broader range of physical scenarios, and employing self-consistent methods for spin estimation, future work will aim to achieve a deeper understanding of the accretion dynamics and the fundamental properties of GX 339–4, further contributing to the study of accreting black holes and their extreme environments.

Appendix A

Observations Tables

Epoch	Telescope / Instrument	Observation ID	Start Time	Exposure [s]
Epoch 1	NuSTAR / FPM	90702303001	2021-01-23 21:46:09	25071
	NICER / XTI	3133010104	2021-01-23 17:26:25	496
	NICER / XTI	3133010105	2021-01-23 23:39:07	3968
	NICER / XTI	3133010106	2021-01-25 00:27:31	2454
Epoch 2	NuSTAR / FPM	90702303003	2021-02-05 23:56:09	21926
	NICER / XTI	3133010116	2021-02-05 04:51:20	1086
Epoch 3	NuSTAR / FPM	90702303005	2021-02-20 10:06:09	20948
	NICER / XTI	3558010501	2021-02-20 03:52:17	1541
	NICER / XTI	3558010601	2021-02-21 03:09:50	2282
Epoch 4	NuSTAR / FPM	90702303007	2021-03-07 23:46:09	23416
	NICER / XTI	3558010902	2021-03-07 04:11:11	4532
	NICER / XTI	3558010903	2021-03-08 00:20:20	10998
Epoch 5	NuSTAR / FPM	90702303009	2021-03-26 12:06:09	15788
	NICER / XTI	4133010103	2021-03-26 03:22:39	6111
	NICER / XTI	4133010104	2021-03-27 01:04:53	8709
Epoch 6	NuSTAR / FPM	90702303011	2021-04-01 19:21:09	14753
	NICER / XTI	4133010109	2021-04-01 00:21:20	16128
	NICER / XTI	4133010110	2021-04-02 01:08:40	12205
Epoch 7	NuSTAR / FPM	90702303013	2021-04-23 19:41:09	20143
	NICER / XTI	4133010130	2021-04-23 01:04:32	3097
	NICER / XTI	4133010131	2021-04-24 01:55:40	3442
Epoch 8	NuSTAR / FPM	80601302002	2021-05-04 23:01:09	13590
	NuSTAR / FPM	80601302004	2021-05-05 10:06:09	4058
	NuSTAR / FPM	80601302006	2021-05-05 14:56:09	2401
	NICER / XTI	4133010141	2021-05-04 12:33:38	840
	NICER / XTI	4133010142	2021-05-05 21:07:46	320
Epoch 9	NuSTAR / FPM	80702316002	2021-10-10 02:06:09	21326
	NICER / XTI	4652010101	2021-10-10 02:16:35	6257
	NICER / XTI	4590010201	2021-10-10 17:47:20	1955
	NICER / XTI	4133010260	2021-10-10 20:52:40	857
	NICER / XTI	4133010261	2021-10-11 01:40:20	2636
Epoch 10	NuSTAR / FPM	80702316004	2021-10-20 02:01:09	21341
	NICER / XTI	4133010267	2021-10-20 22:44:03	189
Epoch 11	NuSTAR / FPM	80702316005	2021-11-02 08:26:09	17821
	NICER / XTI	4133010279	2021-11-02 01:40:17	45
	NICER / XTI	4652010501	2021-11-02 17:08:58	99
	NICER / XTI	4652010502	2021-11-03 00:53:35	349

Table A.1. Selected observations of GX 339-4 during the 2021 outburst.

Epoch	Telescope / Instrument	Date	Spectral bandpass
Epoch 1	NuSTAR / FPM	2021-01-23	3.0 – 79.0 keV
	NICER / XTI	2021-01-23	0.4 – 10.0 keV
	NICER / XTI	2021-01-23	0.4 – 10.0 keV
	NICER / XTI	2021-01-23	0.4 – 10.0 keV
Epoch 2	NuSTAR / FPM	2021-02-05	3.0 – 79.0 keV
	NICER / XTI	2021-02-05	0.3 – 11.2 keV
Epoch 3	NuSTAR / FPM	2021-02-20	3.0 – 79.0 keV
	NICER / XTI	2021-02-20	0.2 – 7.0 keV
	NICER / XTI	2021-02-20	0.2 – 7.0 keV
Epoch 4	NuSTAR / FPM	2021-03-07	3.0 – 79.0 keV
	NICER / XTI	2021-03-07	0.2 – 10.0 keV
	NICER / XTI	2021-03-07	0.2 – 10.0 keV
Epoch 5	NuSTAR / FPM	2021-03-26	3.0 – 79.0 keV
	NICER / XTI	2021-03-26	0.2 – 11.5 keV
	NICER / XTI	2021-03-26	0.2 – 11.5 keV
Epoch 6	NuSTAR / FPM	2021-04-01	3.0 – 60.0 keV
	NICER / XTI	2021-04-01	0.2 – 8.0 keV
	NICER / XTI	2021-04-01	0.2 – 10.5 keV
Epoch 7	NuSTAR / FPM	2021-04-23	3.0 – 60.0 keV
	NICER / XTI	2021-04-23	0.2 – 8.2 keV
	NICER / XTI	2021-04-23	0.2 – 10.7 keV
Epoch 8	NuSTAR / FPM	2021-05-05	3.0 – 50.0 keV
	NuSTAR / FPM	2021-05-05	3.0 – 50.0 keV
	NuSTAR / FPM	2021-05-05	3.0 – 50.0 keV
	NICER / XTI	2021-05-05	0.2 – 10.0 keV
	NICER / XTI	2021-05-05	0.2 – 9.2 keV
Epoch 9	NuSTAR / FPM	2021-10-10	3.0 – 79.0 keV
	NICER / XTI	2021-10-10	0.3 – 10.3 keV
	NICER / XTI	2021-10-10	0.3 – 10.3 keV
	NICER / XTI	2021-10-10	0.3 – 10.3 keV
	NICER / XTI	2021-10-10	0.3 – 10.3 keV
Epoch 10	NuSTAR / FPM	2021-10-20	3.0 – 40.0 keV
	NICER / XTI	2021-10-20	0.7 – 4.0 keV
Epoch 11	NuSTAR / FPM	2021-11-02	3.0 – 30.0 keV
	NICER / XTI	2021-11-02	0.8 – 7.0 keV
	NICER / XTI	2021-11-02	0.8 – 7.0 keV
	NICER / XTI	2021-11-02	0.8 – 7.0 keV

Table A.2. Overview of the energy channels noticed for each observation with observation dates.

Bibliography

Abbott, B. P. et al. (Feb. 2016). "Observation of Gravitational Waves from a Binary Black Hole Merger". In: Phys. Rev. Lett. 116.6, 061102, p. 061102. DOI: 10.1103/PhysRevLett.116.061102. arXiv: 1602.03837 [gr-qc].

Abbott, R. et al. (Sept. 2020). "GW190521: A Binary Black Hole Merger with a Total Mass of M⊙". In: Phys. Rev. Lett. 125.10, 101102, p. 101102. DOI: 10.1103/PhysRevLett.125.101102. arXiv: 2009.01075 [gr-qc].

Adegoke, Oluwashina K. et al. (Dec. 2024). "Characterizing the Broadband Reflection Spectrum of MAXI J1803-298 during Its 2021 Outburst with NuSTAR and NICER". In: ApJ 977.1, 26, p. 26. DOI: 10.3847/1538-4357/ad82e9. arXiv: 2410.01134 [astro-ph.HE].

Arnaud, K. A. (Jan. 1996). "XSPEC: The First Ten Years". In: *Astronomical Data Analysis Software and Systems V*. Ed. by George H. Jacoby and Jeannette Barnes. Vol. 101. Astronomical Society of the Pacific Conference Series, p. 17.

Balsamo, Erin et al. (Sept. 2012). "Development of full shell foil x-ray mirrors". In: *Modern Technologies in Space- and Ground-based Telescopes and Instrumentation II*. Ed. by Ramón Navarro, Colin R. Cunningham, and Eric Prieto. Vol. 8450. Society of Photo-Optical Instrumentation Engineers (SPIE) Conference Series, 845052, p. 845052. DOI: 10.1117/12.926152.

Bambi, Cosimo et al. (Aug. 2021). "Towards Precision Measurements of Accreting Black Holes Using X-Ray Reflection Spectroscopy". In: Space Sci. Rev. 217.5, 65, p. 65. DOI: 10.1007/s11214-021-00841-8. arXiv: 2011.04792 [astro-ph.HE].

Basak, Rupal and Andrzej A. Zdziarski (May 2016). "Spectral analysis of the XMM-Newton data of GX 339-4 in the low/hard state: disc truncation and reflection". In: MNRAS 458.2, pp. 2199–2214. DOI: 10.1093/mnras/stw420. arXiv: 1512.01833 [astro-ph.HE].

Beckmann, Volker and Chris R. Shrader (2012). *Active Galactic Nuclei*. John Wiley & Sons. DOI: 10.1002/9783527666829.

Belloni, T. (Oct. 2005). "Black Hole States: Accretion and Jet Ejection". In: *Interacting Binaries: Accretion, Evolution, and Outcomes*. Ed. by Luciano Burderi et al. Vol. 797. American Institute of Physics Conference Series. AIP, pp. 197–204. DOI: 10.1063/1.2130233. arXiv: astro-ph/0504185 [astro-ph].

Beloborodov, Andrei M. (Jan. 1999). "Plasma Ejection from Magnetic Flares and the X-Ray Spectrum of Cygnus X-1". In: ApJ 510.2, pp. L123–L126. DOI: 10.1086/311810. arXiv: astro-ph/9809383 [astro-ph].

Bolton, C. T. (Feb. 1972). "Identification of Cygnus X-1 with HDE 226868". In: Nature 235.5336, pp. 271–273. DOI: 10.1038/235271b0.

Burrows, David N. et al. (Oct. 2005). "The Swift X-Ray Telescope". In: Space Sci. Rev. 120.3-4, pp. 165–195. DOI: 10.1007/s11214-005-5097-2. arXiv: astro-ph/0508071 [astro-ph].

Buxton, Michelle M. et al. (June 2012). "Optical and Near-infrared Monitoring of the Black Hole X-Ray Binary GX 339-4 during 2002-2010". In: AJ 143.6, 130, p. 130. DOI: 10.1088/0004-6256/143/6/130. arXiv: 1203.5700 [astro-ph.GA].

Chakraborty, Sudip et al. (Nov. 2021). "NuSTAR monitoring of MAXI J1348-630: evidence of high density disc reflection". In: MNRAS 508.1, pp. 475–488. DOI: 10.1093/mnras/stab2530. arXiv: 2109.05380 [astro-ph.HE].

Corral-Santana, J. M. et al. (Mar. 2016). "BlackCAT: A catalogue of stellar-mass black holes in X-ray transients". In: A&A 587, A61, A61. DOI: 10.1051/0004-6361/201527130. arXiv: 1510.08869 [astro-ph.HE].

Dauser, T., J. Garcia, et al. (Oct. 2014). "The role of the reflection fraction in constraining black hole spin." In: MNRAS 444, pp. L100–L104. DOI: 10.1093/mnrasl/slu125. arXiv: 1408.2347 [astro-ph.HE].

Dauser, T., J. García, et al. (May 2016). "Normalizing a relativistic model of X-ray reflection. Definition of the reflection fraction and its implementation in relxill". In: A&A 590, A76, A76. DOI: 10.1051/0004-6361/201628135. arXiv: 1601.03771 [astro-ph.HE].

Dauser, T., J. Wilms, et al. (Dec. 2010). "Broad emission lines for a negatively spinning black hole". In: MNRAS 409.4, pp. 1534–1540. DOI: 10.1111/j.1365-2966.2010.17393.x. arXiv: 1007.4937 [astro-ph.HE].

Davis, Shane W. et al. (Mar. 2005). "Relativistic Accretion Disk Models of High-State Black Hole X-Ray Binary Spectra". In: ApJ 621.1, pp. 372–387. DOI: 10.1086/427278. arXiv: astro-ph/0408590 [astro-ph].

Dickey, John M. and Felix J. Lockman (Jan. 1990). "H I in the galaxy." In: ARA&A 28, pp. 215–261. DOI: 10.1146/annurev.aa.28.090190.001243.

Done, Chris and Maria Diaz Trigo (Oct. 2010). "A re-analysis of the iron line in the XMM-Newton data from the low/hard state in GX339-4". In: MNRAS 407.4, pp. 2287–2296. DOI: 10.1111/j.1365-2966.2010.17092.x. arXiv: 0911.3243 [astro-ph.HE].

Dovčiak, M., V. Karas, and T. Yaqoob (July 2004). "An Extended Scheme for Fitting X-Ray Data with Accretion Disk Spectra in the Strong Gravity Regime". In: ApJS 153.1, pp. 205–221. DOI: 10.1086/421115. arXiv: astro-ph/0403541 [astro-ph].

Duchêne, Gaspard and Adam Kraus (Aug. 2013). "Stellar Multiplicity". In: ARA&A 51.1, pp. 269–310. DOI: 10.1146/annurev-astro-081710-102602. arXiv: 1303.3028 [astro-ph.SR].

Einstein, A. (Jan. 1916). "Die Grundlage der allgemeinen Relativitätstheorie". In: *Annalen der Physik* 354.7, pp. 769–822. DOI: 10.1002/andp.19163540702.

Elvis, M. et al. (Apr. 1978). "Seyfert galaxies as X-ray sources." In: MNRAS 183, pp. 129–157. DOI: 10.1093/mnras/183.2.129.

Esin, Ann A., Jeffrey E. McClintock, and Ramesh Narayan (Nov. 1997). "Advection-Dominated Accretion and the Spectral States of Black Hole X-Ray Binaries: Application to Nova Muscae 1991". In: ApJ 489.2, pp. 865–889. DOI: 10.1086/304829. arXiv: astro-ph/9705237 [astro-ph].

Event Horizon Telescope Collaboration, Kazunori Akiyama, Antxon Alberdi, Walter Alef, Juan Carlos Algaba, et al. (May 2022). "First Sagittarius A* Event Horizon Telescope Results. I. The Shadow of the Supermassive Black Hole in the Center of the Milky Way". In: ApJ 930.2, L12, p. L12. DOI: 10.3847/2041-8213/ac6674.

Event Horizon Telescope Collaboration, Kazunori Akiyama, Antxon Alberdi, Walter Alef, Keiichi Asada, et al. (Apr. 2019). "First M87 Event Horizon Telescope Results. I. The Shadow of the Supermassive Black Hole". In: ApJ 875.1, L1, p. L1. DOI: 10.3847/2041-8213/ab0ec7. arXiv: 1906.11238 [astro-ph.GA].

Fabian, A. C., K. Iwasawa, et al. (Sept. 2000). "Broad Iron Lines in Active Galactic Nuclei". In: PASP 112.775, pp. 1145–1161. DOI: 10.1086/316610. arXiv: astro-ph/0004366 [astro-ph].

Fabian, A. C., M. J. Rees, et al. (May 1989). "X-ray fluorescence from the inner disc in Cygnus X-1." In: MNRAS 238, pp. 729–736. DOI: 10.1093/mnras/238.3.729.

Fan, Ningyue et al. (July 2024). "The 2018 Outburst of MAXI J1820+070 as Seen by Insight-HXMT". In: ApJ 969.1, 61, p. 61. DOI: 10.3847/1538-4357/ad49a1. arXiv: 2404.12161 [astro-ph.HE].

Fender, R. P., T. M. Belloni, and E. Gallo (Dec. 2004). "Towards a unified model for black hole X-ray binary jets". In: MNRAS 355.4, pp. 1105–1118. DOI: 10.1111/j.1365-2966.2004.08384.x. arXiv: astro-ph/0409360 [astro-ph].

Fender, Rob and Tomaso Belloni (Aug. 2012). "Stellar-Mass Black Holes and Ultraluminous X-ray Sources". In: *Science* 337.6094, p. 540. DOI: 10.1126/science.1221790. arXiv: 1208.1138 [astro-ph.HE].

Fürst, F. et al. (Aug. 2015). "The Complex Accretion Geometry of GX 339-4 as Seen by NuSTAR and Swift". In: ApJ 808.2, 122, p. 122. DOI: 10.1088/0004-637X/808/2/122. arXiv: 1506.01381 [astro-ph.HE].

García, J., T. Dauser, et al. (Feb. 2014). "Improved Reflection Models of Black Hole Accretion Disks: Treating the Angular Distribution of X-Rays". In: ApJ 782.2, 76, p. 76. DOI: 10.1088/0004-637X/782/2/76. arXiv: 1312.3231 [astro-ph.HE].

García, J. and T. R. Kallman (Aug. 2010). "X-ray Reflected Spectra from Accretion Disk Models. I. Constant Density Atmospheres". In: ApJ 718.2, pp. 695–706. DOI: 10.1088/0004-637X/718/2/695. arXiv: 1006.0485 [astro-ph.HE].

García, J. A. et al. (Aug. 2018). "The Problem of the High Iron Abundance in Accretion Disks around Black Holes". In: *Workshop on Astrophysical Opacities*. Vol. 515. Astronomical Society of the Pacific Conference Series, p. 282. DOI: 10.48550/arXiv.1805.00581. arXiv: 1805.00581 [astro-ph.HE].

García, Javier A. et al. (Nov. 2015). "X-Ray Reflection Spectroscopy of the Black Hole GX 339–4: Exploring the Hard State with Unprecedented Sensitivity". In: ApJ 813.2, 84, p. 84. DOI: 10.1088/0004-637X/813/2/84. arXiv: 1505.03607 [astro-ph.HE].

Gehrels, N. et al. (Aug. 2004). "The Swift Gamma-Ray Burst Mission". In: ApJ 611.2, pp. 1005–1020. DOI: 10.1086/422091. arXiv: astro-ph/0405233 [astro-ph].

Gendreau, Keith C. et al. (July 2016). "The Neutron star Interior Composition Explorer (NICER): design and development". In: *Space Telescopes and Instrumentation 2016: Ultraviolet to Gamma Ray*. Ed. by Jan-Willem A. den Herder, Tadayuki Takahashi, and Marshall Bautz. Vol. 9905. Society of Photo-Optical

Instrumentation Engineers (SPIE) Conference Series, 99051H, 99051H. DOI: 10.1117/12.2231304.

Genzel, Reinhard, Frank Eisenhauer, and Stefan Gillessen (Oct. 2010). "The Galactic Center massive black hole and nuclear star cluster". In: *Reviews of Modern Physics* 82.4, pp. 3121–3195. DOI: 10.1103/RevModPhys.82.3121. arXiv: 1006.0064 [astro-ph.GA].

George, I. M. and A. C. Fabian (Mar. 1991). "X-ray reflection from cold matter in Active Galactic Nuclei and X-ray binaries." In: MNRAS 249, p. 352. DOI: 10.1093/mnras/249.2.352.

Ghez, A. M. et al. (Dec. 2008). "Measuring Distance and Properties of the Milky Way's Central Supermassive Black Hole with Stellar Orbits". In: ApJ 689.2, pp. 1044–1062. DOI: 10.1086/592738. arXiv: 0808.2870 [astro-ph].

Gillessen, S. et al. (Mar. 2017). "An Update on Monitoring Stellar Orbits in the Galactic Center". In: ApJ 837.1, 30, p. 30. DOI: 10.3847/1538-4357/aa5c41. arXiv: 1611.09144 [astro-ph.GA].

Gonzalez, A. G., D. R. Wilkins, and L. C. Gallo (Dec. 2017). "Probing the geometry and motion of AGN coronae through accretion disc emissivity profiles". In: MNRAS 472.2, pp. 1932–1945. DOI: 10.1093/mnras/stx2080. arXiv: 1708.03205 [astro-ph.HE].

Haardt, F. and L. Maraschi (Oct. 1991). "A Two-Phase Model for the X-Ray Emission from Seyfert Galaxies". In: ApJ 380, p. L51. DOI: 10.1086/186171.

Haardt, Francesco and Laura Maraschi (Aug. 1993). "X-Ray Spectra from Two-Phase Accretion Disks". In: ApJ 413, p. 507. DOI: 10.1086/173020.

Häberle, Maximilian et al. (July 2024). "Fast-moving stars around an intermediate-mass black hole in ω Centauri". In: Nature 631.8020, pp. 285–288. DOI: 10.1038/s41586-024-07511-z. arXiv: 2405.06015 [astro-ph.GA].

Hailey, Charles J. et al. (July 2010). "The Nuclear Spectroscopic Telescope Array (NuSTAR): optics overview and current status". In: *Space Telescopes and Instrumentation 2010: Ultraviolet to Gamma Ray*. Ed. by Monique Arnaud, Stephen S. Murray, and Tadayuki Takahashi. Vol. 7732. Society of Photo-Optical Instrumentation Engineers (SPIE) Conference Series, 77320T. DOI: 10.1117/12.857654.

Harrison, Fiona A., Walter R. Cook, et al. (2010). "Cadmium Zinc Telluride Pixel Detectors for Hard X-Ray Astrophysics". In: *Semiconductor Radiation Detection Systems*. Ed. by Krzysztof Iniewski. Boca Raton, FL: CRC Press, pp. 67–82. DOI: 10.1201/9781315218373.

Harrison, Fiona A., William W. Craig, et al. (June 2013). "The Nuclear Spectroscopic Telescope Array (NuSTAR) High-energy X-Ray Mission". In: ApJ 770.2, 103, p. 103. DOI: 10.1088/0004-637X/770/2/103. arXiv: 1301.7307 [astro-ph.IM].

Haymes, R. C. and F. R. Harnden Jr. (Mar. 1970). "Low-Energy Gamma Radiation from Cygnus". In: ApJ 159, p. 1111. DOI: 10.1086/150391.

Heida, M. et al. (Sept. 2017). "The Mass Function of GX 339-4 from Spectroscopic Observations of Its Donor Star". In: ApJ 846.2, 132, p. 132. DOI: 10.3847/1538-4357/aa85df. arXiv: 1708.04667 [astro-ph.HE].

HI4PI Collaboration et al. (Oct. 2016). "HI4PI: A full-sky H I survey based on EBHIS and GASS". In: A&A 594, A116, A116. DOI: 10.1051/0004-6361/201629178. arXiv: 1610.06175 [astro-ph.GA].

Jansen, F. et al. (Jan. 2001). "XMM-Newton observatory. I. The spacecraft and operations". In: A&A 365, pp. L1–L6. DOI: 10.1051/0004-6361:20000036.

Kaastra, J. S. and J. A. M. Bleeker (Mar. 2016). "Optimal binning of X-ray spectra and response matrix design". In: A&A 587, A151, A151. DOI: 10.1051/0004-6361/201527395. arXiv: 1601.05309 [astro-ph.IM].

Kalberla, P. M. W. et al. (Sept. 2005). "The Leiden/Argentine/Bonn (LAB) Survey of Galactic HI. Final data release of the combined LDS and IAR surveys with improved stray-radiation corrections". In: A&A 440.2, pp. 775–782. DOI: 10.1051/0004-6361:20041864. arXiv: astro-ph/0504140 [astro-ph].

Kerr, Roy P. (Sept. 1963). "Gravitational Field of a Spinning Mass as an Example of Algebraically Special Metrics". In: Phys. Rev. Lett. 11.5, pp. 237–238. DOI: 10.1103/PhysRevLett.11.237.

Kolehmainen, Mari, Chris Done, and María Díaz Trigo (Jan. 2014). "The soft component and the iron line as signatures of the disc inner radius in Galactic black hole binaries". In: MNRAS 437.1, pp. 316–326. DOI: 10.1093/mnras/stt1886. arXiv: 1310.1219 [astro-ph.HE].

Krawczynski, Henric et al. (Nov. 2022). "Polarized x-rays constrain the disk-jet geometry in the black hole x-ray binary Cygnus X-1". In: *Science* 378.6620, pp. 650–654. DOI: 10.1126/science.add5399. arXiv: 2206.09972 [astro-ph.HE].

Laor, Ari (July 1991). "Line Profiles from a Disk around a Rotating Black Hole". In: ApJ 376, p. 90. DOI: 10.1086/170257.

Lightman, A. P. and S. L. Shapiro (June 1975). "Spectrum and polarization of X-rays from accretion disks around black holes." In: ApJ 198, pp. L73–L75. DOI: 10.1086/181815.

Liu, Honghui, Cosimo Bambi, et al. (June 2023). "The Hard-to-soft Transition of GX 339-4 as Seen by Insight-HXMT". In: ApJ 950.1, 5, p. 5. DOI: 10.3847/1538-4357/acca17. arXiv: 2211.09543 [astro-ph.HE].

Liu, Honghui, Jiachen Jiang, Zuobin Zhang, Cosimo Bambi, Andrew C. Fabian, et al. (July 2023). "High-density Reflection Spectroscopy of Black Hole X-Ray Binaries in the Hard State". In: ApJ 951.2, 145, p. 145. DOI: 10.3847/1538-4357/acd8b9. arXiv: 2303.10593 [astro-ph.HE].

Liu, Honghui, Jiachen Jiang, Zuobin Zhang, Cosimo Bambi, Long Ji, et al. (July 2022). "Rapidly alternating flux states of GX 339-4 during its 2021 outburst captured by Insight-HXMT". In: MNRAS 513.3, pp. 4308–4317. DOI: 10.1093/mnras/stac1178. arXiv: 2202.04780 [astro-ph.HE].

Liu, Jie-Ying, Jirong Mao, and B. F. Liu (Jan. 2024). "Magnetic-reconnection-heated corona model: implication of hybrid electrons for hard X-ray emission of luminous active galactic nuclei". In: MNRAS 527.3, pp. 5627–5637. DOI: 10.1093/mnras/stad3615. arXiv: 2311.13135 [astro-ph.HE].

Ludlam, R. M., J. M. Miller, and E. M. Cackett (June 2015). "Reapproaching the Spin Estimate of GX 339-4". In: ApJ 806.2, 262, p. 262. DOI: 10.1088/0004-637X/806/2/262. arXiv: 1505.05449 [astro-ph.HE].

Madsen, Kristin K. et al. (May 2020). "NuSTAR low energy effective area correction due to thermal blanket tear". In: *arXiv e-prints*, arXiv:2005.00569, arXiv:2005.00569. DOI: 10.48550/arXiv.2005.00569. arXiv: 2005.00569 [astro-ph.IM].

Markert, T. H. et al. (Sept. 1973). "Observations of the Highly Variable X-Ray Source GX 339-4". In: ApJ 184, p. L67. DOI: 10.1086/181290.

Markoff, Sera, Michael A. Nowak, and Jörn Wilms (Dec. 2005). "Going with the Flow: Can the Base of Jets Subsume the Role of Compact Accretion Disk Coronae?" In: ApJ 635.2, pp. 1203–1216. DOI: 10.1086/497628. arXiv: astro-ph/0509028 [astro-ph].

Martocchia, Andrea and Giorgio Matt (Oct. 1996). "Iron Kalpha line intensity from accretion discs around rotating black holes". In: MNRAS 282.4, pp. L53–L57. DOI: 10.1093/mnras/282.4.L53.

Matsuoka, Masaru et al. (Oct. 2009). "The MAXI Mission on the ISS: Science and Instruments for Monitoring All-Sky X-Ray Images". In: PASJ 61, p. 999. DOI: 10.1093/pasj/61.5.999. arXiv: 0906.0631 [astro-ph.IM].

Miller, J. M., A. C. Fabian, et al. (May 2004). "Evidence of Black Hole Spin in GX 339-4: XMM-Newton/EPIC-pn and RXTE Spectroscopy of the Very High State". In: ApJ 606.2, pp. L131–L134. DOI: 10.1086/421263. arXiv: astro-ph/0312033 [astro-ph].

Miller, J. M., J. Homan, et al. (Dec. 2006). "A Long, Hard Look at the Low/Hard State in Accreting Black Holes". In: ApJ 653.1, pp. 525–535. DOI: 10.1086/508644. arXiv: astro-ph/0602633 [astro-ph].

Mitsuda, K. et al. (Jan. 1984). "Energy spectra of low-mass binary X-ray sources observed from Tenma." In: PASJ 36, pp. 741–759.

Narayan, Ramesh and Insu Yi (June 1994). "Advection-dominated Accretion: A Self-similar Solution". In: ApJ 428, p. L13. DOI: 10.1086/187381. arXiv: astro-ph/9403052 [astro-ph].

Nath, Sujoy Kumar et al. (Jan. 2024). "Accretion Flow Properties of EXO 1846-031 during Its Multi-peaked Outburst after Long Quiescence". In: ApJ 960.1, 5, p. 5. DOI: 10.3847/1538-4357/ad0735. arXiv: 2307.04522 [astro-ph.HE].

Okajima, Takashi et al. (July 2016). "Performance of NICER flight x-ray concentrator". In: *Space Telescopes and Instrumentation 2016: Ultraviolet to Gamma Ray*. Ed. by Jan-Willem A. den Herder, Tadayuki Takahashi, and Marshall Bautz. Vol. 9905. Society of Photo-Optical Instrumentation Engineers (SPIE) Conference Series, 99054X, p. 99054X. DOI: 10.1117/12.2234436.

Parker, M. L., J. A. Tomsick, J. A. Kennea, et al. (Mar. 2016). "NuSTAR and Swift observations of the very high state in GX 339-4: Weighing the black hole with X-rays". In: *arXiv e-prints*, arXiv:1603.03777, arXiv:1603.03777. DOI: 10.48550/arXiv.1603.03777. arXiv: 1603.03777 [astro-ph.HE].

Parker, M. L., J. A. Tomsick, J. M. Miller, et al. (July 2015). "NuSTAR and Suzaku Observations of the Hard State in Cygnus X-1: Locating the Inner Accretion Disk". In: ApJ 808.1, 9, p. 9. DOI: 10.1088/0004-637X/808/1/9. arXiv: 1506.00007 [astro-ph.HE].

Penrose, Roger (Jan. 1969). "Gravitational Collapse: the Role of General Relativity". In: *Nuovo Cimento Rivista Serie* 1, p. 252. DOI: 10.1023/A:1016578408204.

Plant, D. S. et al. (Jan. 2015). "The truncated and evolving inner accretion disc of the black hole GX 339-4". In: A&A 573, A120, A120. DOI: 10.1051/0004-6361/201423925. arXiv: 1309.4781 [astro-ph.HE].

Poutanen, Juri and Roland Svensson (Oct. 1996). "The Two-Phase Pair Corona Model for Active Galactic Nuclei and X-Ray Binaries: How to Obtain Exact Solutions". In: ApJ 470, p. 249. DOI: 10.1086/177865. arXiv: astro-ph/9605073 [astro-ph].

Poutanen, Juri, Alexandra Veledina, and Andrei M. Beloborodov (May 2023). "Polarized X-Rays from Windy Accretion in Cygnus X-1". In: ApJ 949.1, L10, p. L10. DOI: 10.3847/2041-8213/acd33e. arXiv: 2302.11674 [astro-ph.HE].

Prigozhin, Gregory et al. (July 2016). "NICER instrument detector subsystem: description and performance". In: *Space Telescopes and Instrumentation 2016: Ultraviolet to Gamma Ray*. Ed. by Jan-Willem A. den Herder, Tadayuki Takahashi, and Marshall Bautz. Vol. 9905. Society of Photo-Optical Instrumentation Engineers (SPIE) Conference Series, 99051I, p. 99051I. DOI: 10.1117/12.2231718.

Pringle, J. E. (July 1996). "Self-induced warping of accretion discs". In: MNRAS 281.1, pp. 357–361. DOI: 10.1093/mnras/281.1.357.

Reis, R. C. et al. (July 2008). "A systematic look at the very high and low/hard state of GX339-4: constraining the black hole spin with a new reflection model". In: MNRAS 387.4, pp. 1489–1498. DOI: 10.1111/j.1365-2966.2008.13358.x. arXiv: 0804.0238 [astro-ph].

Ross, R. R. and A. C. Fabian (Mar. 2005). "A comprehensive range of X-ray ionized-reflection models". In: MNRAS 358.1, pp. 211–216. DOI: 10.1111/j.1365-2966.2005.08797.x. arXiv: astro-ph/0501116 [astro-ph].

Saade, M. Lynne et al. (Oct. 2024). "A Comparison of the X-Ray Polarimetric Properties of Stellar and Supermassive Black Holes". In: ApJ 974.1, 101, p. 101. DOI: 10.3847/1538-4357/ad73a3. arXiv: 2408.12746 [astro-ph.HE].

Schreier, E. et al. (Nov. 1971). "Further Observations of the Pulsating X-Ray Source Cygnus X-1 from UHURU". In: ApJ 170, p. L21. DOI: 10.1086/180833.

Schwarzschild, Karl (Jan. 1916). "Über das Gravitationsfeld eines Massenpunktes nach der Einsteinschen Theorie". In: *Sitzungsberichte der Königlich Preussischen Akademie der Wissenschaften*, pp. 189–196.

Shakura, N. I. and R. A. Sunyaev (Jan. 1973). "Black holes in binary systems. Observational appearance." In: A&A 24, pp. 337–355.

Shapiro, S. L., A. P. Lightman, and D. M. Eardley (Feb. 1976). "A two-temperature accretion disk model for Cygnus X-1: structure and spectrum." In: ApJ 204, pp. 187–199. DOI: 10.1086/154162.

Shidatsu, Megumi et al. (Nov. 2011). "X-Ray and Near-Infrared Observations of GX 339-4 in the Low/Hard State with Suzaku and IRSF". In: PASJ 63, S785–S801. DOI: 10.1093/pasj/63.sp3.S785. arXiv: 1105.3586 [astro-ph.HE].

Shyam Prakash V., P., C. Ramadevi M., and Vivek K. Agrawal (May 2024). "Astrosat view of GX 339-4 during the peak of the recent outburst". In: *arXiv e-prints*, arXiv:2405.06090, arXiv:2405.06090. DOI: 10.48550/arXiv.2405.06090. arXiv: 2405.06090 [astro-ph.HE].

Sreehari, H. et al. (Feb. 2019). "Constraining the mass of the black hole GX 339-4 using spectro-temporal analysis of multiple outbursts". In: *Advances in Space*

Research 63.3, pp. 1374–1386. DOI: 10.1016/j.asr.2018.10.042. arXiv: 1811.04341 [astro-ph.HE].

Steiner, James F., Javier A. García, et al. (Feb. 2017). "Self-consistent Black Hole Accretion Spectral Models and the Forgotten Role of Coronal Comptonization of Reflection Emission". In: ApJ 836.1, 119, p. 119. DOI: 10.3847/1538-4357/836/1/119. arXiv: 1701.03777 [astro-ph.HE].

Steiner, James F., Jeffrey E. McClintock, et al. (Aug. 2010). "The Constant Inner-disk Radius of LMC X-3: A Basis for Measuring Black Hole Spin". In: ApJ 718.2, pp. L117–L121. DOI: 10.1088/2041-8205/718/2/L117. arXiv: 1006.5729 [astro-ph.HE].

Steiner, James F., Edward Nathan, et al. (July 2024). "An IXPE-led X-Ray Spectropolarimetric Campaign on the Soft State of Cygnus X-1: X-Ray Polarimetric Evidence for Strong Gravitational Lensing". In: ApJ 969.2, L30, p. L30. DOI: 10.3847/2041-8213/ad58e4. arXiv: 2406.12014 [astro-ph.HE].

Svoboda, Jiří et al. (May 2024). "Dramatic Drop in the X-Ray Polarization of Swift J1727.8–1613 in the Soft Spectral State". In: ApJ 966.2, L35, p. L35. DOI: 10.3847/2041-8213/ad402e. arXiv: 2403.04689 [astro-ph.HE].

Tao, Lian et al. (Dec. 2019). "The Spin of the Black Hole GRS 1716-249 Determined from the Hard Intermediate State". In: ApJ 887.2, 184, p. 184. DOI: 10.3847/1538-4357/ab5282. arXiv: 1910.11979 [astro-ph.HE].

Thorne, Kip S. (July 1974). "Disk-Accretion onto a Black Hole. II. Evolution of the Hole". In: ApJ 191, pp. 507–520. DOI: 10.1086/152991.

Tomsick, John A., Emrah Kalemci, et al. (June 2008). "Broadband X-Ray Spectra of GX 339-4 and the Geometry of Accreting Black Holes in the Hard State". In: ApJ 680.1, pp. 593–601. DOI: 10.1086/587797. arXiv: 0802.3357 [astro-ph].

Tomsick, John A., Kazutaka Yamaoka, et al. (Dec. 2009). "Truncation of the Inner Accretion Disk Around a Black Hole at Low Luminosity". In: ApJ 707.1, pp. L87–L91. DOI: 10.1088/0004-637X/707/1/L87. arXiv: 0911.2240 [astro-ph.HE].

Ubach, Santiago et al. (Nov. 2024). "Self-consistent Disk-reflection Analysis of the Black Hole Candidate X-Ray Binary MAXI J1813-095 with NICER, Swift, Chandra, and NuSTAR". In: ApJ 976.1, 38, p. 38. DOI: 10.3847/1538-4357/ad7b2c. arXiv: 2409.13481 [astro-ph.HE].

Verner, D. A. et al. (July 1996). "Atomic Data for Astrophysics. II. New Analytic Fits for Photoionization Cross Sections of Atoms and Ions". In: ApJ 465, p. 487. DOI: 10.1086/177435. arXiv: astro-ph/9601009 [astro-ph].

Vitral, Eduardo et al. (July 2023). "An elusive dark central mass in the globular cluster M4". In: MNRAS 522.4, pp. 5740–5757. DOI: 10.1093/mnras/stad1068. arXiv: 2305.12702 [astro-ph.GA].

Walton, D. J. et al. (Apr. 2017). "Living on a Flare: Relativistic Reflection in V404 Cyg Observed by NuSTAR during Its Summer 2015 Outburst". In: ApJ 839.2, 110, p. 110. DOI: 10.3847/1538-4357/aa67e8. arXiv: 1609.01293 [astro-ph.HE].

Wang, Jingyi, Erin Kara, Matteo Lucchini, et al. (May 2022). "The NICER "Reverberation Machine": A Systematic Study of Time Lags in Black Hole X-Ray Binaries". In: ApJ 930.1, 18, p. 18. DOI: 10.3847/1538-4357/ac6262. arXiv: 2205.00928 [astro-ph.HE].

Wang, Jingyi, Erin Kara, James F. Steiner, et al. (Aug. 2020). "Relativistic Reflection and Reverberation in GX 339-4 with NICER and NuSTAR". In: ApJ 899.1, 44, p. 44. DOI: 10.3847/1538-4357/ab9ec3. arXiv: 1910.01245 [astro-ph.HE].

Wang-Ji, Jingyi et al. (Mar. 2018). "The Evolution of GX 339-4 in the Low-hard State as Seen by NuSTAR and Swift". In: ApJ 855.1, 61, p. 61. DOI: 10.3847/1538-4357/aaa974. arXiv: 1712.02571 [astro-ph.HE].

Webster, B. Louise and Paul Murdin (Jan. 1972). "Cygnus X-1-a Spectroscopic Binary with a Heavy Companion ?" In: Nature 235.5332, pp. 37–38. DOI: 10.1038/235037a0.

Weisskopf, Martin C. et al. (Apr. 2022). "The Imaging X-Ray Polarimetry Explorer (IXPE): Pre-Launch". In: *Journal of Astronomical Telescopes, Instruments, and Systems* 8.2, 026002, p. 026002. DOI: 10.1117/1.JATIS.8.2.026002. arXiv: 2112.01269 [astro-ph.IM].

Wilkins, D. R. and A. C. Fabian (Aug. 2012). "Understanding X-ray reflection emissivity profiles in AGN: locating the X-ray source". In: MNRAS 424.2, pp. 1284–1296. DOI: 10.1111/j.1365-2966.2012.21308.x. arXiv: 1205.3179 [astro-ph.HE].

Wilms, J., A. Allen, and R. McCray (Oct. 2000). "On the Absorption of X-Rays in the Interstellar Medium". In: ApJ 542.2, pp. 914–924. DOI: 10.1086/317016. arXiv: astro-ph/0008425 [astro-ph].

Woitke, Peter (Sept. 2015). "Modelling and interpretation of SEDs". In: *European Physical Journal Web of Conferences*. Vol. 102. European Physical Journal Web of Conferences, 00007, p. 00007. DOI: 10.1051/epjconf/201510200007.

Zdziarski, A. A., W. N. Johnson, and P. Magdziarz (Nov. 1996). "Broad-band γ-ray and X-ray spectra of NGC 4151 and their implications for physical processes and geometry." In: MNRAS 283.1, pp. 193–206. DOI: 10.1093/mnras/283.1.193. arXiv: astro-ph/9607015 [astro-ph].

Zdziarski, Andrzej A., Marek Gierliński, et al. (July 2004). "GX 339-4: the distance, state transitions, hysteresis and spectral correlations". In: MNRAS 351.3, pp. 791–807. DOI: 10.1111/j.1365-2966.2004.07830.x. arXiv: astro-ph/0402380 [astro-ph].

Zdziarski, Andrzej A., Janusz Ziółkowski, and Joanna Mikołajewska (Sept. 2019). "The X-ray binary GX 339-4/V821 Ara: the distance, inclination, evolutionary status, and mass transfer". In: MNRAS 488.1, pp. 1026–1034. DOI: 10.1093/mnras/stz1787. arXiv: 1904.07803 [astro-ph.SR].

Zhang, Shuang-Nan et al. (Apr. 2020). "Overview to the Hard X-ray Modulation Telescope (Insight-HXMT) Satellite". In: *Science China Physics, Mechanics, and Astronomy* 63.4, 249502, p. 249502. DOI: 10.1007/s11433-019-1432-6. arXiv: 1910.09613 [astro-ph.IM].

Życki, Piotr T., Chris Done, and David A. Smith (Nov. 1999). "The 1989 May outburst of the soft X-ray transient GS 2023+338 (V404 Cyg)". In: MNRAS 309.3, pp. 561–575. DOI: 10.1046/j.1365-8711.1999.02885.x. arXiv: astro-ph/9904304 [astro-ph].